6-18-2015

Identifying the experimental and theoretical effective characteristics of nonaligned anisotropic metamaterials

Michael R. Benson

Recommended Citation

Benson, Michael R., "Identifying the experimental and theoretical effective characteristics of nonaligned anisotropic metamaterials" (2015). *Theses and Dissertations*. 193.
https://scholar.afit.edu/etd/193

Identifying the experimental and theoretical effective characteristics of nonaligned anisotropic metamaterials

DISSERTATION

Michael R. Benson

AFIT-ENP-DS-15-J-008

DEPARTMENT OF THE AIR FORCE
AIR UNIVERSITY

AIR FORCE INSTITUTE OF TECHNOLOGY

Wright-Patterson Air Force Base, Ohio

DISTRIBUTION STATEMENT A
APPROVED FOR PUBLIC RELEASE; DISTRIBUTION UNLIMITED.

AFIT-ENP-DS-15-J-008

IDENTIFYING THE EXPERIMENTAL AND THEORETICAL EFFECTIVE CHARACTERISTICS OF NONALIGNED ANISOTROPIC METAMATERIALS

DISSERTATION

Presented to the Faculty
Graduate School of Engineering and Management
Air Force Institute of Technology
Air University
Air Education and Training Command
in Partial Fulfillment of the Requirements for the
Degree of Master of Science in Applied Physics

Michael R. Benson, B.S.E.E., M.S.

15 June 2015

AFIT-ENP-DS-15-J-008

IDENTIFYING THE EXPERIMENTAL AND THEORETICAL EFFECTIVE CHARACTERISTICS OF NONALIGNED ANISOTROPIC METAMATERIALS

DISSERTATION

Michael R. Benson, B.S.E.E., M.S.

Committee Membership:

Dr. M. A. Marciniak
Chairman

LtCol A. L. Franz, PhD
Member

Dr. M. E. Oxley
Member

Dr. S. E. Nauyoks
Member

Dr. A. M. Urbas
Member

AFIT-ENP-DS-15-J-008

Abstract

Previous research into anisotropic materials has assumed certain properties in order to make the underlying mathematics tractable. One of the assumptions is the alignment of the optical axes with the laboratory frame of reference, such as split-ring resonators lying flat on the material plane. This assumption does not hold true for many metamaterials, such as tilted nanorods. Techniques such as ellipsometry are needed to analyze the effective characteristics of these highly anisotropic structures. In this research, tilted nanorods are analyzed using generalized ellipsometry to extract the indices of the optical axes. The underlying physics of ellipsometry is then used to create a new effective characterization technique called Permittivity and Permeability Tensor Extraction (PPTE), which makes fewer assumptions about the underlying structure of the material and allows for the analysis of a much larger class of structures. PPTE is used to find the effective characteristics of several structures, such as a structure with anisotropy-inducing inclusions and the tilted nanorods. Finally, PPTE is used to begin to examine some of the underlying presumptions about how metamaterials operate, demonstrating that some of the classically used models for calculating permittivity tensors are approximations. The utility of these models in determining the permittivity tensor is studied for several different materials with different properties.

Acknowledgements

To Dr. Marciniak, who gave me an opportunity I did not deserve.

To all of my professors, who taught me everything I know.

To my coworkers, who helped me work through all of this.

To my friends and my family and my friends who are my family, who been by my side this entire time.

To my Dad, who always knew I could do better.

To my Mom, who will always be smarter than me.

To my wife, who was always right there beside me.

To my God, who gave me all of these.

Thank you so much.

Michael R. Benson

Table of Contents

Page

List of Figures

Figure Page

List of Tables

List of Symbols

Symbol		Page
Ψ	Psi	16
Δ	Del	16
$\boldsymbol{E}$	Electric field	16
$\boldsymbol{B}$	Magnetic induction field	16
$\boldsymbol{D}$	Electric displacement field	16
$\boldsymbol{H}$	Magnetic field	16
t	Time	16
ω	Angular frequency	16
$\boldsymbol{r}$	Position	17
$\boldsymbol{k}$	Direction of propagation	17
ς	Field delay	17
μ	Permeability	17
ϵ	Permittivity	17
ρ	Complex reflection coefficient	19
ϕ	Rotation angle	21
r	Reflection ratio	22
θ	Angle of incidence	26
n	Index of refraction	26
k	Extinction coefficient	26
N	Complex index of refraction	26
d	Layer thickness	29
α	Polarizability	33

Symbol		Page
η	Number of electrons	33
P	Polarization	33
f	Volume fraction	34
A	Oscillator Amplitude	35
Γ	Oscillator width	35
ω_0	Oscillator center frequency	35
σ_{se}^2	Reflectance-based figure of merit	38
ξ_{se}^2	Angle-based figure of merit	39
χ_{SE}^2	Error-based figure of merit	39
T	Material transfer matrix	51
T_p	Layer transfer matrix	52
L_i	Front projection matrix	52
L_t	Rear projection matrix	53
Δ_B	Berreman's matrix	56
K_{xx}	Propagation constant	56
$\hat{\alpha}$	Crystalline axis	59
$\hat{\beta}$	Crystalline axis	59
$\hat{\gamma}$	Crystalline axis	59
R	Rotation matrix	59
L_j^D	TAB depolarization factor	64
$U_{\{\alpha,\beta,\gamma\}}$	Ellipsoidal size parameters	65
D_j^D	RAB depolarization factor	65
A	Absorptance	78
R	Total reflectance	78

List of Abbreviations

Abbreviation		Page
IR-VASE	Infrared Variable Angle Spectral Ellipsometer	5
PPTE	Permittivity and Permeability Tensor Extraction	6
CREATE	Computational Research and Engineering Acquisition Tools and Environments	6
FTIR	Fourier Transform Infrared	24
PSC$_{\text{R}}$A	Polarizer-Sample-Rotated compensator-Analyzer	24
EMA	Effective Medium Approximation	33
RAE	Rotating Analyzer Ellipsometer	48
CGS	Centimeter-Gram-Second	53
HBLA	Homogenous Biaxial Layer Approximation	62
TAB	Traditional Anisotropic Bruggeman	64
RAB	Rigorous Anisotropic Bruggeman	64
GLAD	Glancing Angle Deposition	72
HDR	Hemispherical Directional Reflectance	79
HDT	Hemispherical Directional Transmittance	79
DOLP	Degree of Linear Polarization	86
CEM	Computational Electromagnetics	88
PEC	Perfect Electric Conductors	100
IFT	Implicit Function Theorem	138

IDENTIFYING THE EXPERIMENTAL AND THEORETICAL EFFECTIVE CHARACTERISTICS OF NONALIGNED ANISOTROPIC METAMATERIALS

I. Introduction

The research that has culminated in this document began some time in 2013. Dr. Sarangan and (the now) Dr. Shah of the University of Dayton had created two unique tilted-nanorod samples. These materials are small silver rods a few hundred nanometers long, tens of nanometers wide, irregular in length and width and shape, and randomly arrayed across a silicon substrate. The first sample demonstrated short and thick nanorods, while the second demonstrated long and skinny nanorods. This is demosntrated in Figure 20. The University of Dayton research group asked Dr. Marciniak and his research team to help measure its characteristics. Dr. Marciniak gave the sample to me for measurements, and that started a very long process which eventually ended with this dissertation.

Tilted nanorods are interesting metamaterials due to their tilted nature [14, 16, 38, 71, 74, 75, 77, 78, 85]. The majority of metamaterial research has been performed on materials where the structures are aligned with laboratory frame of reference [35,52,64,87,88,95]; for example, a split-ring resonator is built with gaps aligned with the tiling directions [31, 34, 58]. Tilted nanorods do not have this kind of inherent structure. They are built such that the long axis of the rod is not perpendicular with the plane of the material, which gives them both triclinic characteristics and create optical axes not aligned with the laboratory frame of reference.

The tilted nature of these materials creates numerous difficulties in determining their properties using techniques other than ellipsometry. Traditional techniques

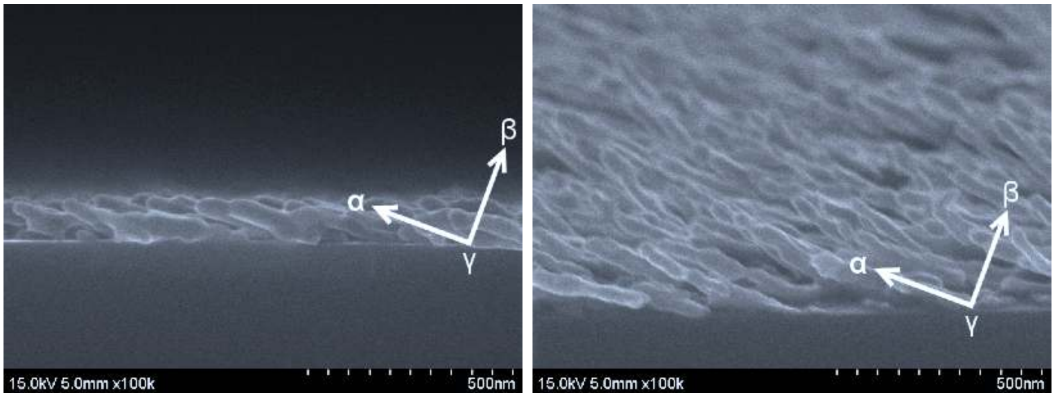

Figure 1. SEM images of silver nanorods. Left sample was grown at 300K, while the right sample was grown at 100k.

assume that the material parameters are simple and aligned with the laboratory frame of reference, which is an invalid assumption for tilted crystal-like materials [30, 75, 78]. The simplicity is necessary to make the underlying mathematics tractable [86]. Because of these characteristics, new techniques must be created to determine the properties of these materials.

This dissertation will determine the effective material parameters of the two nanorod samples shown in Figure 1, as well as determine similar parameters for a model of the materials. Generalized Ellipsometry will be detailed and used to determine the index and orientation of the optical axes of both materials. These measurements can be directly compared against each other to demonstrate the impact of the material's geometry on the effective material parameters. A new effective material parameter extraction technique will be derived to analyze the same parameters for a model of the nanorod. This technique can be used on a much broader class of materials, such as anisotropic non-aligned metamaterial structures and crystals with axes unaligned with the laboratory frame of reference.

1.1 Problem Statement

These nanorods are complex metamaterials that have characteristics that are not found in most materials [75, 77, 78]. The tilted aspect of the materials impart triclinic characteristics, a characteristic found in few materials outside of crystals. Materials that are triclinic in nature are classically studied using a technique known as ellipsometry [93]. This research seeks to understand why the materials exhibits these characteristics. This requires building and analyzing models of the structures. The purpose of this research is to both measure and model the behaviors of these materials in order to understand the relationship between the material's geometry and its optical characteristics.

Identifying this relationship will ultimately lead to the ability to design nanorod-based materials that can achieve some specific purpose. These materials could then be engineered to have specific optical properties by designing some physical geometry. This would allow for greater material utility, and could lead to the discovery and creation of application specific nanorod-based materials.

1.2 Scope and Goals

The tilt of the materials creates a coupling between portions of the fields within the materials that are traditionally independent. The field of ellipsometry traditionally analyzes these structures, but is an iterative process not well suited for use within simulations. A preferable tool would be a linear one, which could begin with some set of measurements and directly extract the solution from the input. A functional diagram of both processes is shown in Figure 2. Ellipsometry is necessary for laboratory work, but is non-ideal for usage within simulations.

This research aims to both measure and model the optical characteristics of the tilted-nanorod metamaterial. Measuring the optical characteristics involves deter-

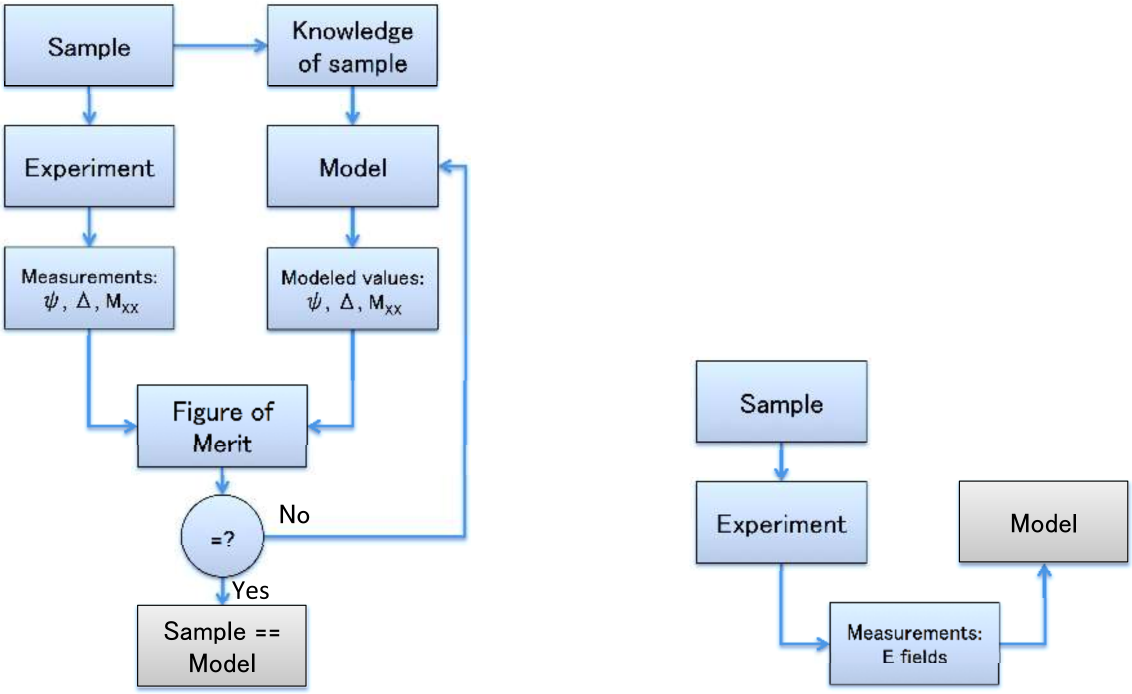

Figure 2. Process of Ellipsometry (left) and PPTE (right). Note that ellipsometry is an iterative process based on the Figure of Merit, while PPTE can determine material parameters in a linear fashion.

mining the permittivity of the material through a technique known as ellipsometry. This technique uses the reflection and transmission of polarized light to determine inherent material characteristics; in this case, the permittivities along the principle axes of the materials [30]. The two separate samples will be measured independently to prove that the two samples are optically distinct, which proves that the underlying physical geometry has a direct effect on the observed optical properties.

In order to understand the behavior of these materials, electromagnetic modeling will be used to determine and analyze the effective characteristics of the nanorods. From these simulations, the effective material parameters will be determined [13]. These effective material parameters can be used to predict the model's behavior outside of the range of the simulation, which can be used to identify areas of interest much faster than performing a wider range of simulations.

1.3 Limits and Challenges

The difficulty in this process is due to the characteristic that makes these materials worth studying: their triclinic behavior. Crystals have been measured and discussed in depth within the ellipsometry community [7, 29, 56, 68], but artificial, structured monoclinic and triclinic materials have only begun to be examined within the last five years. There exists a small body of work, perhaps five to ten pieces [14, 16, 38, 71, 74, 75, 77, 78, 85], which have measured similar structures. This makes the measurements themselves a non-trivial task.

The other difficulty comes in simulating these same materials. The field of effective material parameters is a growing one, but one that has not discussed non-aligned materials. Most of them begin with the assumption that the optical axes are aligned with the lab frame of reference, and move forward from this assumption [64, 83, 99]. This is not possible with the tilted nanorods due to the difference in the optical axes and the laboratory frame of reference [16,38,85], which means that some new method for extracting these materials must be created.

This extraction methodology makes the assumption that the material can be modeled by a homogenous permittivity and permeability tensor. This means that the technique, as presented in this work, cannot be used in materials that exhibit rotation or spatial dispersion. The technique can be easily modified to account for materials exhibiting non-zero optical rotation tensors, but most likely cannot address spatial dispersion. The technique is also presently limited to use within computer simulations, where the exact phase of the field is known and there is no uncertainty.

1.4 Research Strategies

Research was performed in two stages. The first involved using the Infrared Variable Angle Spectral Ellipsometer (IR-VASE), made by J. A. Woollam Co., to measure the effective optical indices of the samples created by Dr. Sarangan and Dr. Shah. Absorptance was determined using a set of measurements using the Air Force Institute of Technology's SOC-100 Hemispherical Directional Reflectometer, an instrument manufactured by Surface Optics Corp. This instrument also measures hemispherical directional transmittance.

The second stage of my research involved creating the Permittivity and Permeability Tensor Extraction (PPTE) technique. This process allows for the extraction of the permittivity and permeability tensor from simulated scattered fields. By building a process which extracts the complete permittivity and permeability tensor, this technique is free from many of the underlying assumptions of other parameter extraction techniques [86], specifically the assumption of the alignment of the optical axes.

The information needed by PPTE is the amplitude and phase of scattered fields. The software FLO_K is used to determine these values from a computer generated scene. FLO_K is a finite-element based computational electromagnetic software developed by Dr. D'Angelo of the Air Force Research Laboratory, Sensors Directorate. The software was developed as part of the Computational Research and Engineering Acquisition Tools and Environments (CREATE) program for expanding the Air Force's ability to perform computer-based simulations [6].

1.5 Dissertation Outline

This document is written in roughly the same order as the research was performed. Chapter II is devoted to the field of ellipsometry [30, 39, 94], which is a niche field of research within optics. The field is often used either to identify optical parameters such as the index of refraction, or to determine physical material properties, such as layer thicknesses [1, 48, 102]. Many people practicing within the field of optics take these determined values for granted, or rely on scientists with experience in the field for making these measurements.

The chapter begins with electric fields, and moves from there to the basics of isotropic ellipsometry. This platform is used as a base to understand Generalized Ellipsometry [81], which is a complexity required to measure highly anisotropic samples [28, 54, 76], such as the ones that prompted this research. Here, the underlying physics of ellipsometry, namely the Four-by-four Matrix Formalism is explained and detailed [79].

Chapter III is focused on the measurements of the original nanorod samples. The IR-VASE of the Air Force Research Laboratory was used to calculate the complex index of the samples along their principle axes, which is the common language for discussing metamaterials. Other optical properties of the materials such as their reflectance and absorptance was found using the SOC-100 HDR. The sample grown at room temperature offered optical characteristics that highly varied between orientations, while the sample grown at cryogenic temperatures offered more consistent optical characteristics, but only at longer wavelengths. The two samples demonstrate unique optical properties, which again proves that there is some relationship between the structures morphology and the optical characteristics.

The fourth chapter begins with the basics of ellipsometry and why it is necessary in a laboratory setting, but not in the world of computational electromagnetics. From these basic differences, the Four-by-four Matrix Formalism is used to go from reflected and transmitted fields to the effective permittivity and permeability information that describes materials. The process I created for performing this is called PPTE, and is detailed in this chapter. PPTE requires the amplitude and phase of scattered field to extract the effective material parameters. The software FLO_K is a finite element based computational electromagnetic solver which is capable of determining these values. The technique is used to examine a plane of known permittivity, an aligned anisotropic material, and a model of the silver nanorods. There was a high degree of accuracy in the permittivities determined in the case of both the plane and the aligned anisotropic material. The nanorod exhibited the expected triclinic characteristics, which predicted the scattered fields of the model with a high degree of accuracy.

Within PPTE, there is one step that has additional complications due to the presence of multiple solutions. The step involves inverting the exponential operator of a complex matrix. This cannot be done correctly without understanding the problem at hand, as well as the physics of its application. A matrix exponential can be calculated by finding the exponential of the eigenvalues, which is not a one-to-one operation. Inverting this operation is possible using a set of assumptions that are discussed within this chapter. The underlying mathematics of this operation are discussed in depth, then several assumptions required to arrive at the correct solution are stated explicitly. These assumptions are then tested against the physics of the problem and shown to be valid assumptions when used within this technique.

Chapter VI takes a step back towards ellipsometry, and takes a critical look at some of the underlying assumptions about the behavior of metamaterials. Certain presumptions have been made extensively regarding the operation of these materials [1,30,79], and the PPTE technique allows for those presumptions to be tested. These presumptions are stated explicitly, then used to identify the characteristics they would impress on the solution to the problem. The method for extracting this information from the results of the PPTE process is detailed and then used to analyze the results. The results show that the classical assumptions about the behavior of these materials are not as well understood as previously assumed. The simple presumed geometric transformations are at best approximations of the actual material behavior, as the tensors extracted from the nanorods indicated that the geometric transformations would need to be wavelength dependent to determine the correct material tensor from the permittivities of the optical axes.

This document achieves the goals stated previously. The experimental characteristics of these materials are determined using Generalized Ellipsometry. Using the underlying mechanics of the Generalized Ellipsometry, a new parameter extraction technique, PPTE, is derived and detailed in depth. This technique is shown to simply and accurately characterize complex materials. The step of PPTE involving multiple roots is analyzed from a physical point of view, which allows for the determination of the correct solution, which is shown to be possible within PPTE. Finally, PPTE is used to examine the previous presumptions about material behaviors.

This document benefits the scientific community as a whole in several ways. The first is by contributing a set of measurements to the community studying tilted-nanorods. This comparative study clearly links the optical characteristics of the material with the underlying geometry, an observation that had not been demonstrated previously. In addition, it offers a more efficient way to communicate the details of the structures, which enables communication clarity for future research.

The PPTE technique is a new and more precise way of determining a material's optical properties. This technique uses a small number of simple assumptions to extract the complete material tensor, which has not previously been possible. In addition, it provides a clear mechanism to go between effective material parameters and scattered fields, which allows for a mechanism of testing the predictive power of these extracted parameters. The addition of the inverse exponential operator allows for PPTE to be used with nearly any material, making it a much more general purpose tool than it would be otherwise.

Finally, PPTE allows for the examination of some of the underlying principles of ellipsometry to be examined. This is research that is just now possible due to this extraction methodology, and demonstrates that metamaterials are even more complex than researchers previously assumed. This allows for an even greater flexibility in material design for future materials.

The research presented in this document measures the optical properties and effective material parameters of two separate tilted-nanorod samples. A novel technique applicable to a wide variety of problems is derived to determine the theoretical characteristics of these materials. This allows for the examination of these complex materials from both a physical and theoretical point of view, and will allow for material design opportunities in future research.

II. Ellipsometry

The goal of this research is to identify the characteristics of nanoscopic nanorods. However, the samples make this a difficult task. The samples have been shown to be highly anisotropic [75–77], which makes performing ellipsometry with them much more difficult than for other, simpler samples [30]. Fortunately, the field of Generalized Ellipsometry has arisen to address these difficulties in a systematic fashion [79], and has enabled the measurements of these samples.

Ellipsometry uses polarized light to non-invasively estimate the physical and optical characteristics of a surface [80]. Polarized light is used to illuminate a surface, and the reflected or transmitted light is analyzed by a series of polarizers. The information gleaned from this affected light is used to either directly interpret the macroscopic sample properties, or compared against a model to estimate physical parameters such as layer thicknesses or index of refraction. Over the last several decades, ellipsometry has become a powerful and widely used tool to quickly and efficiently measure otherwise obscure characteristics [10].

This chapter aims to cover both the theory and practice of ellipsometry, as well as how it was used in this dissertation. The section relating to ellipsometric theory has been divided into two sections: basic ellipsometry and Generalized Ellipsometry. Section 2.2 covers the theory and practice of ellipsometry relating to simple samples, such as isotropic layered media. The following section, Section 2.3, covers the theory of Generalized Ellipsometry, which is necessary for complex samples. It covers the physics necessary for Generalized Ellipsometry, the experimental setups, and material modeling.

2.1 Introduction to Ellipsometry

The underlying principle of ellipsometry is that light is changed upon interacting with matter [26]. The fields might change direction, or change in relative phase, or in amplitude. Most often the field will change in all three quantities [93]. By identifying these relative changes, information pertaining to the interacting matter can be identified. Intangible quantities such as permittivity can be determined, and physical quantities such as thickness can be extracted. This can be hugely helpful in a large number of circumstances, especially when dealing with microscopic and nanoscopic materials, or situations where directly observing these properties would be prohibitively difficult [9, 24, 60, 77].

2.1.1 Fundamental physics of ellipsometry.

Light is polarized [19]. Each and every photon has an electric field which oscillates in some direction while moving through space. In many cases, the polarization of light can be ignored. When there are many photons with random polarizations, the effects of being polarized are unobservable due to the enormous number of randomly oriented particles [33]. The polarization of these particles is irrelevant while moving through free-space; the direction of their oscillation makes no difference while they are moving in straight lines at the speed of light [37].

But, when a photon interacts with matter, suddenly polarization matters. When a photon strikes a surface, the polarization determines whether it will be reflected off the surface or be coupled into the material [41]. When inside some materials, the polarization determines how long it will take for the photon to reach the other side [4]. When two photons are traveling in the same direction, the polarization will determine if they destructively interfere or are observed as being twice as bright as a single photon [37].

Ellipsometry characterizes and quantifies all of these effects, and uses them to tell us something about the materials with which the light interacts. For example, the permittivity of the material determines how much light of each polarization is reflected, which implies that recording these polarizations can provide meaningful information about the permittivity of a material. Constructive and destructive interference can be used to relay information about layer thickness. Using much more complicated models, ellipsometry can be used to identify the orientation of crystal lattices without ever observing the crystal.

Since conception, ellipsometry has been a powerful tool for extracting material parameters in a non-invasive fashion [48]. It has been used time and time again to extract very precise parameters while doing nothing more than observing reflected and transmitted light from a sample. Two angles, Ψ and Δ, which define the shape of the reflected or transmitted light, are measured by the instrument [102]. These angles are compared with computer generated models of the material, and used to calculate the parameters of the model which best match the measured data. When the measured and modeled data reach a good agreement, it can be assumed that both the model and the material share the same parameters.

2.1.2 History.

Paul Drude is widely considered to be the father of all ellipsometry [96]. He was the one to link the change in polarization to the physical properties of the sample during his doctoral research in 1887 [96]. Vedam notes that Drude observed this while working on his dissertation, “Reflection and refraction of light at the boundaries of absorbing crystals,” when he observed that the polarization properties of the crystals being measured were a function of time. His investigation into this property revealed that it was due to an oxide layer forming on the crystals. He worked through the equations governing the polarization properties of thin films, and discovered many of the equations used today in ellipsometry.

After this episode, he turned his research into discovering the optical characteristics of many metals and alloys [80]. Drude's work, in 1890, yielded numbers that are in close agreement to those of Palik, who performed his research nearly 100 years later. While his method was very accurate, it was orders of magnitudes slower than the methods used today [30]; Drude spent hours making measurements at a mere two wavelengths.

The field of ellipsometry yielded very little growth over the next sixty plus years; hampered by the mechanical nature of the instruments and the difficulties in analyzing the data. The personal computer changed both of these things; it automated the operation of the ellipsometer and allowed for much easier data analysis [103]. Aspnes and Studna were some of the pioneers in the field of spectroscopic ellipsometry [8], and created an instrument capable of extracting 200 parameters (complex permittivity as a function of wavelength) at 100 wavelengths simultaneously. These instruments still tended to be slow, taking on the order of an hour to run per sample.

The next major breakthrough in the field happened merely five years later, when Muller and Farmer created one of the first ellipsometers which can be used for real time data extraction [63]. Their instrument was capable of capturing four times as many wavelengths, and operated orders of magnitude faster. Aspnes and Studna's instrument operated on the order of hours; their's operated on the order of fractions of a minute.

A few years after this, the field of ellipsometry expanded rapidly. Fujiwara notes that this increase is due to the proliferation of commercial devices around this time [30]. Ellipsometry had been known to be a powerful analysis tool, but its difficulty of use had prevented it from being widely used. The availability of commercial, off-the-shelf instruments capable of making ellipsometric measurements opened the field to nearly everyone.

One of the latest additions to the field, and certainly the one most pertinent to this research, came in 1998, when Schubert published a paper detailing the four-by-four matrix formalism [79]. Before this, ellipsometry had relied on the assumption that one polarization state would not excite the other. Schubert's work freed ellipsometry from this assumption, and widely expanded the field of materials that could be studied.

Today, ellipsometry instruments have reached most of their potential [102]. There is less work being performed on how to build faster and more accurate ellipsometers, because the instruments today are very good [48]. A typical ellipsometer is capable of surveying wide wavelength ranges, with measurement times that range from minutes to fractions of an hour. These measurements have proven time and time again to be highly accurate, and are in good agreement with traditional measurement methods.

2.2 Basic Ellipsometry

This section is aimed at describing the fundamentals of ellipsometry. There are many measurements and descriptors that are unique to ellipsometry, and need to be understood to understand the measurements that are being made. The basics of polarized light are discussed in this section, then applied in order to understand the most basic case of ellipsometry: a material that is both homogenous and isotropic. There are some situations where non-homogenous materials can be be modeled, which will be covered later in the section. However, the assumption of isotropy will be held through this entire section. Understanding the ellipsometry of an isotropic case is paramount to understanding anisotropic ellipsometry, which is the primary goal of this research.

2.2.1 Physics of ellipsometry.

The angles Ψ and Δ are where most people begin their familiarization with ellipsometry. These angles are related to the complex coefficient of reflection ρ of a material, which can be used to extract a huge number of physical parameters. But what exactly are these angles? How is any information extracted from a reflection or transmission coefficient? This portion of the document is used to explain the origin and uses of these angles, and how the reflection and transmission of a sample is related to with the properties that ellipsometry extracts.

Polarized light.

Ellipsometry is the study of how polarized light is affected by interacting with a sample [94]. Therefore, the best place to start understanding ellipsometry is with a discussion about polarized light. Ultimately, light is a solution to Maxwell's equations. Jackson [41] gives Maxwell's equations without sources as

$$\nabla \cdot \boldsymbol{B} = 0 \tag{1}$$

$$\nabla \cdot \boldsymbol{D} = 0 \tag{2}$$

$$\nabla \times \boldsymbol{E} + \frac{\partial}{\partial t}\boldsymbol{B} = 0 \tag{3}$$

$$\nabla \times \boldsymbol{H} - \frac{\partial}{\partial t}\boldsymbol{D} = 0 \tag{4}$$

where $\boldsymbol{E}$ is the electric field, $\boldsymbol{B}$ is the magnetic induction field, $\boldsymbol{D}$ is the electric displacement field, and $\boldsymbol{H}$ is the magnetic field. If one assumes that $\boldsymbol{E}$ exhibits harmonic time dependence $\exp(-i\omega t)$, where t is time and ω is the angular frequency of the field, then these equations can be solved to give the electric field and magnetic induction field as

$$\boldsymbol{E}(\boldsymbol{r},t) = \boldsymbol{E}_0 \exp\left[i\boldsymbol{k}\cdot\boldsymbol{r} - i\omega t + \varsigma\right] \tag{5}$$

$$\boldsymbol{B}(\boldsymbol{r},t) = \boldsymbol{B}_0 \exp\left[i\boldsymbol{k}\cdot\boldsymbol{r} - i\omega t + \varsigma\right] = \left(\sqrt{\mu\epsilon}\hat{k} \times \boldsymbol{E}_0\right) \exp\left[i\boldsymbol{k}\cdot\boldsymbol{r} - i\omega t + \varsigma\right] \tag{6}$$

where $\boldsymbol{r}$ is the position vector in space, $\boldsymbol{k}$ is the wave vector, ς is the field's phase delay, μ is the magnetic permeability, and ϵ is the electric permittivity. $\boldsymbol{E}_0$ is the direction and amplitude of the E field, while $\boldsymbol{B}_0$ is the same for the B field. Any wave which can be written in this form of (5) is considered to be linearly polarized. Notice that, if needed, the phase delay can be incorporated into the $\boldsymbol{E}$ and $\boldsymbol{B}$ terms by making them complex. This is done frequently throughout the rest of the document, thus it should be assumed that all E fields in this document are complex valued.

Due to the principle of superposition, many of these solutions can exist within the same space [41]. Any combination of fields sharing the same direction of propagation (or the opposite direction) can be expressed as the sum of two independent E fields which are polarized perpendicularly to each other. This simplified E field can be thought of as a single E field which exhibits elliptical polarization.

Elliptical polarization can be deconstructed into several simpler cases. For example, if both of the perpendicular fields share the same phase delay ς, the field will behave as a single linearly-polarized wave. If the two waves have the same amplitude, E_0, and one has a phase delay of $+\pi/2$ with respect to the other, the wave is circularly polarized, specifically right-hand circular [39]. If the phase delay is $-\pi/2$, it is still circularly polarized, only now it is referred to as left-hand circular. In general, the two fields will have different amplitudes and phases, and are simply called elliptically polarized. An example of two perpendicular fields being combined into an elliptically polarized field can be seen in Figure 3.

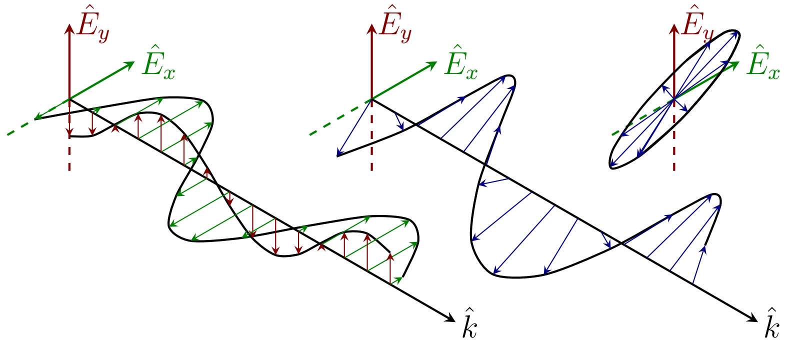

Figure 3. Any combination of purely monochromatic light waves sharing the same (or antiparallel) direction of propagation can be thought of as elliptically polarized light.

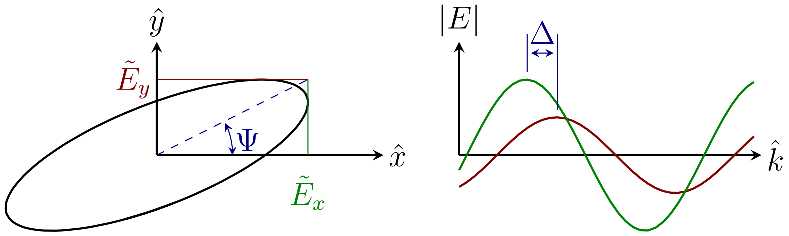

Figure 4. Elliptically polarized light viewing into the direction of propagation. Ψ and Δ are related to the geometry of the ellipse. Δ is the difference in phase between the two waves, and is not intuitively interpretable from the shape of the ellipse.

Ψ, Δ, and ρ.

The shape of any arbitrary ellipse can be fully defined using two parameters. In ellipsometry, the two defining parameters are two angles: Ψ and Δ [10]. These two angles are easily found knowing the E field of the wave. The angle Ψ is the angle of the peak amplitude of the E field. Assuming that the two perpendicular components of the field have amplitudes E_x and E_y, Ψ is given by $\arctan(E_y/E_x)$. The angle Δ is given by $\angle E_x - \angle E_y$. An example of this is shown in Figure 4.

Determining these two parameters in theory is remarkably simple. However, measuring these values in practice is much more difficult. Δ can be directly determined from the shape of the ellipse using a significant amount of geometry, but this is not how Δ is measured in practice. Practically measuring Ψ and Δ will be covered in the following section.

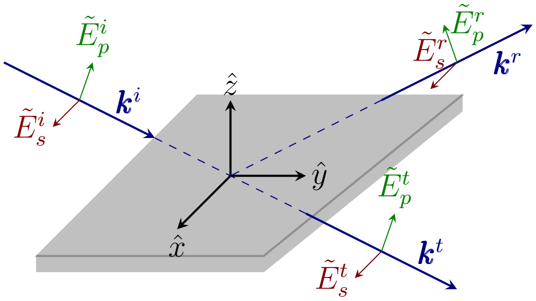

Figure 5. Directions of s and p polarization for a planewave with direction $\boldsymbol{k}$. The direction of the p polarization is preserved upon reflection while s is not. i indicates the incident wave, r represents the reflected wave, and t indicates the transmitted wave.

A third value that is the basis of all ellipsometry can now be discussed. This value is known as the complex coefficient of reflection, and is frequently denoted as ρ. Because this value deals with the interaction of a lightwave with some surface, it is worthwhile to begin discussing polarization with respect to the plane of the surface. The commonly used notation is s and p polarization. The s polarization is short for "parallel" polarization, and is the polarization state in which the E field is parallel to the plane of incidence, formed by the direction of propagation and the sample normal. The s polarization, which is short for "senchreckt", the German word for perpendicular, is the polarization state which is perpendicular to both p polarization and the direction of propagation ($\hat{k} \times \hat{E}_p$). The direction of the s polarization state is preserved upon reflection, while the p polarization state is not. This is shown in Figure 5.

The sample will reflect some portion of the incident light. The amount of light reflected can be described in two ratios: reflected s polarized light over incident s polarized light, and the same for p polarization. ρ is the ratio of these two polarizations, and is defined by

$$\rho = \frac{E_p^r / E_p^i}{E_s^r / E_s^i} \equiv \frac{r_p}{r_s}. \tag{7}$$

If it is assumed that both polarizations of incident light are equal and in phase with each other (linearly polarized at +45°), then ρ describes the elliptically polarized light reflected from the sample. It can then be expressed using Ψ and Δ:

$$\rho = \tan \Psi \exp(i\Delta). \tag{8}$$

2.2.2 Making ellipsometric measurements.

Making measurements of the angles Ψ and Δ is a nontrivial process. There are several different methods from extracting these parameters. The oldest, and now least common, is known as null-ellipsometry, and will be briefly covered here. The null-ellipsometer was chosen due to its intuitive nature and simplicity. More recent ellipsometers operate in a different fashion which makes them much more difficult to grasp their operating concepts. The addition of measurements as a function of wavelength makes their operation even more complicated (see the section on ellipsometers in Fujiwara's work [30]). Some examples of feature extraction will also be given here to show how ellipsometry extracts physical properties from ellipsometric data.

Experimental setups.

The goal of ellipsometry is to extract sample characteristics in a noninvasive manner. Polarized light is generated and used to illuminate the sample. The reflected specular light is then analyzed by a second set of polarizers [26]. This is demonstrated in Fig. 6. This light is then processed by a computer in order to calculate ratios of the r_s and r_p. These ratios are compared to user-generated models to estimate the inherent properties of the sample, such as layer thickness or index of refraction.

The first ellipsometer built is now known as a null-ellipsometer. The ellipsometer contains the same elements found in ellipsometers today, but operates in a much different manner. Today, ellipsometers typically operate with only a single rotating element, which rotates at a constant rate while a detector records the reflected or

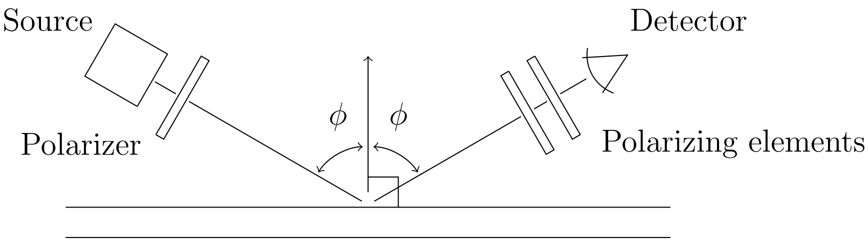

Figure 6. Example of a null-ellipsometer. A blackbody source is frequently used as the source, while an FTIR often detects the reflected intensities.

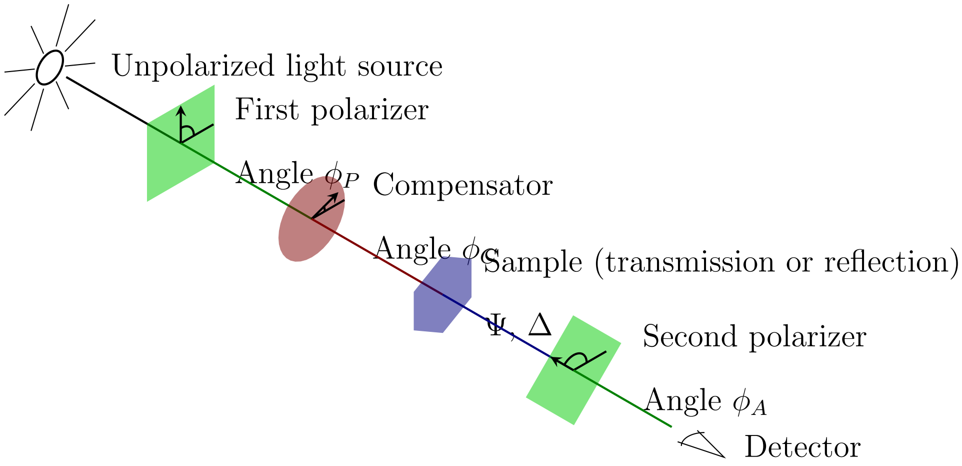

Figure 7. Functional diagram of a null ellipsometer. The analyzer is rotated to minimize the observed power.

transmitted light's intensity [8]. In a null-ellipsometer, there are two elements which are rotated: a compensator (typically a quarter-wave plate) and an analyzer polarizer. These two elements are rotated independently until the detected light is at a minimum (optimally, zero). A diagram of a null-ellipsometer is shown in Figure 7.

The optical train of such a device is simple. An unpolarized or partially polarized light source is transformed into linearly polarized light through the use of a polarizer. This light is transmitted through a compensator at some angle ϕ_C. From here, the light is either reflected or transmitted through the sample in question. The modified light is passed through a second polarizer at some angle ϕ_A. The amplitude of the light is observed after this optic.

Fujiwara gives the amplitude of the observed E field [30] as

$$\begin{aligned} E_{\mathrm{NE}} = {} & r_p \cos\phi_A \left[\cos\phi_C \cos(\phi_P - \phi_C) - \rho_c \sin\phi_C \sin(\phi_P - \phi_C)\right] \\ & + r_s \sin\phi_A \left[\sin\phi_C \cos(\phi_P - \phi_C) + \exp(i\varsigma_C) \cos C \sin(\phi_P - \phi_C)\right] \end{aligned} \tag{9}$$

where E_A is the observed intensity, r_p and r_s are the reflection ratios given in (7), and ς_C is the phase shift of the compensator. A quarter-wave plate is typically used as the compensator, which delays the phase of part of the wave by $\pi/2$. Ergo, $\exp(i\varsigma_C) = -i$. The angle of the compensator (ϕ_C) is held fixed during the experiment, and is generally chosen to be $\pi/4$. This makes the above equation

$$\begin{aligned} E_{\mathrm{NE}} = {} & r_p \cos\phi_A \left[\cos(\pi/4) \cos(\phi_P - \pi/4) + i \sin(\pi/4) \sin(\phi_P - \pi/4)\right] \\ & + r_s \sin\phi_A \left[\sin(\pi/4) \cos(\phi_P - \pi/4) - i \cos(\pi/4) \sin(\phi_P - \pi/4)\right] \\ = {} & r_p \cos\phi_A \left[\cos(\phi_P - \pi/4) + i \sin(\phi_P - \pi/4)\right] \\ & + r_s \sin\phi_A \left[\cos(\phi_P - \pi/4) - i \sin(\phi_P - \pi/4)\right] \end{aligned} \tag{10}$$

During the experiment, the first and second polarizers are rotated until the observed intensity is at a minimum, ideally 0. When this occurs, E_{NE} is equal to zero, and Equation (10) can be rewritten in terms of $r_s/r_p = \rho$ as

$$\begin{aligned} & r_p \cos\phi_A \left[\cos(\phi_P - \pi/4) + i \sin(\phi_P - \pi/4)\right] \\ & \quad = -r_s \sin\phi_A \left[\cos(\phi_P - \pi/4) - i \sin(\phi_P - \pi/4)\right]. \end{aligned} \tag{11}$$

Therefore,

$$\frac{r_p}{r_s} = -\frac{\sin\phi_A \left[\cos(\phi_P - \pi/4) - i \sin(\phi_P - \pi/4)\right]}{\cos\phi_A \left[\cos(\phi_P - \pi/4) + i \sin(\phi_P - \pi/4)\right]}, \tag{12}$$

and

$$\rho = \tan\Psi \exp(i\Delta) = -\tan\phi_A \frac{1 - i\tan(\phi_P - \pi/4)}{1 + i\tan(\phi_P - \pi/4)}. \tag{13}$$

Using the identity

$$\exp(-i2\phi) = \frac{1 - i\tan\phi}{1 + i\tan\phi}, \tag{14}$$

Ψ and Δ can be shown to be

$$\Psi = -\phi_A \tag{15}$$

$$\Delta = -2\phi_P + \pi/2. \tag{16}$$

This method was how Drude originally performed ellipsometry [10]. Null-ellipsometry is much easier to understand than other forms of ellipsometry, and allows for ellipsometry to be performed without the aid of a computer, or even an electronic detector. The modern methods of ellipsometry are aided by computers, and use more complicated methods of extracting Ψ and Δ, and other polarization information in many cases. These setups and further abilities will be discussed later in both the following section and Section 2.3.2.

Angles Ψ and Δ of λ.

Note that the null-ellipsometer is only capable of making measurements at a single wavelength. While ellipsometry at a single wavelength can often be of use, it is often more useful to make ellipsometric measurements at a range of wavelengths. This enables the extraction of some parameters, such as the complex index of refraction as a function of wavelength, and increases accuracy in others, such as layer thickness [94].

Several other ellipsometer setups have been created which use broadband sources and optics, and are capable of making wavelength dependent ellipsometric measurements. Fujiwara's work "Spectroscopic Ellipsometry" [30] has an in-depth survey and discussion of many different types of ellipsometers in his Section 4.2. Here, the ellipsometer setup used throughout this document will be briefly discussed.

The Infrared Variable Angle Spectral Ellipsometer (IR-VASE) is an FTIR-PSC$_\mathrm{R}$A ellipsometer [1]. FTIR stands for "Fourier Transform Infrared", which refers to the light source and method of spectroscopy being used. PSC$_\mathrm{R}$A indicates the optical train of the system, which is a polarizer, the sample, a rotating compensator, then an analyzing polarizer. The compensator is the only rotating part of the system.

The FTIR is used in the same way as it is in spectroscopy. A broadband source (a tungsten filament in the IR-VASE) is split, then interfered with itself in order to create an interferogram as a function of mirror displacement [91]. This light passes through a polarizer (most broadband sources are unpolarized) before it is reflected or transmitted from the sample. During the movement of the interfering mirror, the compensator is held at one angle. The light is observed by a detector, which is then processed by a computer to arrive at a spectral measurement.

Disregarding the spectral component of the wavelength, a generic PSC$_\mathrm{R}$A works by rotating the compensator and recording the intensity. Fujiwara gives the observed E field of the ellipsometer [30] as

$$E_\mathrm{C} = \left(\cos^2\phi_C - i\sin^2\phi_C\right)\sin\Psi\exp(i\Delta) + (1+i)\cos\phi_C\sin\phi_C\cos\psi \tag{17}$$

where ϕ_C is the angle of the compensator (in this case, a quarter wave plate), and the angle of the polarizer and analyzer are 45° and 0°, respectively. The normalized observed intensity at the detector would then be

$$\begin{aligned} I/I_0 = 2 - \cos 2\Psi& \\ &+ \sin 2\phi_C \times 2\sin 2\Psi \sin\Delta \\ &- \cos 4\phi_C \times \cos 2\Psi \\ &+ \sin 4\phi_C \times \sin 2\Psi \cos\Delta. \end{aligned} \tag{18}$$

As the breakout of the above equation shows, the ellipsometric quantities can be determined by treating the measured signal as a sum of sines and cosines. Knowing this, the two ellipsometric parameters can be found by simply measuring as few as four points over the course of the rotation of the optic.

What is so powerful about this analysis is that it has no wavelength dependence, and can therefore be used to measure Ψ and Δ as a function of wavelength with no increase in measurement time [72]. The only things that still need to be accounted for are the lack of perfect polarizers (a problem inherent in any measurement) and the lack of broadband compensators. However, similar mathematics can be performed if the phase delay of the compensator is known, and used to find the extraction equations for the non-ideal case.

Because most of the mathematical equations involving Ψ and Δ are not wavelength dependent, this dependence will be largely ignored through the rest of this section. The mathematics will be derived for a single wavelength based on the knowledge that it can be easily extended over the range of wavelengths in question.

n and k extraction.

The Ψ and Δ angles can be used to directly extract the effective complex index of refraction of the sample. It is assumed that the sample is infinitely large, perfectly flat, and the measured component of the wave is only due to the surface reflection of the sample. The values of Ψ and Δ can be used to calculate the complex reflection coefficient ρ using the equation

$$\rho = \frac{r_p}{r_s} = \tan\Psi\exp(i\Delta).$$

Here, r_s and r_p represent the complex reflection coefficients from the s and p polarized light incident on the sample. These values can be described using the angle of incidence, θ, the real portion of the index of refraction n, and the imaginary portion of the index of refraction k. For simplicity, the following equations will use the complex index of refraction $N = n + ik$ [19].

$$r_s = \frac{\cos\theta - \sqrt{N^2 - \sin^2\theta}}{\cos\theta + \sqrt{N^2 - \sin^2\theta}} \tag{19}$$

$$\begin{aligned} r_p &= \frac{1/\cos\theta - N/\sqrt{1 - \sin^2\theta/N^2}}{1/\cos\theta + N/\sqrt{1 - \sin^2\theta/N^2}} \\ &= \frac{\sqrt{N^2 - \sin^2\theta} - N^2\cos\theta}{\sqrt{N^2 - \sin^2\theta} + N^2\cos\theta} \end{aligned} \tag{20}$$

Substituting these two equations into (19), the complex reflectance can be written as

$$\begin{aligned} \rho &= \frac{\left(\sqrt{N^2 - \sin^2\theta} - N^2\cos\theta\right)\left(\cos\theta + \sqrt{N^2 - \sin^2\theta}\right)}{\left(\sqrt{N^2 - \sin^2\theta} + N^2\cos\theta\right)\left(\cos\theta - \sqrt{N^2 - \sin^2\theta}\right)} \\ &= \frac{\left[N^2 - \sin^2\theta - N^2\cos^2\theta\right] - \left[(1 - N^2)\cos\theta\sqrt{N^2 - \sin^2\theta}\right]}{\left[N^2 - \sin^2\theta - N^2\cos^2\theta\right] + \left[(1 - N^2)\cos\theta\sqrt{N^2 - \sin^2\theta}\right]} \equiv \frac{U + V}{U - V}. \end{aligned} \tag{21}$$

where

$$U = N^2 - \sin^2\theta - N^2\cos^2\theta \tag{22}$$

$$V = (N^2 - 1)\cos\theta\sqrt{N^2 - \sin^2\theta}. \tag{23}$$

A new variable W can be defined as the ratio between U and V.

$$\begin{aligned} W = \frac{U}{V} &= \frac{N^2 - \sin^2\theta - N^2\cos^2\theta}{(1 - N^2)\cos\theta\sqrt{N^2 - \sin^2\theta}} \\ &= \frac{N^2 - \sin^2\theta - \cos^2\theta + \cos^2\theta - N^2\cos^2\theta}{(1 - N^2)\cos\theta\sqrt{N^2 - \sin^2\theta}} \\ &= \frac{-(1 - N^2) + (1 - N^2)\cos^2\theta}{(1 - N^2)\cos\theta\sqrt{N^2 - \sin^2\theta}} \\ &= \frac{\cos^2\theta - 1}{\cos\theta\sqrt{N^2 - \sin^2\theta}} = \frac{\sin\theta\tan\theta}{\sqrt{N^2 - \sin^2\theta}} \end{aligned} \tag{24}$$

By squaring both sides, N^2 can easily be found in terms of W and θ.

$$W^2 = \frac{\sin^2\theta\tan^2\theta}{N^2 - \sin^2\theta} \tag{25}$$

therefore

$$N^2 = \sin^2\theta\left[1 + \frac{\tan^2\theta}{W^2}\right]. \tag{26}$$

From Equation (21), W can be found in terms of ρ:

$$\begin{aligned} \rho = \frac{U + V}{U - V} &= \frac{1 + W}{1 - W} \\ W &= \frac{\rho + 1}{\rho - 1}. \end{aligned} \tag{27}$$

This can be substituted into (26) to find N in terms of ρ and θ.

$$N = n + ik = \sin\theta \left[1 + \left(\frac{\rho - 1}{\rho + 1} \right)^2 \tan^2\theta \right]^{1/2} . \tag{28}$$

It is important to note what this is actually measuring. These measurements assume that the only light reflected from the sample (in the specular direction) is due to a Fresnel reflectance at the surface. This is not a measure of the actual n and k of the sample; instead it is the required n and k that an infinitely thick, infinitely long planar material would need to have to create the Ψ and Δ measured.

2.2.3 Ellipsometric modeling.

Layer thickness, layer permittivity, and layer composition are the three attributes that are most frequently extracted from ellipsometric data. Unlike the index extraction detailed above, none of these properties are directly extractable from the measured data. Models of the material need to be created and compared to the measured data. Due to the linear nature of light, the reflectance and transmittance of a layer can be found knowing the permittivity of the material. Calculating the permittivity is done using one of several models. If the permittivity is unknown, there are permittivity models based on oscillators which can be fit to the measured data. If the materials of the layer are known, then an effective medium can be used to calculate the volume fraction. All of these will be described in the proceeding sections.

Calculating layer thickness.

In most applications, the effective index of the material is not aim of the measurement. Ellipsometry is typically used in industry in order to non-invasively measure material parameters that would otherwise be difficult to measure. One of the more common measurements, for example, is layer thickness. Many applications of multi-

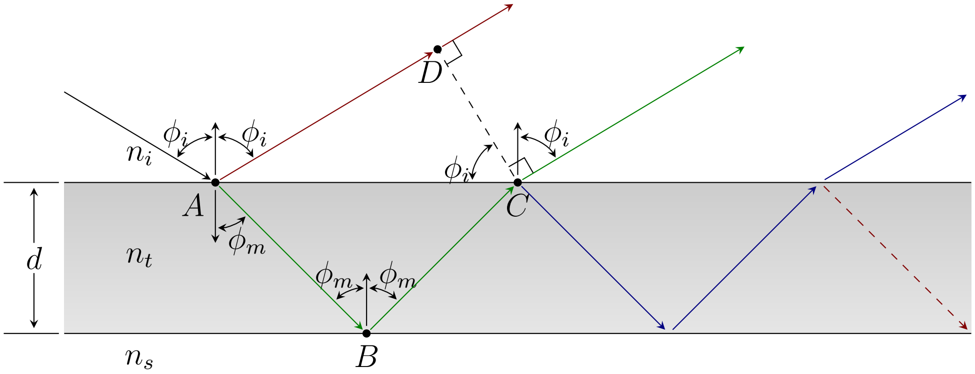

Figure 8. Diagram of a thin-film problem composed of infinite, perfectly flat planes. ϕ_i is the angle of incidence, while ϕ_m is the angle of propagation within the media. The light reflects off the substrate, leading to an infinite summation.

layered material rely on precise layer thickness in order to achieve the desired optical parameters. This is not something that can be directly measured with ellipsometry, but these parameters are extractable using a model.

Closed-form solutions for the complex coefficient of reflection can be found for simple cases, such as a single layer of some material on top of a substrate. This allow for the extraction of the layer thickness from the ellipsometry measurements. Take, for example, a layer of thickness d and index n_t on top of a substrate with index n_s, as seen in Figure 8. (Both of these indexes are allowed to be complex; the difference between N and n will be addressed where appropriate.) Note that the thickness of the substrate is not taken into account; it is assumed that all light that enters the substrate is absorbed or transmitted out of the system.

There are two boundaries present in this problem. The reflectances at each boundary for each polarization state can be found to be

$$r_s^{im} = \frac{n_i \cos\theta_i - n_m \cos\theta_m}{n_i \cos\theta_i + n_m \cos\theta_m} \tag{29}$$

$$r_s^{ms} = \frac{n_m \cos\theta_m - n_s \cos\theta_s}{n_m \cos\theta_m + n_s \cos\theta_s} \tag{30}$$

$$r_p^{im} = \frac{n_m \cos\theta_i - n_i \cos\theta_m}{n_i \cos\theta_i + n_m \cos\theta_m} \tag{31}$$

$$r_p^{ms} = \frac{n_s \cos\theta_m - n_m \cos\theta_s}{n_s \cos\theta_m + n_m \cos\theta_s} \tag{32}$$

where θ_i is the angle of incidence and Snell's law [37] gives

$$n_i \sin\theta_i = n_m \sin\theta_m = n_s \sin\theta_s. \tag{33}$$

The initial ray will strike the deposited material; r^{im} of it will be reflected, and the rest will enter into the material. After traveling an effective distance δ through the medium (the higher index affects the phase of the ray), it will strike the boundary in-between the material and the substrate. Here, r^{ms} will be reflected back into the material, while $1 - r^{ms}$ will enter into the substrate. Again, some of the light will be transmitted out of the material ($-r^{im}$), while some will be reflected into the material to repeat the process again.

The total reflection is then the sum of all of the reflected rays. However, there is one more effect to take into account: interference. These waves will be added together and interfere with one another. In order to properly calculate this effect, the phase difference between rays must be known. This is straightforwardly calculated knowing the geometry of the problem.

The difference in phase between the two wavefronts (the reflected wavefront and the refracted wavefront) can be found as the difference in phase between the longer path ($\bar{A}B + \bar{B}C$) minus that of the reference phase $\bar{A}D$ (see Figure 8). The path length of the refracted path is given by

$$\overline{AB} + \overline{BC} = \frac{2d}{\cos\theta_m}. \tag{34}$$

This gives a difference in phase of $2kn_m d/\cos\theta_m$.

The path length of the reflected wave is the projection of the length $\overline{AC}$ onto the path $\overline{AD}$. The length $\overline{AC}$ is given by

$$\overline{AC} = 2d\tan\theta_m. \tag{35}$$

This forms the hypotenuse of the triangle ACD. The length $\overline{AD}$ is then given by

$$\overline{AD} = \overline{AC}\sin\theta_i = 2d\tan\theta_m\sin\theta_i. \tag{36}$$

The phase of this reflection is then $2n_i d\tan\theta_m\sin\theta_i$. There is one further simplification to make which makes use of Snell's law. Using (33),

$$\overline{AD} = 2d\tan\theta_m\sin\theta_i = 2d\tan\theta_m\frac{n_m\sin\theta_m}{n_i} = 2d\frac{n_m}{n_i}\frac{\sin^2\theta_m}{\cos\theta_m}, \tag{37}$$

which makes the phase simply $2kn_m d\frac{\sin^2\theta_m}{\cos\theta_m}$. The difference in phase between the two wavefronts is then

$$\delta\varsigma = 2kn_m d\frac{1}{\cos\theta_m} - 2kn_m d\frac{\sin^2\theta_m}{\cos\theta_m} = 2kn_m d\cos\theta_m. \tag{38}$$

The total reflection coefficient can now be found. The total reflection coefficient is

$$\begin{aligned} r^t = {} & r^{im} \\ & + (1 - r^{im}) r^{ms} (1 + r^{im}) e^{i\delta\theta} \\ & + (1 - r^{im}) r^{ms} \left[(1 - r^{im}) r^{ms} \right] (1 + r^{im}) e^{i2\delta\theta} \\ & + (1 - r^{im}) r^{ms} \left[(1 - r^{im}) r^{ms} \right]^2 (1 + r^{im}) e^{i3\delta\theta} + \cdots \end{aligned} \tag{39}$$

$$= r^{im} + \left(1 - (r^{im})^2\right) r^{ms} e^{i\delta\theta} \sum_{\mathtt{m}=0}^{\infty} \left[(1 - r^{im}) r^{ms} \right]^{\mathtt{m}} e^{i\mathtt{m}\delta\theta} \tag{40}$$

r_s^t and r_p^t are calculated separately, but with the same equation. Each line of (39) is another wavefront reflected off of the material-substrate boundary. This infinite series is a geometric series which converges to

$$r^t = r^{im} + \frac{\left(1 - (r^{im})^2\right) r^{ms} e^{i\delta\theta}}{1 - (1 - r^{im}) r^{ms} e^{i\delta\theta}} \tag{41}$$

when $|(1 - r^{im}) r^{ms}| < 1$, a property guaranteed by the physics of the problem.

Modeling layers.

The goal of ellipsometry is ultimately to determine the physical characteristics of a layer. When the details of a layer are well known, the physical attributes of a layer, such as layer thickness, can be determined from the measurements. However, there are many times when the layer properties are not known. This can be due to a number of reasons. Sometimes, a single layer is composed of multiple materials. Other times, the layer properties are the parameter being extracted from the measurement. This section will discuss some of the ways of modeling layer materials when the properties of the layers are not known.

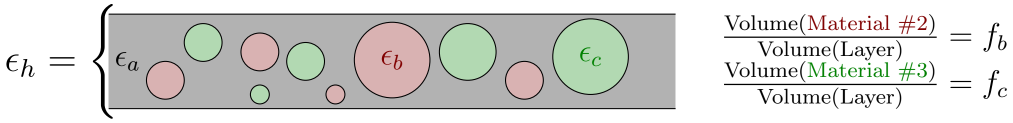

Figure 9. Diagram of a layer which can be modeled as an effective medium. The relative size of the particles can be shown to be irrelevant to the effective permittivity.

Effective Medium Approximation. One of the most common inhomogenous layers is known as the Effective Medium Approximation (EMA). This theory was originally used to calculate the effective permittivity of a first material with spherical particles of a different material imbedded inside the layer [90]. This is shown in Figure 9. It has been shown to be a useful model of a huge number of other materials [7,9,29].

The effective permittivity, ϵ_h, is derived by finding the polarizability of the layer as a whole, and using the relationship between the polarizability and permittivity to find the effective permittivity. For a spherical particle in a vacuum with polarizability α and number of electrons η, the polarization P can be expressed as [93]

$$P = E\frac{\eta\alpha}{1 - 4\pi N\alpha/3}. \tag{42}$$

The effective permittivity can be expressed as [93]

$$\epsilon_h = 1 + \frac{P}{\epsilon_0 E}. \tag{43}$$

Combined with the Equation (42), the effective permittivity of this spherical particle can be shown to be

$$\epsilon_h = 1 + \frac{1}{\epsilon_0}\frac{\eta\alpha}{1 - 4\pi\eta\alpha/3}. \tag{44}$$

This can be rewritten in terms of $\eta\alpha$ as

$$\frac{\epsilon_h - 1}{\epsilon_h + 2} = \frac{4\pi}{3}\eta\alpha, \tag{45}$$

which is known as the Clausius-Mossotti relation [25].

When there are multiple materials in a single layer, this equation can be rewritten to use the volume fraction of each material to that of the whole:

$$\frac{\epsilon_h - 1}{\epsilon_h + 2} = \frac{4\pi}{3}(\eta_a \alpha + \eta_b \alpha_b) \tag{46}$$

$$= \frac{4\pi}{3}\left[f_a \frac{\epsilon_a - 1}{\epsilon_a + 2} + f_b \frac{\epsilon_b - 1}{\epsilon_b + 2}\right] \tag{47}$$

where $f_{a,b} = \eta_{a,b}/(\eta_a + \eta_b)$ [30]. This gives a simple equation which relates the effective permittivity of the medium in terms of known material parameters and the volume fraction of each material.

Practically, this makes some ellipsometric problems much easier to solve. Instead of needing to solve for the layer permittivity and thickness at the same time (two unknowns per wavelength, and another constant), the problem can be solved using just two unknowns: the layer thickness, and one of the volume fractions. This drastically decreases the solution space.

It is worth noting that several modifications that can be made to this solution. The first is acknowledging the fact that most layers are not principally formed of vacuums. Equations (42) and (43) can easily be adjusted to address this fact, which leads to a new expression for the effective permittivity [94]:

$$\frac{\epsilon_1 - \epsilon_h}{\epsilon_1 + \epsilon_h} = \frac{4\pi}{3} f_a \frac{\epsilon_a - \epsilon_h}{\epsilon_a + 2\epsilon_h} \tag{48}$$

where ϵ_1 refers to the permittivity of the host material, and f_a refers to the ratio of the embedded material (ϵ_a) to the host material.

The previous formula assumes that the host material is known. In many materials, there is not a strong presence of one material relative to the other. In this case, it can be instead assumed that the permittivity of the host material is the same as the effective permittivity. This gives rise to the equation

$$0 = f_a \frac{\epsilon_a - \epsilon_h}{\epsilon_a + 2\epsilon_h} + f_b \frac{\epsilon_b - \epsilon_h}{\epsilon_b + 2\epsilon_h} \tag{49}$$

where the permittivity of the second material is ϵ_b. This is known as the Bruggeman effective medium approximation [20]. This can easily be extended to M constituents,

$$0 = \sum_{m=1}^{M} f_m \frac{\epsilon_h - \epsilon_m}{\epsilon_h + 2\epsilon_m}. \tag{50}$$

Modeling material permittivities.

Another method for modeling layer permittivities is called the homogenous layer approximation [93]. Here, nothing about the layer is assumed. The permittivity of the layer is calculated using a number of free parameters which control the size and shape of different oscillators. These oscillators are modeled after the characteristics of physical processes. In some cases, they can be found using the physical parameters of the material being modeled, but this cannot be applied to many materials. These free parameters are then used as fitting parameters.

Lorentz permittivity model. The Lorentz oscillator is used to describe a single electron, two-level atom [10]. The atoms composing the solid react strongly to certain frequencies, which strongly affects the effective layer permittivity. The Lorentz oscillator can be used to model layers if the atomic properties of the material are known. A material with a single Lorentz oscillator will have effective permittivity defined by three modeling parameters, the oscillator amplitude A, the oscillator widthΓ, and the oscillator center frequency ω_0. This can be calculated as

$$\epsilon_{\text{lorentz}}(\omega) = 1 + \frac{A}{(\omega_0^2 - \omega^2) + i\Gamma\omega}. \tag{51}$$

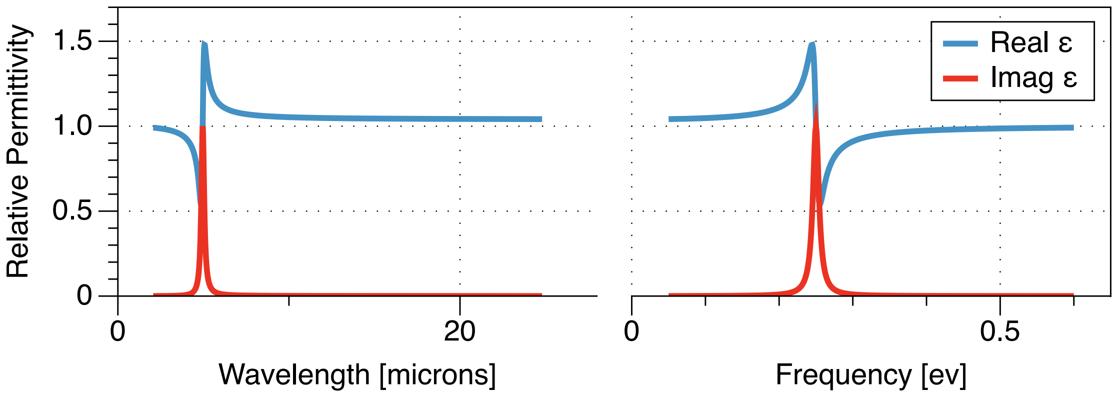

Figure 10. Real and imaginary permittivity of a Lorentz oscillator. The center frequency is 0.25 ev, and the oscillator has an amplitude of 1. $\Gamma = 1$**.**

This is formula (5.7) in [30], where $A = \frac{e^2\eta_e}{\epsilon_0 m_e}$. In the event that there are multiple Lorentz oscillators (which is fairly common), the effective permittivity of the material becomes

$$\epsilon_{\text{combined}}(\omega) = 1 + \sum_{m=1}^{M} \frac{A_m}{(\omega_m^2 - \omega^2) - i\Gamma_m\omega} \tag{52}$$

where M is the total number of Lorentz oscillators. An example of this oscillator is shown in Figure 10.

Drude permittivity model. The secondly frequent used oscillator is the Drude oscillator. This oscillator describes the permittivity of conductors, where electrons can freely travel between atoms. Again, the derivation of the oscillator is beyond the scope of this document, but can be found in [10]. Typically, materials are modeled with only a single Drude term. A material with a single Drude oscillator can be described with two fitting terms from the Lorentz oscillator, A and Γ:

$$\epsilon(\omega) = 1 - \frac{A}{\omega^2 - i\Gamma\omega} \tag{53}$$

An example of this oscillator is shown in Figure 11. These oscillator models are based on oscillator models derived using classical mechanics, and accurately model

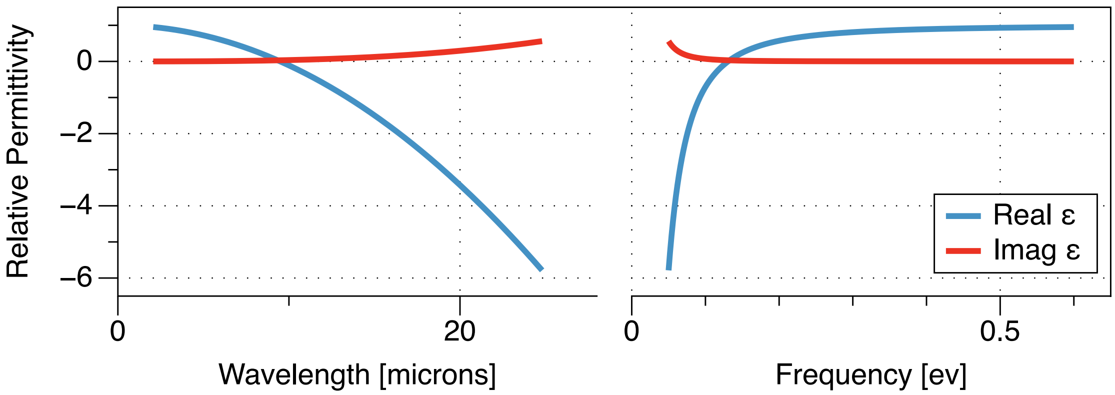

Figure 11. Real and imaginary permittivity of a Drude oscillator. This oscillator has an amplitude of 1 and a Γ of 1.

the behavior of many materials.

Other oscillators. There are many other oscillator models that are used in ellipsometry. The ones detailed here are the ones most often found in the modeling of materials in the infrared. Sellmeir and Cauchy equations are frequently used to model glasses in the visible and UV portion of the spectrum. These models consist of only a real permittivity due to transparent nature of the glasses they model [10]. Other oscillators, such as the Tauc-Lorentz oscillator, are simply simplifications or special cases of the Lorentz oscillator [93].

Complex materials. Oscillators are additive in nature, which means that any number of oscillators can be combined to model a single layer. In the research presented here, the permittivities will be modeled using a single Drude oscillator and two Lorentz oscillators. While more oscillators could be added, this will actually decrease the quality of the Figure of Merit, the χ^2 value (which will be detailed in slightly later in this section). This value is dependent on the number of fitting parameters, and increasing the number of fitting parameters gives a higher value (which indicates a worse fit). These oscillators have been used to give good fits and good χ^2 values, which is why they were used in this research. The full fitting equation for the layer permittivity is

$$\epsilon_{\text{layer}}(\omega) = 1 - \frac{A_d}{\omega^2 - i\Gamma_d\omega} + \frac{A_1}{(\omega^2 - \omega_1^2) - i\Gamma_1\omega} + \frac{A_2}{(\omega^2 - \omega_2^2) - i\Gamma_2\omega} \tag{54}$$

where the fitting terms $\{A_d,\ \Gamma_d\}$ are associated with the Drude oscillator, $\{A_1,\ \omega_1,\ \Gamma_1\}$ are associated with the first Lorentz oscillator, and $\{A_2,\ \omega_2,\ \Gamma_2\}$ are associated with the second.

2.2.4 Figures of merit.

The goal of ellipsometry is to take measured data and model it; it is then assumed that the parameters of the model correspond with the parameters of the measured material. The question that naturally arises out of this is, how close is close? What metric should be used to describe the correlation between measured data and modeled data?

Three metrics have been widely used to answer this question. The oldest of the three is a scaled version of the mean squared error between the two sets of data [30].

$$\sigma_{\text{se}}^2 = \frac{1}{M - F - 1} \sum_{m=1}^{M} \left(\rho_{\text{meas}}(\lambda_m) - \rho_{\text{calc}}(\lambda_m)\right)^2 \tag{55}$$

where M is the number of samples (number of wavelengths tested), F is the number of fitting parameters, ρ_{meas} is the measured ellipsometric data, and ρ_{calc} is the modeled ellipsometric data.

The scaling factor has several implications. The first is, the use of the number of samples encourages, so to speak, measurements with more data points. A well fit measurement with fewer data points would have a higher σ_{se}^2, indicating a poorer fit. The second term in the scaling factor encourages using a fit with fewer parameters.

Any measurement can be perfectly described using an adequate number of fitting functions; the scaling factor increases σ_{se}^2 when adding new fitting parameters does not improve the fit.

A similar version of this function is

$$\xi_{\mathrm{se}}^2 = \frac{1}{2M - F + 1} \sum_{m=1}^{M} \left[\left(\frac{\Psi_{\mathrm{meas}}(\lambda_m) - \Psi_{\mathrm{calc}}(\lambda_m)}{\sigma\Psi(\lambda_m)} \right)^2 + \left(\frac{\Delta_{\mathrm{meas}}(\lambda_m) - \Delta_{\mathrm{calc}}(\lambda_m)}{\sigma\Delta(\lambda_m)} \right)^2 \right] \tag{56}$$

where $\sigma\Psi$ and $\sigma\Delta$ are the standard deviation of the measurements at the given wavelength [30]. This equation gives some benefits compared to (55). The first is that dividing by the standard deviation allows for noisy measurements to have less of an impact on the figure of merit. Another benefit is that Ψ and Δ tend to vary less than ρ, which is equal to $\tan\Psi \exp i\Delta$. This prevents measurements with $\Psi \sim \pi/2$ from falsely inflating the metric.

The final metric that will be discussed here is

$$\chi_{\mathrm{se}}^2 = \frac{1}{2M - F + 1} \sum_{m=1}^{M} \left[\left(\frac{\Psi_{\mathrm{meas}}(\lambda_m) - \Psi_{\mathrm{calc}}(\lambda_m)}{\delta\Psi(\lambda_m)} \right)^2 + \left(\frac{\Delta_{\mathrm{meas}}(\lambda_m) - \Delta_{\mathrm{calc}}(\lambda_m)}{\delta\Delta(\lambda_m)} \right)^2 \right], \tag{57}$$

which is subtly different than the equation for ξ_{se}^2 [30]. χ_{SE}^2 uses $\delta\Psi$ and $\delta\Delta$ instead of $\sigma\Psi$ and $\sigma\Delta$. The δ terms refer to possible measurement error. These errors are calculable from the measured data and the properties of the instrument, and are beyond the scope of this document (see [93]). The advantage of this equation is that the figure of merit reduces the influence of measurements that were made that are prone to error; not all combinations of Ψ and Δ are susceptible to error in the same way. The disadvantage is the fact that it requires an intimate knowledge of the equipment and the method through which the instrument extracts data in order to be calculated.

2.2.5 Measurement techniques for simple samples.

Ellipsometry for simple samples is fairly straightforward. The only measurements needed to obtain the characteristics of the sample are a single Ψ and Δ measurement. These measurements are typically made as a function of wavelength to either allow for the modeling of the permittivities or to reduce noise in measuring other sample properties. This section gives practical advice on making measurements and modeling samples.

Measurement angle.

The single piece of information that seems to be most often repeated is that the ideal angle for measurements is Brewster's angle [104]. Brewster's angle is the angle at which one of the incident polarization states is not reflected for a simple sample. Fresnel's equations give the reflection coefficient of p polarized light as

$$r_p = \frac{n_2 \cos\theta_1 - n_1 \cos\theta_2}{n_2 \cos\theta_1 + n_1 \cos\theta_2} \tag{58}$$

where n_1 and n_2 are the indicies of the two materials, and θ_1 and θ_2 are the angle of incidence and reflection in their respective materials. (Note that the s polarization state is ignored, as it does not go to zero.) 0 reflection occurs when the numerator goes to zero. Using Equation (33),

$$n_1 \sin\theta_1 = n_2 \sin\theta_2. \tag{59}$$

The numerator of Equation (58) goes to zero when

$$n_2 \cos\theta_1 = n_1 \sqrt{1 - \left(\frac{n_1}{n_2} \sin\theta_1\right)^2} \tag{60}$$

which can be rewritten as

$$n1^2 n_2^2 - n_2^4 \cos^2\theta_1 + n_1^4 \sin^2\theta_1. \tag{61}$$

Using the identities

$$\sin\theta = \frac{\tan\theta}{\left[1+\tan^2\theta\right]^{1/2}} \tag{62}$$

$$\cos\theta = \frac{1}{\left[1+\tan^2\theta\right]^{1/2}}, \tag{63}$$

this can be rewritten as

$$n_1^2 n_2^2 = \frac{n_2^4 + n_1^4 \tan^2\theta_1}{1+\tan^2\theta_1}. \tag{64}$$

Reorganizing the terms,

$$n_2^2\left(n_1^2 - n_2^2\right) = n_1^2\left(n_1^2 - n_2^2\right)\tan^2\theta_1 \tag{65}$$

which simplifies to Brewster's Law:

$$\theta_1 = \arctan\left(\frac{n_2}{n_1}\right). \tag{66}$$

Now, when an ellipsometric measurement is made at Brewster's angle, one of the polarization states goes to zero; the other does not. If one of the polarization states is perfectly zero, Ψ goes to zero and Δ becomes undefined. By the fundamental equation of ellipsometry, $\rho = 0$. This can be substituted into (28):

$$\begin{aligned} n &= \sin\theta \left[1 + \left(\frac{0-1}{0+1}\right)^2 \tan^2\theta\right]^{1/2} \\ &= \sin\theta \left[1 + \tan^2\theta\right]^{1/2} \\ &= \sin\theta \sec\theta = \tan\theta \end{aligned} \tag{67}$$

Brewster's law gives $\tan\theta = n/1$ when the incident medium is air. At this angle, the angle provides the information necessary to extract the index of the material.

In more complex structures, there is not a single index that determines the ellipsometric angles. However, the material will demonstrate an effective index. This leads to the so-called "pseduo-Brewster's angle", which is the angle at which ρ is closest to zero. These angles tend to be most resiliant against measurement uncertainty, and make for overall better determination of the optical properties of the sample.

Permittivity modeling.

It can sometimes be advantageous to initially fit permittivity data over a subset of the measured data rather than the entire sample set. Some oscillators, especially Lorentz oscillators, will only significantly affect a portion of the wavelength range. Take, for example, the permittivity shown in Figure 12. This permittivity is similar to a metal measured by one of my colleagues, as far as feature number and proportions.

The permittivity has several features to it. The most obvious is the Lorentz oscillator in the middle. The center frequency ω_0 is around 12 microns, which is the peak of the imaginary portion of the permittivity. If this were the only oscillator present, the portion sloping downwards towards the higher wavelengths would not be present. If the Lorentz oscillator was the only oscillator present, the permittivity at longer wavelengths would be a constant. Since it is not, this would imply that there

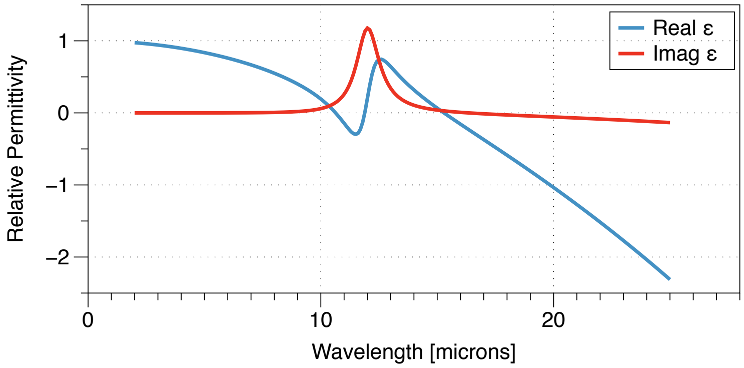

Figure 12. Real and imaginary permittivity based on Nickel.

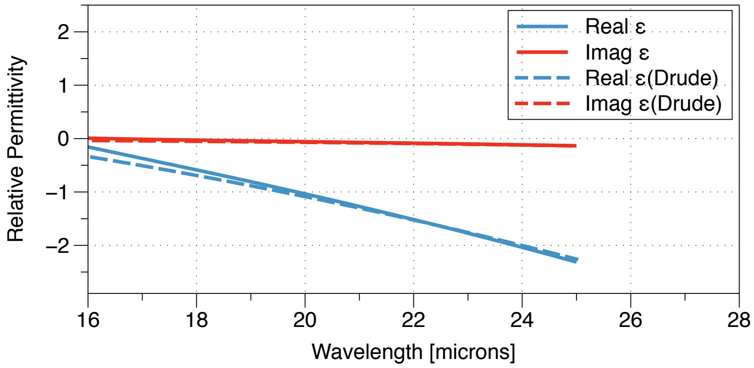

Figure 13. Real and imaginary permittivity based on Nickel, fit with only a Drude oscillator. Notice the drude oscillator better models the permittivity further away from the lorentz oscillator feature, centered at 12 microns.

is most likely a Drude oscillator present as well.

It can be difficult to fit both oscillators at the same time. The Lorentz oscillator is likely spectrally narrow (which can be seen in how quickly the imaginary portion of the oscillator falls away. It makes sense to then try to fit the Drude oscillator away from the range affected by the Lorentz oscillator. Figure 13 shows the actual material permittivity and the permittivity due sole to the Drude oscillator.

The fit shown above gives an amplitude value within about 5% of the actual value, and correctly calculates the broadening parameter Γ. With this oscillator fit, now it is much easier to fit the Lorentz part of the curve. The value of ω_0 can easily be assumed to be 12 microns, which makes fitting the rest of the parameters fairly straightforward. Once the approximate values are entered, a computer optimization technique can easily determine the remaining parameters.

2.3 Advanced Ellipsometry

Most samples are simple. They are homogenous over the examined area, they are isotropic, and they can be nicely defined and treated using the theories outlined above. Many samples are not so simple. A sample made using a deposition might not have the same optical properties as the bulk material [59]. Most metamaterials are not homogenous; indeed, their unique properties are often due to this characteristic [105]. Even simple materials, such as crystals, can have drastically anisotropic characteristics, which give them a huge number of uses within optics [68].

How can we measure and characterize such samples? Ellipsometry can be extended to address some of these concerns, and others can be safely accounted for or completely ignored in the analysis.

All three characteristics of complicated samples can be seen in the nanorods, which are the principle focus of this research. The nanorods are randomly distributed over the sample. This effect can be ignored by simply averaging the measurements over a huge number of nanorods in simulation, and over millions of nanorods in the measurements. The imperfections in the permittivities of the deposition material can be addressed by allowing the deposition permittivity to be one of the fitting parameters. The most difficult attributes to measure is the anisotropy, which will be discussed in this section.

2.3.1 Physics of Generalized Ellipsometry.

One of the assumptions that was made in the previous section was the assumption that there is no cross-polarization present anywhere in the sample. S-pol light comes in, S-pol light comes out; no P-pol light is generated through the interaction. This is not the case in a great number of materials. Take, for instance, a quarter-wave plate. These plates are designed to take linearly polarized light, and create circularly polarized light upon transmission. A material like this cannot be properly examined under the assumptions of the previous section. However, expanding the physics of ellipsometry can be used to extract the same information without the use of this simplifying assumption.

Anisotropic samples.

Anisotropy is the property of being directionally dependent [3]. In electromagnetics, this implies that the properties of the material change as a function of the direction of the fields. This makes everything much more difficult to model, from an electromagnetic standpoint. The direction of the E field will have a drastic impact on the material's effects. This property can be leveraged, and is, to create a huge number of optics with unique properties. One of these, for example, is the quarter wave plate. This optic uses differences in the index, as a function of the direction of the fields, to create circularly polarized light from linearly polarized light.

Anisotropy is caused by having a permittivity that is directionally dependent. This has the effect of changing the polarization such that it is no longer parallel to the E field [41]. This effect can be caused by a number of different phenomena. For example, this effect can be caused by the properties of a crystal lattice. Some crystals lattices are hexagonal in one plane, and rectangular in the other. The hexagonal plane allows for very little electron movement, which causes a lower permittivity. The rectangular dimension allows for much more movement, which creates a very different permittivity [56].

This is especially apparent in the nanorod samples. It is very easy for electrons to move up and down the nanorods. Coupling between nanorods is possible, but more difficult than the up and down movement. In addition, the tiltedness of the nanorods will make it more difficult to couple between nanorods in some directions relative to others. These effects imply that the nanorods will be highly anisotropic.

Jones matrix calculus and Generalized Ellipsometry ratios.

In simple, isotropic samples, there is no way for one polarization state to excite another. This dramatically simplifies the mathematics involved in the electromagnetics, as any cross-coupling effects can be considered to be zero. This is not the case for anisotropic samples [19]. Quarterwave plates, for examples, can take a single polarization as incident and transmit both polarization states. With this, it makes sense to expand the reflection and transmission coefficients to address this new feature. The Jones matrix relates input and output polarizations [33].

For a sample with incident light $E^i_{s,p}$, the reflected (E^r) and transmitted (E^t) light can be related to the incident light with the following equations:

$$\begin{bmatrix} E^r_p \\ E^r_s \end{bmatrix} = \begin{bmatrix} r_{pp} & r_{sp} \\ r_{ps} & r_{ss} \end{bmatrix} \begin{bmatrix} E^i_p \\ E^i_s \end{bmatrix} \tag{68}$$

$$\begin{bmatrix} E^t_p \\ E^t_s \end{bmatrix} = \begin{bmatrix} t_{pp} & t_{sp} \\ t_{ps} & t_{ss} \end{bmatrix} \begin{bmatrix} E^i_p \\ E^i_s \end{bmatrix}. \tag{69}$$

All of the electromagnetic fields in these equations are complex, and the matrix elements are complex as well. This allows for the phase of the fields to change through their interaction with the sample. The values in these matrices are straightforward. For example, r_{ps} element represents the complex ratio of incident P-pol light to the reflected S-pol light.

The ellipsometric ratios are normalized values taken from the Jones matrix. There are six ratios that are used in generalized ellipsometry, which are as follows [10].

$$\rho_{pp} \equiv \frac{r_{pp}}{r_{ss}} \tag{70}$$

$$\rho_{ps} \equiv \frac{r_{ps}}{r_{ss}} \tag{71}$$

$$\rho_{sp} \equiv \frac{r_{sp}}{r_{ss}} \tag{72}$$

$$\tau_{pp} \equiv \frac{t_{pp}}{t_{ss}} \tag{73}$$

$$\tau_{ps} \equiv \frac{t_{ps}}{t_{ss}} \tag{74}$$

$$\tau_{sp} \equiv \frac{t_{sp}}{t_{ss}}. \tag{75}$$

The ratios are similar to the ratio ρ discussed previously. ρ, τ_{pp} is the same as ρ in normal ellipsometry. ρ, τ_{ps} is the ratio of P-pol light generated by the S-pol state to that generated by the S-pol state. The ρ, τ_{sp} ratio is the P-pol light generated by the S-pol state over the S-pol light that is generated by the same state. It is very common to see these ratios described using Ψ and Δ angles. These angles are generated in the same way, although they lack the physical intuition of the Ψ_{pp} and Δ_{pp} angles.

These angle are used because measuring the phase of a field within the visible or infrared regime is incredibly difficult, if not impossible in most cases. Within these regimes, the electric field cannot be directly measured; instead, the power of the wave is observed. The power of a field does not convey any information about the absolute phase, so this information cannot be observed. This is not the case in low frequency regimes, such as radio and microwaves, where the lower frequency allows for the detection of the phase of a field. Because the absolute phase cannot be determined, measurements within the visible and infrared regime must instead rely on the relative phase of the fields. The relative phases can be easily determined using techniques such as interferometry. Hence, relative fields are exclusively used within ellipsometry.

The Jones matrix can be rewritten to utilize these ratios rather than the individual values, which is useful to compare theory and measurements. The scaled version of the Jones matrix is then

$$\begin{bmatrix} E_p^r \\ E_s^r \end{bmatrix} = r_{ss} \begin{bmatrix} \rho_{pp} & \rho_{sp} \\ \rho_{ps} & 1 \end{bmatrix} \begin{bmatrix} E_p^i \\ E_s^i \end{bmatrix} \tag{76}$$

$$\begin{bmatrix} E_p^t \\ E_s^t \end{bmatrix} = t_{ss} \begin{bmatrix} \tau_{pp} & \tau_{sp} \\ \tau_{ps} & 1 \end{bmatrix} \begin{bmatrix} E_p^i \\ E_s^i \end{bmatrix} . \tag{77}$$

This can sometimes simplify equations used for extracting these parameters from measurements.

2.3.2 Generalized Ellipsometry measurements.

Making Generalized Ellipsometry measurements is substantially more difficult than making standard ellipsometry measurements. This section will give some insight into the operation of the ellipsometer and give some practical advice for running these experiments. There are a few works that give practical advice on making these measurements, but much is left to the experimenter to learn by themselves. This is mainly due to the difficulty in making these measurements; it takes years for experimenters to properly learn how to measure and model these materials efficiently.

Experimental setup.

There are several different ellipsometer configurations which can be used to extract the Generalized Ellipsometry measurements. The simplest of these is the Rotating Analyzer Ellipsometry, commonly referred to as Rotating Analyzer Ellipsometer (RAE). A functional diagram of the ellipsometer is shown in Figure 14. This analyzer is physically simpler than the null ellipsometer examined in the previous section. The

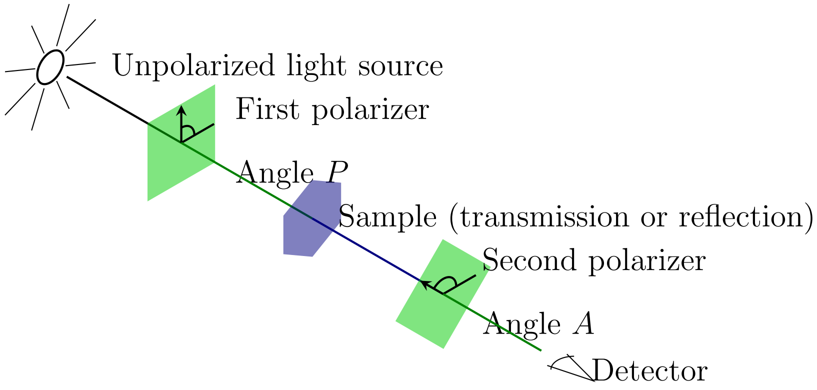

Figure 14. Functional diagram of a Rotating Analyzer Ellipsometer. The analyzer is rotated through a full rotation for several different polarizer angles.

trade-off is that extracting the elements of the Jones matrix is substantially harder.

Fujiwara gives the electric field observed at the detector for an RAE instrument [30] as

$$E_{\mathrm{RAE}} \propto (\rho_{pp} + \rho_{ps} \tan\psi_P)\cos\psi_A + (\rho_{sp} + \tan P)\sin\psi_A \tag{78}$$

where the ψ_A is the angle of the analyzer polarizer and ψ_P is the angle of the first polarizer. The detector can only detect the overall intensity of the light, which is

$$I_{\mathrm{RAE}} = |E_{\mathrm{RAE}}|^2 \propto |\Xi|^2\cos^2\psi_A + |\Theta|^2\sin^2\psi_A + 2\mathrm{Re}\{\Xi\Theta\}\cos\psi_A\sin\psi_A \tag{79}$$

where

$$\Xi = \rho_{pp} + \rho_{ps}\tan\psi_P \tag{80}$$

$$\Theta = \rho_{sp} + \tan\psi_P. \tag{81}$$

This can be easily rewritten as

$$I_{\mathrm{RAE}} \propto |\Xi|^2 + |\Theta|^2 + \left(|\Xi|^2 - |\Theta|^2\right)\cos 2\psi_A + 2\mathrm{Re}\{\Xi\Theta\}\sin 2\psi_A \tag{82}$$

using a few trigonometric identities. This is normalized into the more standard form

$$I_{\text{RAE}} \propto 1 + \alpha \cos 2\psi_A + \beta \sin 2\psi_A \tag{83}$$

where

$$\alpha = \frac{|\rho_{pp} + \rho_{ps} \tan \psi_P|^2 - |\rho_{sp} + \tan \psi_P|^2}{|\rho_{pp} + \rho_{ps} \tan \psi_P|^2 + |\rho_{sp} + \tan \psi_P|^2} \tag{84}$$

$$\beta = \frac{\mathrm{Re}\left\{(\rho_{pp} + \rho_{ps} \tan \psi_P)\,(\rho_{sp} + \tan \psi_P)\right\}}{|\rho_{pp} + \rho_{ps} \tan \psi_P|^2 + |\rho_{sp} + \tan \psi_P|^2}. \tag{85}$$

The above equation is the same in the case of making a transmission measurement, except that the ρ terms are replaced by τ terms.

Over the course of a measurement, the analyzer (ψ_A) is rotated over some range. Once the data is taken, the coefficients α and β can be extracted for some value of ψ_P. This gives two values for calculating six unknowns; each value of ρ has a real and imaginary component that must be calculated. Because of this, the experiment needs to be repeated at least two more times at different values of ψ_P, in order to have enough data to extract all of the necessary values. Typically, data is collected at more than three values of ψ_P to increase the confidence in the extracted values.

Notes on making measurements.

Because of the anisotropic nature of the samples examined, it is no longer possible to get all of the information needed from a single measurement. Multiple measurements are needed at different angles of incidence and sample orientations. All of these measurements need to be fit to the model simultaneously in order to extract the effective properties. Many commercial packages offer features which do this for the user more-or-less automatically [102].

2.3.3 Modeling under Generalized Ellipsometry.

The modeling of materials with anisotropic properties becomes exponentially more difficult than isotropic materials. The direction and orientation of the E field now play a part in the transmission of energy through a layer. Under most circumstances, a completely different approach is needed in order to calculate the relevant ellipsometric values.

There are some approaches which do not require the following formalisms to analyze. These often have stringent requirements which make them unusable for the nanorods examined in this research. For instance, Fujiwara gives a derivation of ellipsometric values taken from an anisotropic material which has optical axes aligned with the plane of the measurement [30]. This may be a good approach for many metamaterials, such as split ring resonators [34], but fails for ours; the tilt of the nanorods implies that the optical axes will not be aligned with the laboratory frame of reference.

Four-by-four Matrix Formalism.

The Four-by-four Matrix Formalism begins with the assumption of linearity: there must be some linear relationship between the fields incident, reflected, and transmitted through some material [79]. This is one of the basic assumptions for any kind of work in optics, and holds true for almost all materials. This formalism expresses this relationship using the T matrix:

$$\begin{bmatrix} E_s^i \\ E_s^r \\ E_p^i \\ E_p^r \end{bmatrix} = \begin{bmatrix} T \end{bmatrix} \begin{bmatrix} E_s^t \\ 0 \\ E_p^t \\ 0 \end{bmatrix} . \tag{86}$$

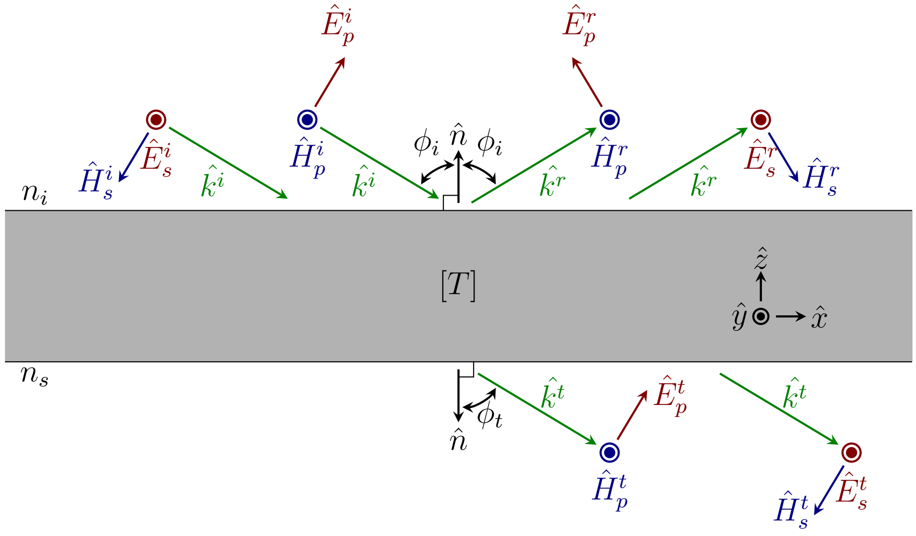

Figure 15. Diagram of a problem involving a T matrix. The T matrix converts from incident and reflected fields to the transmitted fields. From this, the generalized ellipsometry angles can be extracted. E refers to teh E fields, H refers to the magnetic fields, and $\hat{k}$ demonstrates the direction of propagation. i indicates an incident field, r indicates a reflected field, and t indicates a transmitted field.

This is shown in Figure 15.

The T matrix, commonly known as the transfer matrix, is composed of three parts. The first is a projection matrix (L_i) which casts the incident, reflected, and transmitted light onto the plane of the material. A similar matrix (L_t) is needed for the bottom of the material, taking the E fields at the interface and converting them into the transmitted rays. The final part of the matrix is the matrix (T_p) which describes the relationship between the E fields on the top face with that of the bottom. This matrix is the most complex of the three, and will be discussed in depth. In equation form, this is expressed as

$$T = L_i^{-1} T_p L_t \tag{87}$$

The front projection matrix L_i takes the incident and reflected light, and converts

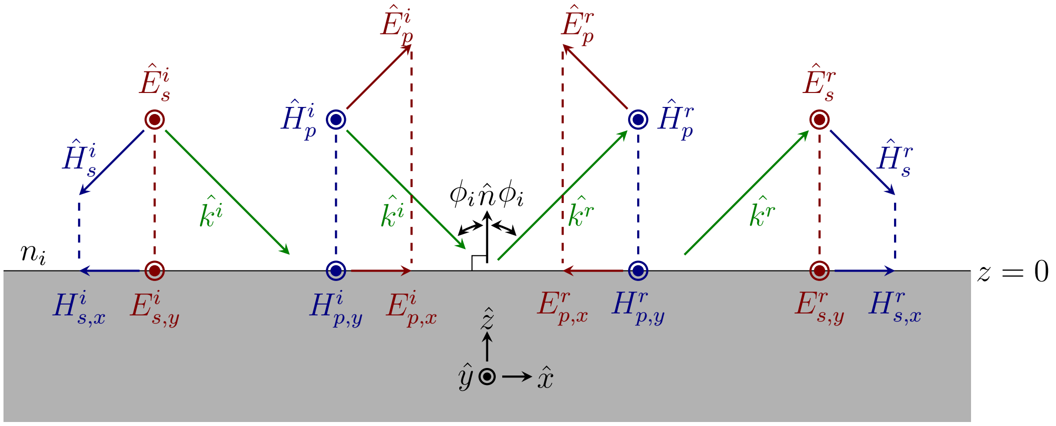

Figure 16. The matrix L_i projects from the incident and reflected E fields onto the plane of the material in terms of both E and H.

it into the E and H fields on the surface:

$$\begin{aligned}\begin{bmatrix} E_x(0) & E_y(0) & H_x(0) & H_y(0) \end{bmatrix}^T &= L_i \begin{bmatrix} E_s^i & E_s^r & E_p^i & E_p^r \end{bmatrix}^T \\ &= \begin{bmatrix} 0 & 0 & \cos\theta_i & -\cos\theta_i \\ 1 & 1 & 0 & 0 \\ -n_i\cos\theta_i & n_i\cos\theta_i & 0 & 0 \\ n_i & n_i & 0 & 0 \end{bmatrix} \begin{bmatrix} E_s^i \\ E_s^r \\ E_p^i \\ E_p^r \end{bmatrix}. \end{aligned} \tag{88}$$

n_i is the index of the incident medium and θ_i is the angle of incidence. Here, Centimeter-Gram-Second (CGS) units are used to simplify the equations. This will be continued throughout the rest of this document. A diagram illustrating this projection is shown in Figure 16.

The rear projection matrix L_t is formed in the same way (see Figure 17). Traditionally, this matrix simply performs the same projection of the transmitted wave onto the rear face. This is appropriate for ellipsometric experiments. The matrix

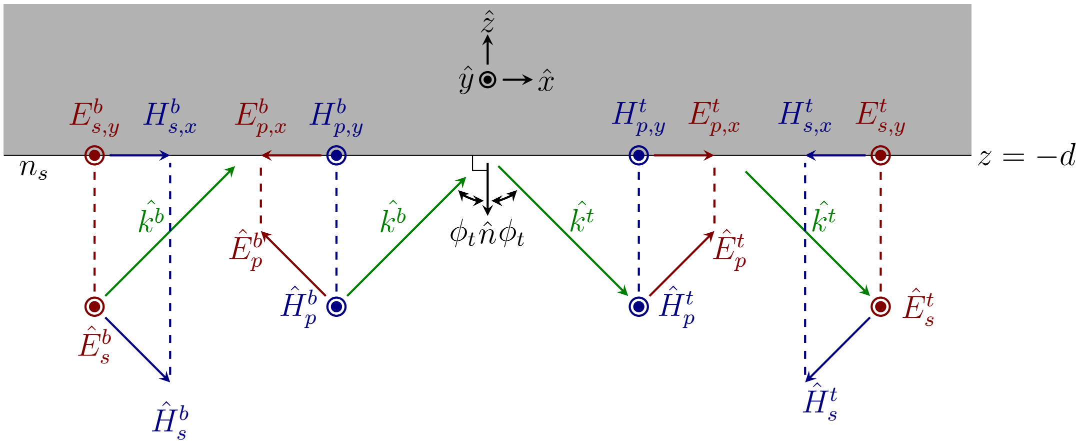

Figure 17. L_t projects from the back-traveling and transmitted E fields onto the rear plane of the material in terms of E and H. For the partial transfer matrix, E_b is set to zero.

which performs this operation is:

$$\begin{aligned}\begin{bmatrix} E_x(-d) & E_y(-d) & H_x(-d) & H_y(-d) \end{bmatrix}^T &= L_t \begin{bmatrix} E^t_s & 0 & E^t_p & 0 \end{bmatrix}^T \\ &= \begin{bmatrix} 0 & 0 & \cos\theta_s & 0 \\ 1 & 0 & 0 & 0 \\ -n_s\cos\theta_s & 0 & 0 & 0 \\ 0 & 0 & n_s & 0 \end{bmatrix} \begin{bmatrix} E^t_s \\ 0 \\ E^t_p \\ 0 \end{bmatrix}. \end{aligned} \tag{89}$$

Here, n_s is the index of the substrate, and θ_s is the angle of the transmitted wave. A diagram illustrating this projection is shown in Figure 17.

This approach deliberately ignores the possibility of a back-traveling wave, much on purpose. The back-traveling wave is not present in any ellipsometry experiment, and is completely unnecessary for calculating ellipsometric quantities. However, there are cases where utilizing the back-traveling wave may be advantageous. Allowing for a back-traveling wave will allow for more information about the medium to be extracted during a simulation. Because of this, it makes sense to derive a full transfer matrix, which allows for the back-traveling wave as well:

$$\begin{bmatrix} E_x(-d) \\ E_y(-d) \\ H_x(-d) \\ H_y(-d) \end{bmatrix} = L_t \begin{bmatrix} E_s^t \\ E_s^b \\ E_p^t \\ E_p^b \end{bmatrix} = \begin{bmatrix} 0 & 0 & \cos\theta_s & -\cos\theta_s \\ 1 & 1 & 0 & 0 \\ -n_s\cos\theta_s & n_s\cos\theta_s & 0 & 0 \\ 0 & 0 & n_s & n_s \end{bmatrix} \begin{bmatrix} E_s^t \\ E_s^b \\ E_p^t \\ E_p^b \end{bmatrix}. \tag{90}$$

Here, E^b refers to the back-traveling wave.

The traditional rear projection matrix (which will be denoted as the partial rear projection matrix where applicable) is useful in it is the simplest matrix that can be used for extracting the relevant information. The full rear projection matrix has several other properties that make it more desirable in problems involving simulation.

The first property is that this matrix is fully invertible. The partial transfer matrix has two columns of zeros, which means that it destroys information whenever it is used. The full transfer matrix does not; although that extra information is useless much of the time in a classical ellipsometry environment.

The second is that it allows the sample to be interrogated from the back of the sample, which allows for more information about the sample to be extracted. Again, in ellipsometry, this is not done, but this is something easily accomplished in simulation. A back-traveling wave can be easily created in order to extract more information about the system. This will be explored in more depth in Chapter IV.

T_p **matrix.** The final matrix needed to calculate T is denoted T_p, and relates the fields on the top ($z = 0$) with those on the bottom ($z = -d$), or

$$\begin{bmatrix} E_x(0) & E_y(0) & H_x(0) & H_y(0) \end{bmatrix}^T = T_p \begin{bmatrix} E_x(-d) & E_y(-d) & H_x(-d) & H_y(-d) \end{bmatrix}^T . \tag{91}$$

The electromagetics of the problem can be examined to determine the value of this matrix.

The differential equation

$$\frac{\partial}{\partial z} \begin{bmatrix} E_x(z) & E_y(z) & H_x(z) & H_y(z) \end{bmatrix}^T = i\frac{c}{\omega}\Delta_B \begin{bmatrix} E_x(z) & E_y(z) & H_x(z) & H_y(z) \end{bmatrix}^T \tag{92}$$

is known as Berreman's equation [15], and describes how light propagates through an anisotropic layer. Here, ω is the frequency, c is the speed of light, and Berreman's matrix Δ_B is defined as

$$\Delta_B = \begin{bmatrix} -K_{xx}\frac{\epsilon_{zx}}{\epsilon_{zz}} & -K_{xx}\frac{\epsilon_{zy}}{\epsilon_{zz}} & 0 & 1 - \frac{K_{xx}^2}{\epsilon_{zz}} \\ 0 & 0 & -1 & 0 \\ \epsilon_{yz}\frac{\epsilon_{zx}}{\epsilon_{zz}} - \epsilon_{yx} & K_{xx}^2 - \epsilon_{yy} + \epsilon_{yz}\frac{\epsilon_{zy}}{\epsilon_{zz}} & 0 & K_{xx}\frac{\epsilon_{yz}}{\epsilon_{zz}} \\ \epsilon_{xx} - \epsilon_{xz}\frac{\epsilon_{zx}}{\epsilon_{zz}} & \epsilon_{xy} - \epsilon_{xz}\frac{\epsilon_{zy}}{\epsilon_{zz}} & 0 & -K_{xx}\frac{\epsilon_{xz}}{\epsilon_{zz}} \end{bmatrix} . \tag{93}$$

K_{xx} is defined as $n_i \sin\theta_i$, and the ϵ variables are taken from the effective permittivity tensor

$$\boldsymbol{\epsilon} = \begin{bmatrix} \epsilon_{xx} & \epsilon_{xy} & \epsilon_{xz} \\ \epsilon_{yx} & \epsilon_{yy} & \epsilon_{yz} \\ \epsilon_{zx} & \epsilon_{zy} & \epsilon_{zz} \end{bmatrix} . \tag{94}$$

This means, given a direction of propagation in the incident media, K_{xx}, and knowing the permittivity tensor, $\boldsymbol{\epsilon}$, the change in the E and H fields as a function of z can be known. With this, the relationship between the fields at the front of the material and the rear of the material can be known. Solving Berreman's equation for $z = 0$ in terms of $z = -d$ (see Figure 15) yields

$$\begin{bmatrix} E_x(0) \\ E_y(0) \\ H_x(0) \\ H_y(0) \end{bmatrix} = \exp\left(-i\frac{2\pi}{\lambda_0}\Delta_B d\right) \begin{bmatrix} E_x(-d) \\ E_y(-d) \\ H_x(-d) \\ H_y(-d) \end{bmatrix}. \tag{95}$$

This implies

$$T_p = \exp\left(-i\frac{2\pi}{\lambda_0}\Delta_B d\right). \tag{96}$$

Note that the exponential in the equation is actually a matrix exponential, since Δ_B is a matrix. Matrix exponentials are more difficult to calculate than scalar exponentials, but can be easily calculated in most numerical packages (see [61]).

If there are multiple layers to a material, the matrix T_p will need to be constructed from several different matrices; one for each layer. For J layers, the matrix T_p will be

$$T_p = \prod_{j=1}^{J} T_j \tag{97}$$

where T_j is the T_p matrix calculated for that individual layer.

ϵ tensor. The only thing left to properly define is the tensor $\boldsymbol{\epsilon}$, specifically the elements of this tensor. This three-by-three tensor (or matrix or dyadic, depending on the referenced literature [56]), has the form given in (94). It is difficult to understand the physical implications from this equation alone, which is why it will be examined more thoroughly in relation to the D field.

The electric flux density D is a measure of charge per area [41]. It has units of amp-seconds per area, or equivalently Farad-volts per area. D is related to the E field by ϵ. Since E has units of volts per meter, ϵ must have units of Farads per meter, which is a measure of capacitance. Therefore, ϵ is a measure of how much energy can be stored in space as a function of distance.

In vector form, the relationship between D and E is described by

$$\begin{bmatrix} D_x \\ D_y \\ D_z \end{bmatrix} = \boldsymbol{\epsilon} \begin{bmatrix} E_x \\ E_y \\ E_z \end{bmatrix}. \tag{98}$$

In free space, ϵ has no directional dependence; energy is not stored more easily in any direction than any other. ϵ is therefore a constant (ϵ_0) in free space. ϵ is a constant, although not typically ϵ_0, in most materials.

This is not the case for all materials. Anisotropic materials exhibit the property that energy is more easily stored in some directions than others. Crystals are a naturally occurring material that exhibit this property. Their crystalline structure allows for energy to be stored easily in some directions, but not others. In these situations, the $\boldsymbol{\epsilon}$ tensor is needed to describe the relationship between the E field and the D field. Written more explicitly using Equation (94),

$$\begin{aligned} D_x\hat{x} &= \epsilon_{xx}E\hat{x} + \epsilon_{xy}E_y\hat{y} + \epsilon_{xz}E_z\hat{z} \\ D_y\hat{y} &= \epsilon_{yx}E\hat{x} + \epsilon_{yy}E_y\hat{y} + \epsilon_{yz}E_z\hat{z} \\ D_z\hat{z} &= \epsilon_{zx}E\hat{x} + \epsilon_{zy}E_y\hat{y} + \epsilon_{zz}E_z\hat{z}. \end{aligned} \tag{99}$$

Now, the D field and the E field are not necessarily aligned. An E field oriented in the $\hat{x}$ direction might contribute to a D field in the $\hat{y}$ direction, if it is easier for energy to be stored in that direction.

This is the most general form of the $\boldsymbol{\epsilon}$ tensor. There are some assumptions that can be made to simplify the matrix. For example, what would happen if the E field was aligned with one of these directions that best stores energy? In the case of the crystal, what if the E field was aligned with the crystalline direction? If these directions can be expressed such that they are orthogonal to each other [68], then (99) can be rewritten as

$$\begin{aligned} D_\alpha &= \epsilon_\alpha E_\alpha \hat{\alpha} \\ D_\beta &= \epsilon_\beta E_\beta \hat{\beta} \\ D_\gamma &= \epsilon_\gamma E_\gamma \hat{\gamma}. \end{aligned} \tag{100}$$

or

$$\begin{bmatrix} D_\alpha \\ D_\beta \\ D_\gamma \end{bmatrix} = \begin{bmatrix} \epsilon_\alpha & 0 & 0 \\ 0 & \epsilon_\beta & 0 \\ 0 & 0 & \epsilon_\gamma \end{bmatrix} \begin{bmatrix} E_\alpha \\ E_\beta \\ E_\gamma \end{bmatrix} \tag{101}$$

where $\hat{\alpha}$, $\hat{\beta}$, and $\hat{\gamma}$ are unit vectors along the crystalline axes. This diagonalization can be done using a rotation matrix [30]. Assuming that R is a rotation matrix which converts from the (x, y, z) coordinate system to the (α, β, γ) coordinate system,

$$\begin{bmatrix} D_x \\ D_y \\ D_z \end{bmatrix} = R \begin{bmatrix} \epsilon_\alpha & 0 & 0 \\ 0 & \epsilon_\beta & 0 \\ 0 & 0 & \epsilon_\gamma \end{bmatrix} R^{-1} \begin{bmatrix} E_x \\ E_y \\ E_z \end{bmatrix}. \tag{102}$$

In some cases, the crystal axes are not perpendicular to one another. $\boldsymbol{\epsilon}$ can still be diagonalized in this case, although it requires a triclinic (crystalline) axes to orthonormal axes transformation [77]. This can be written in terms of a rotation matrix (which needs at least three angles) and a triclinic projection matrix, which is covered in more detail in Chapter VI.

Ratio and angle extraction.

The T matrix completely describes the relationship between the light exiting a material and the light incident on and reflected from the material [93]. From this, all of ellipsometric values can be directly extracted. This relationship is

$$\begin{bmatrix} E_s^i \\ E_s^r \\ E_p^i \\ E_p^r \end{bmatrix} = \begin{bmatrix} T_{11} & T_{12} & T_{13} & T_{14} \\ T_{21} & T_{22} & T_{23} & T_{24} \\ T_{31} & T_{32} & T_{33} & T_{34} \\ T_{41} & T_{42} & T_{43} & T_{44} \end{bmatrix} \begin{bmatrix} E_s^t \\ 0 \\ E_p^t \\ 0 \end{bmatrix}, \tag{103}$$

which is (86) stated with the elements of T enumerated.

The ellipsometric data being extracted are the ratios between the Jones matrix elements, which were given in (70) through (75). These ratios can be expressed, using the Jones matrix ((68) and (69)) in terms of the incident, reflected, and transmitted E fields. For instance,

$$E_p^r = r_{pp} E_p^i + r_{ps} E_s^i, \tag{104}$$

which is taken directly from the Jones matrix equation (68). If E_s^i is equal to zero, the element r_{pp} is

$$r_{pp} = \left. \frac{E_p^r}{E_p^i} \right|_{E_s^i=0}. \tag{105}$$

Similarly,

$$r_{ss} = \left. \frac{E_s^r}{E_s^i} \right|_{E_p^i=0}. \tag{106}$$

The ellipsometric ratio R_{pp} is then expressible as

$$R_{pp} = \frac{E_p^r / E_p^i \big| \, E_s^i = 0}{E_s^r / E_s^i \big| \, E_p^i = 0}. \tag{107}$$

All four of the quantities in this equation can be described using terms of the T

matrix.

$$E_s^i = T_{11}E_s^t + T_{13}E_p^t \tag{108}$$

$$E_s^r = T_{21}E_s^t + T_{23}E_p^t \tag{109}$$

$$E_p^i = T_{31}E_s^t + T_{33}E_p^t \tag{110}$$

$$E_p^r = T_{41}E_s^t + T_{43}E_p^t. \tag{111}$$

r_{pp} is then

$$\begin{aligned} r_{pp} &= \left.\frac{T_{41}E_s^t + T_{43}E_p^t}{T_{31}E_s^t + T_{33}E_p^t}\right| T_{11}E_s^t + T_{13}E_p^t = 0 \\ &= \left.\frac{T_{41}E_s^t + T_{43}E_p^t}{T_{31}E_s^t + T_{33}E_p^t}\right| E_p^t = -\frac{T_{11}}{T_{13}}E_s^t \\ &= \frac{T_{41} - T_{43}(T_{11}/T_{13})}{T_{31} - T_{33}(T_{11}/T_{13})} \\ &= \frac{T_{41}T_{13} - T_{43}T_{11}}{T_{31}T_{13} - T_{33}T_{11}}. \end{aligned} \tag{112}$$

Note that if T_{13} is equal to zero, the above derivation can be redone defining $E_s^t = -T_{13}/T_{11}$. Similarly,

$$r_{ss} = \frac{T_{31}T_{23} - T_{33}T_{21}}{T_{31}T_{13} - T_{33}T_{11}}. \tag{113}$$

Now, R_{pp} can be written exclusively in terms of the elements of T.

$$\begin{aligned} R_{pp} &= \frac{E_p^r/E_p^i\big|\, E_s^i = 0}{E_s^r/E_s^i\big|\, E_p^i = 0}. \\ &= \frac{(T_{41}T_{13} - T_{43}T_{11})\,/\,(T_{31}T_{13} - T_{33}T_{11})}{(T_{31}T_{23} - T_{33}T_{21})\,/\,(T_{31}T_{13} - T_{33}T_{11})} \\ &= \frac{T_{41}T_{13} - T_{43}T_{11}}{T_{31}T_{23} - T_{33}T_{21}}. \end{aligned} \tag{114}$$

The other ratios can be found in a similar manner, and can be shown to be

$$R_{ps} = \frac{T_{11}T_{12} - T_{21}T_{13}}{T_{11}T_{43} - T_{41}T_{13}} \tag{115}$$

$$R_{sp} = \frac{T_{41}T_{33} - T_{43}T_{31}}{T_{21}T_{33} - T_{23}T_{31}} \tag{116}$$

$$T_{pp} = -\frac{T_{11}}{T_{33}} \tag{117}$$

$$T_{ps} = -\frac{T_{13}}{T_{11}} \tag{118}$$

$$T_{sp} = -\frac{T_{31}}{T_{33}}. \tag{119}$$

Model parameters.

Modeling something as a single layer with anisotropic properties is known as the Homogenous Biaxial Layer Approximation (HBLA). While the nanocolumns are not a homogenous layer, their macroscopic properties can be approximated as such [74]. These properties cannot be extracted directly from the ellipsometric measurements. Instead, a model of a homogenous biaxial material must be generated, then compared to the measured data.

This leaves a large number of unknowns which need to be solved simultaneously. Most of these unknowns come from the $\boldsymbol{\epsilon}$ matrix. There are three different permittivities within the matrix, one for each axis. These permittivities will be modeled using (54), which contains ten unknowns each. This gives thirty unknowns for the diagonalized permittivity matrix.

This diagonalized matrix is then modified by a rotational matrix, which converts from the crystalline axes to the laboratory axes. An Euler rotation matrix will be used for this, which includes an additional three unknowns: the angles ϕ_e, θ_e, and ψ_e. The final unknown is the layer thickness d. This gives a total unknown count of 34 in

Table 1. Unknowns in HBLA model. Each optical axis is modeled by two lorentz oscillators and one drude, which accounts for 10 unknowns each.

α axis	β axis	γ axis	Layer
A_{drude}	A_{drude}	A_{drude}	ϕ_e
Γ_{drude}	Γ_{drude}	Γ_{drude}	θ_e
$A_{\text{lor},1}$	$A_{\text{lor},1}$	$A_{\text{lor},1}$	ψ_e
$\Gamma_{\text{lor},1}$	$\Gamma_{\text{lor},1}$	$\Gamma_{\text{lor},1}$	d
$\lambda_{0,\text{lor},1}$	$\lambda_{0,\text{lor},1}$	$\lambda_{0,\text{lor},1}$	
$A_{\text{lor},2,\alpha}$	$A_{\text{lor},2}$	$A_{\text{lor},2}$	
$\Gamma_{\text{lor},2}$	$\Gamma_{\text{lor},2}$	$\Gamma_{\text{lor},2}$	
$\lambda_{0,\text{lor},2}$	$\lambda_{0,\text{lor},2}$	$\lambda_{0,\text{lor},2}$	

order to model this material as a homogenous biaxial layer, which has the $[\epsilon]$ matrix

$$\epsilon = R(\phi_e, \theta_e, \psi_e)^{-1} \begin{bmatrix} \epsilon_\alpha & & \\ & \epsilon_\beta & \\ & & \epsilon_\gamma \end{bmatrix} R(\phi_e, \theta_e, \psi_e) \tag{120}$$

These unknowns are shown in Table 1. Before the advent of personal computers, solving for so many unknowns would have been impossible. With modern numeric packages, optimization routines can be easily setup to numerically solve for all of the unknowns simultaneously. This is precisely what is done by ellipsometric packages such as WVASE32, built by J.A. Woollam and Co.

Other models.

The Bruggeman effective medium approximation which was covered previously relies on the assumption that the particles suspended in the material are spherical. There are many times that this is not the case. One of the most straightforward and

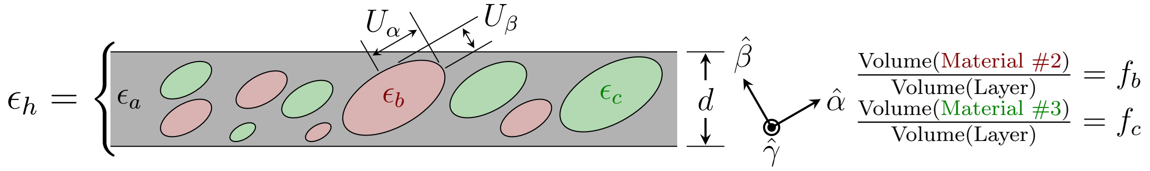

Figure 18. Diagram of a Traditional and Rigorous Anisotropic Bruggeman effective medium. This material exhibits different optical properties depending on the orientation of the E field.

useful extensions of this model are the Traditional Anisotropic Bruggeman (TAB) EMA and the Rigorous Anisotropic Bruggeman (RAB) EMA. Both of these approaches opt for ellipsoidal particles which are defined by the ratio of their axes. TAB-EMA is easier to calculate, while RAB-EMA can be used to provide more accurate solutions to the effective permittivities [57].

Both models use the same underlying assumption of ellipsoidal particles suspended in a material with an effective permittivity. This is shown in Figure 18. The model is very similar to that of Figure 9, but with ellipsoidal particles instead of spherical particles.

TAB-EMA. For the TAB-EMA model [57], the permittivity of each axes is defined in the set of equations

$$0 = \sum_{m=1}^{M} f_m \frac{\epsilon_m - \epsilon_{h,j}}{\epsilon_{h,j} + L_j^D(\epsilon_m - \epsilon_{h,j})} \tag{121}$$

where j is each axis of permittivity, that is $j \in \{\alpha, \beta, \gamma\}$ (this is what gives the three separate equations). f_m is once again the volume fraction of each constituent material, M is the total number of constituent materials, and L_j^D is what is known as the depolarization factor for each axis. For the TAB-EMA model, each depolarization factor is calculated in the same way, using the equation

$$L_j^D = \frac{U_\alpha U_\beta U_\gamma}{2} \int_0^\infty \frac{(s+U_j^2)^{-1} ds}{\sqrt{(s+U_x^2)(s+U_y^2)(s+U_z^2)}}. \tag{122}$$

Here, the factors $U_{\{\alpha,\beta,\gamma\}}$ represent the relative dimension of the ellipsoid along the related axis, and s is a placeholder variable. Some algebra can be used to show that not all three dimensions need to be defined; only the ratios between the three are needed. Typically, U_α/U_γ and U_β/U_γ are defined. This gives a total of M+1 fitting parameters per layer.

Solving Equation (121) can often prove to be difficult due to the number of roots of the equation. The details of arriving at the correct solution are given in Appendix B.

RAB-EMA. The defining equations of the RAB-EMA model are very similar to (121). They are

$$0 = \sum_{n=1}^{N} f_n \frac{\epsilon_n - \epsilon_{h,j}}{1 + D_j^D(\epsilon_n - \epsilon_{h,j})} \tag{123}$$

for each $j \in \{\alpha, \beta, \gamma\}$. D_j^D is a different depolarization factor which is more difficult to calculate.

$$D_\alpha^D = \frac{1}{4\pi} \int_0^{2\pi} \int_0^{\pi} \frac{\sin^3\theta \cos^2\phi}{U_\alpha^2 \rho_R} d\theta \; d\phi \tag{124}$$

$$D_\beta^D = \frac{1}{4\pi} \int_0^{2\pi} \int_0^{\pi} \frac{\sin^3\theta \sin^2\phi}{U_\beta^2 \rho_R} d\theta \; d\phi \tag{125}$$

$$D_\gamma^D = \frac{1}{4\pi} \int_0^{2\pi} \int_0^{\pi} \frac{\sin\theta \cos^2\phi}{U_\gamma^2 \rho_R} d\theta \; d\phi \tag{126}$$

where

$$\rho_R = \frac{\sin^2\theta \cos^2\phi}{U_\alpha^2}\epsilon_{h,\alpha} + \frac{\sin^2\theta \sin^2\phi}{U_\beta^2}\epsilon_{h,\beta} + \frac{\cos\phi}{U_\gamma^2}\epsilon_{h,\gamma}. \tag{127}$$

Note that the inclusion of the effective permittivities within the ρ term (which is itself within the depolarization factors), makes this set of equations significantly more difficult to solve. Calculating the effective permittivities can be done numerically, but is a difficult and tedious process. Furthermore, this forces the depolarization factor to be wavelength dependent. The difficulties in performing these calculations has made utilizing this in experiments prohibitively difficult; although there have been some papers published which uses this effective medium.

Difficulties aside, there are an equal number of unknowns between the TAB-EMA and RAB-EMA approaches to calculate layer permittivities.

2.3.4 Figures of merit.

The FOM used in Generalized Ellipsometry are much like those used in basic ellipsometry, as seen in Equations (55) through (57). The difference is that the additional extracted angles must now be included in the figures of merit. The three figures of merit become [30]

$$\begin{aligned}\sigma_{\mathrm{GE}}^2 = \frac{1}{3M-F-1}\sum_{m=1}^{M} &\big[(\rho_{pp,\mathrm{meas}}(\lambda_m) - \rho_{pp,\mathrm{calc}}(\lambda_m))^2 \\ &+ \big(\rho_{ps,\mathrm{meas}(\lambda_m)} - \rho_{ps,\mathrm{calc}(\lambda_m)}\big)^2 + \big(\rho_{sp,\mathrm{meas}(\lambda_m)} - \rho_{sp,\mathrm{calc}(\lambda_m)}\big)^2\Big] \qquad (128)\end{aligned}$$

$$\begin{aligned}\xi^2_{\mathrm{GE}} =& \frac{1}{6M-F+1}\times \\ &\sum_{m=1}^{M}\left[\left(\frac{\Psi_{pp,\mathrm{meas}}(\lambda_m)-\Psi_{pp,\mathrm{calc}}(\lambda_m)}{\sigma\Psi_{pp}(\lambda_m)}\right)^2+\left(\frac{\Delta_{pp,\mathrm{meas}}(\lambda_m)-\Delta_{pp,\mathrm{calc}}(\lambda_m)}{\sigma\Delta_{pp}(\lambda_m)}\right)^2\right. \\ +&\quad\left(\frac{\Psi_{ps,\mathrm{meas}}(\lambda_m)-\Psi_{ps,\mathrm{calc}}(\lambda_m)}{\sigma\Psi_{ps}(\lambda_m)}\right)^2+\left(\frac{\Delta_{ps,\mathrm{meas}}(\lambda_m)-\Delta_{ps,\mathrm{calc}}(\lambda_m)}{\sigma\Delta_{ps}(\lambda_m)}\right)^2 \\ +&\quad\left.\left(\frac{\Psi_{sp,\mathrm{meas}}(\lambda_m)-\Psi_{sp,\mathrm{calc}}(\lambda_m)}{\sigma\Psi_{sp}(\lambda_m)}\right)^2+\left(\frac{\Delta_{sp,\mathrm{meas}}(\lambda_m)-\Delta_{sp,\mathrm{calc}}(\lambda_m)}{\sigma\Delta_{sp}(\lambda_m)}\right)^2\right]\end{aligned} \tag{129}$$

$$\begin{aligned}\chi^2_{\mathrm{GE}} =& \frac{1}{6M-F+1}\times \\ &\sum_{m=1}^{M}\left[\left(\frac{\Psi_{pp,\mathrm{meas}}(\lambda_m)-\Psi_{pp,\mathrm{calc}}(\lambda_m)}{\delta\Psi_{pp}(\lambda_m)}\right)^2+\left(\frac{\Delta_{pp,\mathrm{meas}}(\lambda_m)-\Delta_{pp,\mathrm{calc}}(\lambda_m)}{\delta\Delta_{pp}(\lambda_m)}\right)^2\right. \\ +&\quad\left(\frac{\Psi_{ps,\mathrm{meas}}(\lambda_m)-\Psi_{ps,\mathrm{calc}}(\lambda_m)}{\delta\Psi_{ps}(\lambda_m)}\right)^2+\left(\frac{\Delta_{ps,\mathrm{meas}}(\lambda_m)-\Delta_{ps,\mathrm{calc}}(\lambda_m)}{\delta\Delta_{ps}(\lambda_m)}\right)^2 \\ +&\quad\left.\left(\frac{\Psi_{sp,\mathrm{meas}}(\lambda_m)-\Psi_{sp,\mathrm{calc}}(\lambda_m)}{\delta\Psi_{sp}(\lambda_m)}\right)^2+\left(\frac{\Delta_{sp,\mathrm{meas}}(\lambda_m)-\Delta_{sp,\mathrm{calc}}(\lambda_m)}{\delta\Delta_{sp}(\lambda_m)}\right)^2\right]\end{aligned} \tag{130}$$

The quantities involved in all three equations retain the same meanings as the ones in the basic ellipsometry sections 2.2.4. The $\delta\Psi$ and $\delta\Delta$ terms become increasingly more difficult to quantify, but are calculable. It should be noted that the variable M is multiplied by different constants than in the previous section; this is due to the fact that Generalized Ellipsometry collects three times as much information per measurement than standard ellipsometry. The F term retains the multiplier of one out front, but will be inherently higher due to the need of fitting a more complex $\boldsymbol{\epsilon}$.

2.3.5 Measurement techniques.

Making measurements of anisotropic samples is very difficult. Isotropy makes both the modeling and the measurements substantially easier; the only angle of importance is the angle from the normal. However, with the permittivity being heavily dependent on the orientation of the sample, the angle of rotation becomes very important. I sent the following email to Dr. Schubert, one of the worlds foremost anisotropic ellipsometrists, some time ago asking him for any advice that he had on making these measurements:

> I have recently been working on some ellipsometry measurements involving silver nanocolumns, and was hoping that you could give me some advice on fitting the data. Is there some kind of method that you follow for fitting the data? Specifically, I was wondering if there was some kind of order that you take in fitting the data, such as "First, I fit the data along the crystal a axis as a isotropic medium...". I'm having some difficulties in modeling the sample, and would appreciate any insight you might have.

He responded

> The first thing I would do with an unknown sample is to look at Mueller matrix data of a few wavelength versus sample rotation to identify the (an)isotropic nature of the sample. Specifically have a look at the off-diagonal elements versus rotation to see if the structures exhibit biaxial or uniaxial behavior (two or four zero crossings) and how "strong" the anisotropy is (*i.e.* do the off-diagonal elements show maximum amplitudes of 0.6 or only 0.06)? Working 7 years with these structures, I can almost draw a picture of the structures after seeing these data. Cross-section and top view SEM images are always helpful if you have issues with the fits - if something went wrong during deposition and the individual nanostructures are not very defined or do not all have exactly the same direction you won't be able to get a fit without messing with the model.
>
> Take existing effective optical constants and "play" around with the model (biaxial, uniaxial, *etc.*) to learn what has to change to get closer to your measured data. It is important to get the starting parameters right. SEM

> will help you to estimate the slanting angle and thickness and you should know your in-plane orientation actually based on your deposition. What model are you using - a point-by-point approach (what I call HBLA; JAP 114, 083510, (2013)] or do you work with an EMA approach?
>
> If you are working with an EMA approach, use bulk Ag optical constants and keep them fixed in the first step to get in-plane orientation, slanting angle, and thickness roughly right. If your are using a point-by-point approach you can try to approximate as a first step the c-direction with an isotropic Bruggeman EMA mixing void and Ag and just fit the fraction.

Dr. Schubert works mainly with Mueller matrices during his measurements; I would advise the reader to reference [93] for more details on these values.

Speaking from my experience, some of the notes from standard ellipsometry still hold, while others do not. Taking measurements at high angles of incidence (70 to 80 degrees) is still best. While these samples do not have real Brewster's angles, the pseudo-Brewster's angles still operate to reduce measurement noise and error. If the optical axes are not known, these high angle measurements should be done with sample rotations at no less than 45 degree increments, to prevent skipping over any of the optical axes. (Dr. Schubert has an ellipsometer which rotates through all of the sample rotation angles, which is not currently available on the IR-VASE available for use.)

Simply taking angles at higher angles of incidence is no longer sufficient for extracting all of the sample's information; multiple angles of incidence need to be measured to observe all of the optical properties. I opted for ranging the ellipsometry angles from 30 degrees from normal down to 80 degrees. While the higher angles give more accurate data, the lower angles are needed to extract the samples information for the axes that are not fully observed at the higher angles.

Modeling the samples becomes significantly more difficult as well due to the large solution space of the answer. I found the best workflow to be to begin modeling the sample as isotropic using only a single angle of incidence and sample rotation, and examining only the basic ellipsometry data. The sample is slowly expanded from there, first changing the sample to uniaxial, then expanding it to other angles of incidence. Once that fit is modeled accurately, the model should be expanded to the other sample rotations and angles of incidence. A biaxial model should be used at this point, and will give the final model parameters.

2.4 Conclusion

Ellipsometry is a noninvasive methodology for determining the physical characteristics of a material. It is built upon the fact that the polarization of light is affected by physical material parameters, such as the index of refraction or layer thicknesses. In some simple cases, formulas can be derived which directly correlate observed reflectance and transmittance information with material characteristics.

More often than not, the materials that are analyzed are too complex for simple equations. In this case, a material model must be constructed. The polarization characteristics of the model must be compared against the polarization characteristics that are measured, which is done using an appropriate figure of merit. Models must be varied to decrease the figure of merit. Once the figure of merit approaches zero, it can be assumed that both the model and the material share the same physical characteristics, assuming that the model is an accurate representation of the material.

This process becomes much more difficult for anisotropic samples, which must rely on complex electromagnetics to describe the polarization characteristics. The Four-by-four Matrix Methodology accurately describes how light propagates through an anisotropic material, and can be used to find the relevant characteristics. The final step of the process involves converting from absolute field information to relative field phases and amplitudes, which is a noninvertible operation. This operation is necessary in a laboratory setting, as the absolute field phase is not knowable.

Ellipsometry is an incredibly power technique capable of characterizing a huge variety of materials. Unfortunately, much of the strength in this comes with experience in knowing how to accurately describe a model of the material. Even so, it is widely used in both industry and research as a noninvasive method for determining many relevant material parameters.

III. Optical characterization of silver-nanorod thin films grown using oblique angle deposition

Ellipsometry is used to non-invasively determine the optical characteristics of a material. In this chapter, a set of measurements is made on the two silver nanorod samples to determine their anisotropic characteristics. Generalized Ellipsometry is used to extract the index of all three optical axes for both samples, which are then compared against each other. This comparison shows a significant difference in properties between the two samples, which aside from their geometry are identical. This demonstrates a clear linkage between the optical characteristics of nanorod-based materials and their underlying physical geometry. Once understood, this relationship can be utilized to create new materials for specific applications.

The following is a paper entitled "Optical characterization of silver-nanorod thin films grown using oblique angle deposition". This paper was authored by myself, Michael Benson, as well as Piyush Shah, Michael Marciniak, Andrew Sarangan, and Augustine Urbas. It was published May 15, 2014 in the Journal of Nanomaterials of the Hindi Publishing Corporation. This paper was written to summarize optical characteristics of a set of silver nanorods grown by Dr. Shah, and encompasses both ellipsometric measurements as well as absorptance measurements.

3.1 Abstract

Nanorods are metamaterial structures that have been shown to have wide application, ranging from biomedical uses to photovoltaic materials. These materials have unique optical characteristics. In this paper, two silver (Ag) nanorod thin-film samples are created using Glancing Angle Deposition (GLAD) at both near-room temperature (∼300K) and cryogenic temperature (∼100K). Generalized ellipsometry is used to measure the optical constants of the samples. The strong difference be-

tween the optical constants of the constituent materials and those of these thin films shows the characteristics of the samples are due to how their metamaterial structures are defined. The principle optical axes of the films align well with the morphological characteristics of the nanostructures. The axis with the greatest index of refraction remains aligned to the principle axes, but shifts orientation with respect to morphological characteristics between samples. Experimental results show differences in both magnitude and characteristics of the nanorod indexes. Reflectance and transmittance measurements are performed to extract absorptance data. The room-temperature deposited sample shows a higher overall absorptance, while the cryogenic sample shows a clear orientation-dependent absorptance. Polarization data is analyzed to show that the 100K thin film exhibits polarization-dependent absorptance, while the 300K sample's absorptance has a strong orientation dependence.

3.2 Introduction

Materials composed of nanorods can have optical properties that are drastically different than their bulk material counterparts [16, 38, 77]. These structures have found a wide number of potential uses, ranging from biomedical applications [49] to photovoltaic device improvements [40]. The characterization of these structures has been studied extensively in a number of different places [54,71,76,78], focusing mostly on the optical constants of the material. Here, two nanorod samples are characterized using generalized ellipsometry and reflectance-based measurements to examine their varying optical properties, as well as their spectral absorptance properties.

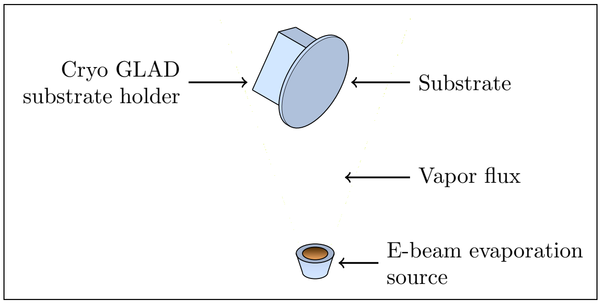

Figure 19. Nanorod growth experimental setup. The sample is tilted at an angle with respect to the incident field to grow the rods at an angle.

3.3 Materials and Methods

3.3.1 Growth Methodology.

The thin-film deposition method discussed in this study was done using a generic e-beam evaporation system (MDC evap-4000) made by Torr International. This chamber was retrofitted with a custom-built substrate holder to support thin-film growth at cryogenic (∼100K) and room (∼300K) temperatures concurrently. Liquid nitrogen was allowed to flow through the substrate holder in an open-loop configuration to achieve cryogenic substrate temperatures during the deposition process. Copper and Teflon angle blocks with a preset angle of 88° were mounted on the substrate holder. Using mechanical clips, silicon (Si) substrates were attached to the angled surface of the block. Two type-K thermocouples were attached to the angle blocks to measure substrate temperature during deposition. This experimental setup is shown in Figure 19. Further detail of this experimental setup is discussed in [85].

Prime grade double-side-polished (DSP) p-type Si <100> wafers were used in this study. Partial wafers were cleaned using acetone, methanol and isopropyl alcohol followed by nitrogen blow drying. The silver (Ag) evaporation pellets were 99.99% purity from Kurt J. Lesker Company. The chamber base pressure was less than 66×10^{-6} Pa (0.5×10^{-6} Torr) prior to the start of the deposition. After the initial pre-conditioning ramp, the final deposition rate was maintained at 0.3 nm/s. Film

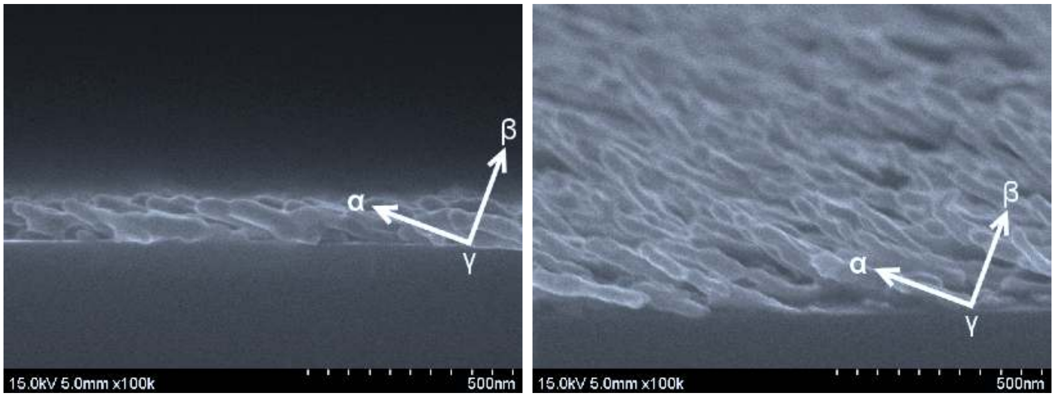

Figure 20. SEM images of silver nanorods. Left sample was grown at 300K, while the right sample was grown at 100k.

thickness was monitored using SQC-310 thin-film deposition controller, manufactured by Inficon.

Top view and cross sectional scanning electron microscope (SEM) images were acquired using Hitachi S-4800 high resolution SEM system and are shown in Figure 20. ImageJ software was used to structurally characterize morphological differences among the 300K and 100K grown Ag-nanorod thin-film samples.

3.3.2 Spectral Ellipsometry Measurements.

Ellipsometry measures the complex reflection coefficient [102]. This data is typically compared against a model of the material components to evaluate the actual parameters of the sample. In spectral ellipsometry, a broadband source is combined with a series of polarizing optics to illuminate a sample with an exact polarization state. A detector then views the specular reflectance of the sample through another polarizing optic to measure the proportion of light reflected by the sample.

The complex reflection coefficient can be described as

$$\rho_{pp} = \tan(\Psi_{pp}) \exp(i\Delta_{pp}) \tag{131}$$

where $\tan(\Psi_{pp})$ is the ratio of the amplitude of light horizontally polarized over that vertically polarized, and Δ_{pp} is the phase delay between the two orthogonal fields [32].

Fundamentally, this complex reflection coefficient relates back to the reflection Jones matrix of the sample. An element with a reflection matrix of

$$R_j = \begin{bmatrix} r_{pp} & r_{sp} \\ r_{ps} & r_{ss} \end{bmatrix} \tag{132}$$

will have a complex reflection coefficient equal to $\rho_{pp} = r_{pp}/r_{ss}$. Two other complex reflection coefficients are commonly used,

$$\rho_{sp} = \frac{r_{sp}}{r_{ss}} \tag{133}$$

$$\rho_{ps} = \frac{r_{ps}}{r_{pp}}, \tag{134}$$

and give new information of the relative Jones matrix. These reflection coefficients (and hence corresponding Ψ and Δ) can be extracted using Generalized Ellipsometry. Extraction methods are detailed in [82], and were previously detailed in 2.3. These additional two reflection coefficients are very important for measuring biaxial samples. A biaxial material's Jones matrix is non-diagonal everywhere except for the principle axes. These extra measurements are required to properly extract the material parameters.

This data is typically measured as a function of angle of incidence, ψ, as measured from the surface normal. The reflection coefficient changes significantly given any change of material parameters, such as layer depth or surface roughness, making the measure of Ψ and Δ over a range of angles fairly material specific.

The complex reflection coefficient, and hence Ψ and Δ, can easily be modeled given material parameters. Because these parameters are calculated, they can be quickly

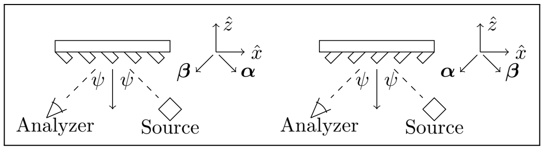

Figure 21. Ellipsometry experimental setup. The diagram on the left demonstrates the orientation "INTO," while the diagram on the right demonstrates the orientation "AGAINST."

varied by a computer to create a broad range of Ψ and Δ data. These simulations are then compared to the measured data. If the modeled data and the measured data align well, it can be assumed that the sample is well described by the model.

Nanorods typically exhibit biaxial properties [28, 75, 77, 81], which means that complex refractive index, $n + ik$, is not the same for every orientation or angle ψ. Biaxial materials have three principle axis ($\boldsymbol{a}, \boldsymbol{b}, \boldsymbol{c}$, denoted as $\boldsymbol{\alpha}, \boldsymbol{\beta}$, and $\boldsymbol{\gamma}$ in Figure 20), each of which has a different index of refraction. In many applications, these axes do not line up with the laboratory frame of reference, which makes them difficult to measure due to the immense solution space [81]. Ellipsometric models can be set up to generate biaxial data, which can then be used to estimate the angles of these axes. Typically, these angles correspond with properties of the materials, such as the direction of the nanorods [75].

In our experiment, we found that the axis with the highest real part of the refractive index measured at the lowest sampled wavelength changed between samples. Due to the confusion of having the axes' names change between samples, these axes are instead designated $\boldsymbol{\alpha}$, $\boldsymbol{\beta}$, and $\boldsymbol{\gamma}$, which were chosen to correspond with the morphological characteristics of the sample and are aligned with the optical axis. $\boldsymbol{\alpha}$ corresponds with the direction of the nanorods, $\boldsymbol{\gamma}$ is perpendicular to $\boldsymbol{\alpha}$ in the plane of the substrate, and $\boldsymbol{\beta}$ is perpendicular to the other two pointing away from the surface. In other models, $\boldsymbol{\alpha}$ and $\boldsymbol{\beta}$ do not have to necessarily be perpendicular to each other. Here, they are defined as perpendicular.

Previous studies of nanorods point to the fact that the material will have biaxial properties, and these axes typically align with the direction of the rods [74]. Knowing this, the ellipsometric measurements were taken along three directions: the plane of $\boldsymbol{\alpha}$ and $\boldsymbol{\beta}$ on the side of $\boldsymbol{\alpha}$ (also designated "INTO", as the nanorods point towards the source), the same plane on the opposite side (also designated "AGAINST", as the nano rods point away from the source), and the plane of the sample normal and $\boldsymbol{\gamma}$ (also designated "ACROSS", as the nano rods are perpendicular to the source). An example of these orientations can be seen in Figure 21. This allows us to collect data along all three of the principle axes of the sample, which can be used to extract the relevant material parameters using an ellipsometric model. An example of the experimental setup used showing the sample orientation can be seen in Figure 21. Data collection was performed using J. A. Woollam Co.'s IR-VASE, and analysis was carried out using the associated software [101].

3.3.3 Hemispherical Reflectance and Transmittance Measurements.

While ellipsometry measures specularly reflected light, light scattered at other angles can also be used to identify specific material parameters, such as absorptance. Typically, absorptance is fairly difficult to measure directly, but it can be extracted from reflectance and transmittance data. Conservation of energy states that absorptance (A), reflectance (R) and transmittance (T) are related by

$$1 = A(\psi) + R(\psi) + T(\psi). \tag{135}$$

Absorptance can also be found given the real and complex index of refraction, n and k, values of the material. Absorptance is calculated as

$$A = \exp\left[-2k\frac{c}{\omega}\frac{d}{\cos\theta}\right] \tag{136}$$

where ω is the frequency of the incident light, c is the speed of light, d is the material thickness, and θ is the angle of propagation within the sample. Because k is divided by λ_0, samples will have high absorptance when they have lower k (but > 0) values at shorter wavelengths or higher k values at longer wavelengths.

Reflectance and transmittance measurements were made using the SOC-100 which measures Hemispherical Directional Reflectance (HDR) and Hemispherical Directional Transmittance (HDT). Because of this, special care must be taken to ensure proper measurement of these nanorod samples. The sample must be mounted upside down relative to the reflectance measurement to properly measure the transmittance of the sample. This is shown in Figure 22.

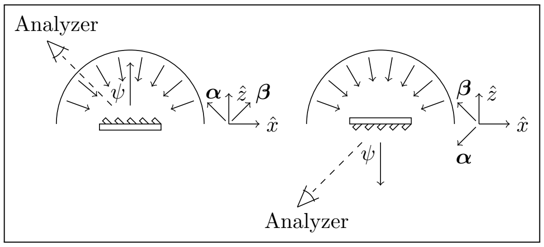

Figure 22. Reflectance (left) and transmittance (right) experimental setup. Both diagrams show the orientation "INTO".

3.4 Results and Discussion

3.4.1 Sample Characteristics.

Figure 20 showed the top and side view SEM images for 300K and 100K grown Ag nanorod thin films. The distinct morphological differences in the structure of these films are evident from these images. The nanostructure of 300K grown films is in agreement with previously reported results in literature [12, 47]. Compared to 300K, 100K grown thin films appear to have distinctly separate nanorods with smaller diameter. The 300K sample has partially collapsed nanostructure with larger-diameter nanorods. This fact is not obvious unless the structure of the film is investigated using cross sectional view. Based on the observed differences in the diameter, length, number of nanorods per unit area, and nanorod spacing, it appears that the available Ag nanostructured surface area of the 100K films will be larger than that of the 300K grown thin films. Therefore, it is expected that the 100K and 300K grown thin films will exhibit different plasmonic, optical, electrical, and mechanical properties. The difference in the evolution of thin films and quantitative morphological differences of these films is discussed in our previously reported study [85].

3.4.2 Optical Constant Extraction.

The n and k values extracted along the principle axes are shown in Figure 23. The structure of the nanorods obviously has a strong impact on the overall characteristics of the metamaterial as a whole. Neither sample exhibits any behavior that can be attributed to a simple layered material model. These values (summarized in Table 2) were extracted by fitting the measured data to a biaxial layered model. Given the average film thickness (taken from the SEM images), n and k were varied to match the collected generalized ellipsometry data.

Table 2. Modeling parameters and measurements for both sample grown at 300K and sample grown at 100K.

	300K Sample		100K Sample	
	Model Parameter	SEM Measurement	Model Parameter	SEM Measurement
Layer depth [nm]	135 nm	128 nm – 160 nm	115 nm	110 nm – 120 nm
Nanorod angle [deg]	84°	68° – 72°	84°	68° – 72°

Both samples exhibit clear anisotropic behavior. The effective index changes considerably as a function of the orientation and the angle ψ. More significantly, each sample demonstrates unique behavior, indicating that the sub-wavelength structures

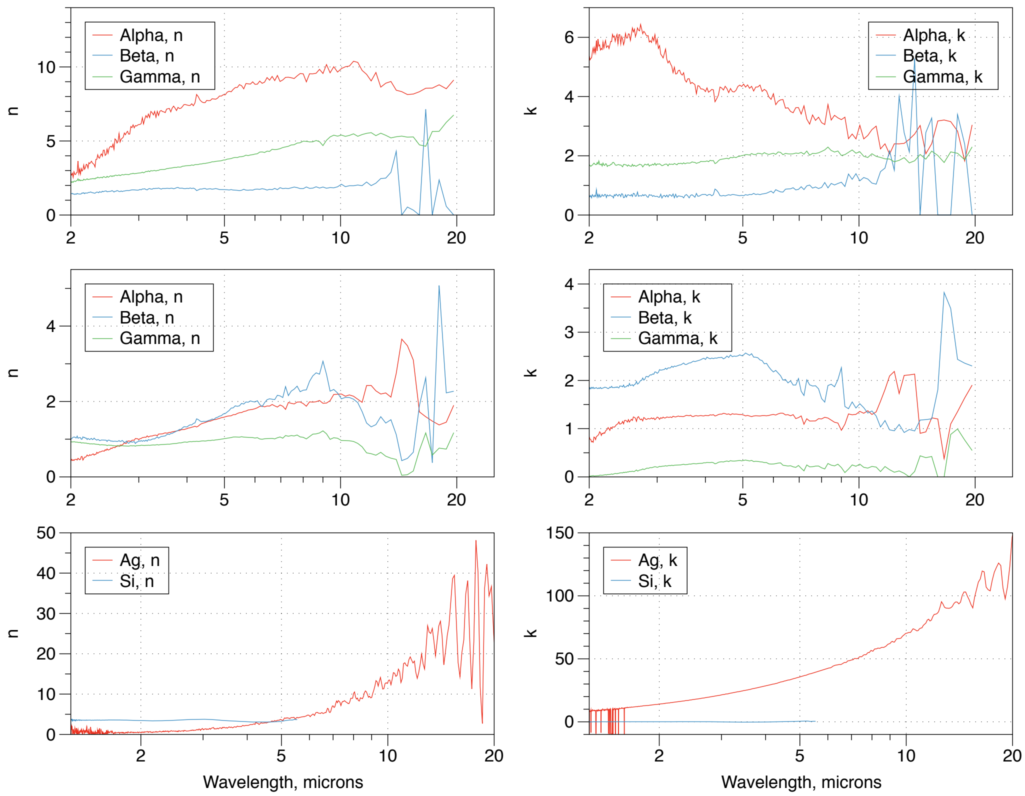

Figure 23. Measured n (left) and k values (right). Sample grown at 300K shown on top, while the sample grown at 100K is shown in the middle. $\boldsymbol{\alpha}$ corresponds with the direction of the nanorods, $\boldsymbol{\gamma}$ is the perpendicular of $\boldsymbol{\alpha}$ lying in the plane of the sample, and $\boldsymbol{\beta}$ is the perpendicular to the two previous vectors. The n and k values extracted for the Si substrate and Ag deposition are shown at the bottom.

are responsible for the material's response. Both sets of nanorods have complex indexes significantly higher than that of the substrate and significantly lower than that of the Ag deposition (also shown in Figure 23).

The 300K sample has an index that is highest along the direction of the nanocolumns. This behavior has been observed in other nanorod samples at shorter wavelengths [78]. This index has a high complex component, which would imply that the absorptance in this direction would be comparatively higher. The complex portion decreases sharply towards 5 µm, where it approaches the behavior of the other two axes.

The 100K sample has a much different behavior. Here, the index along the $\boldsymbol{\alpha}$ axis starts lower than the other two, then increases to approximately the behavior of the

$\boldsymbol{\beta}$ axis. This behavior has also been observed in other nanorod samples [75]. This axis has a complex part of the index that is lower than the $\boldsymbol{\beta}$ axis, which is contrary to the 300K sample. The real portion of the index along $\boldsymbol{\alpha}$ crosses the $\boldsymbol{\gamma}$ index at 2.65 µm, and crosses the $\boldsymbol{\beta}$ at both 2.82 µm and 3.75 µm.

While both of these behaviors have been noted before, these samples are novel because they exhibit both behaviors. The most significant difference between the two samples is the geometry of the nanorods, implying that this difference is responsible for this unique behavior.

These two structures have significantly different effective optical constants. The optical axes of these materials always roughly aligns with the morphological characteristics of the sample, which is why the $\boldsymbol{\alpha}$, $\boldsymbol{\beta}$, and $\boldsymbol{\gamma}$ axes were chosen instead of the typical n_a, n_b, and n_c axes found in similar papers. Choosing these axes allows for a much clearer comparison between the two samples.

Similar structures have been well described using a Bruggeman Effective Medium Approximation [76]. Typically, this kind of film would be a silver and void mixture with a void fraction percentage likely around 70% with some depolarization factor. For our particular sample, these parameters were not of great importance; the effective index of the material was needed to correlate with the measured absorptance data.

The orientation of the optical axes was easily extracted for both samples, and is shown in Figure 20. For the 300K sample, the orientation of the $\boldsymbol{\alpha}$ axes is located at 83.76° from normal. Fitting placed $\boldsymbol{\gamma}$ at 89.9° from normal, and $\boldsymbol{\beta}$ axis at 6.21° from normal, on the opposite side of the $\boldsymbol{\alpha}$ axis. This confirms that the $\boldsymbol{\gamma}$ axis is in the plane of the sample. Similarly, for the 100K sample, the orientation of the $\boldsymbol{\alpha}$ axis was located at 83.89° from normal. The $\boldsymbol{\beta}$ axis is oriented at 8.26° from normal. $\boldsymbol{\gamma}$ axis is a bit further from the plane of the substrate, oriented 5.53° above the plane of the sample.

3.4.3 Absorptance Calculations.

The absorptance is calculated using Eq. (135) with the reflectance and transmittance measurements. The absorptance of the Si substrate is shown in Figure 24. The absorptance of the substrate shows two peaks inconsistent with the ellipsometric data discussed in Section 3.4.2. The peak occurring at 9 µm and 16 µm are due to interstitial oxygen present in the Si. This is commonly found in silicon grown by Czochralski method [2].

Note that the absorptance is polarization dependent. This is due to the difference in reflectance between the two orthogonal states; the perpendicular polarization state is prevented from exiting the material. The reflected portion of the energy passes through the layer again, where it has another chance to be absorbed, which in turn leads to a higher absorptance.

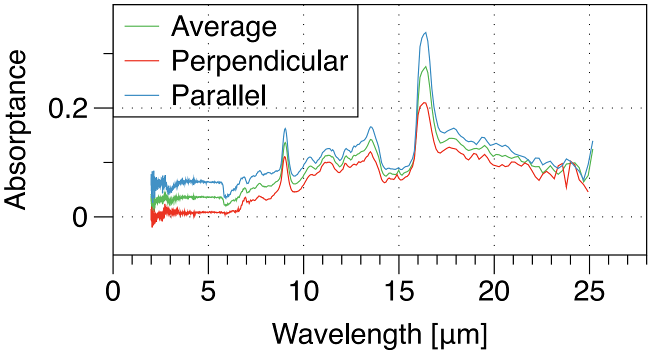

Figure 24. Polarization based absorptance for Si substrate.

The spectral reflectance and transmittance measurements of the samples are shown in Figure 25. The 300K sample has a significantly lower reflectance than the 100K sample. The "INTO" orientation reflects significantly better than the "AGAINST" orientation; the "AGAINST" and "ACROSS" transmittance measurements are nearly identical for this sample; and the "INTO" orientation transmits better at longer wavelengths.

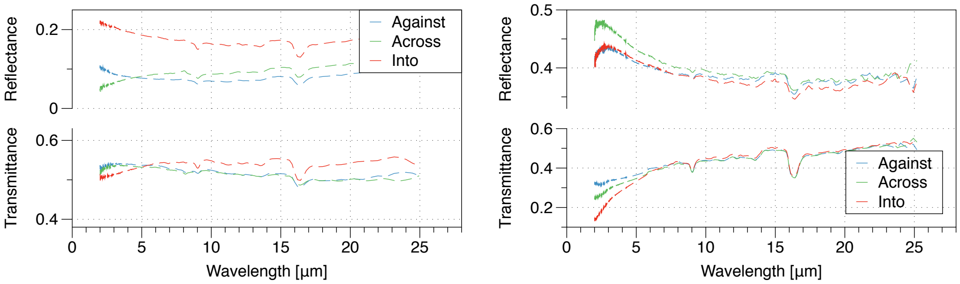

Figure 25. Reflectance and transmittance measurements for unpolarized light at $\psi = 70°$. Left sample was grown at 300K, while the right sample was grown at 100k.

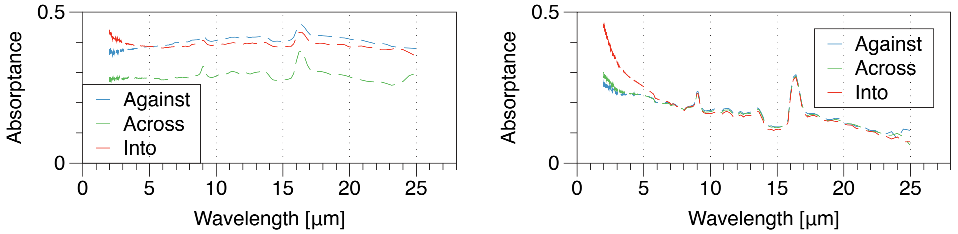

Figure 26. Absorbance measurements for unpolarized light at $\psi = 70°$. Left sample was grown at 300K, while the right sample was grown at 100k.

The 100K sample has clearly different reflectance and transmittance properties (Figure 25 (right)). All three orientations have very similar characteristics, with the "ACROSS" orientation showing slightly higher reflectance. For transmittance, all three measurements are nearly identical after about 7 µm. For the shorter wavelengths, there is a large difference between the "AGAINST" and "INTO" orientations, contrary to what was observed in the 300K sample.

The absorptance measurements show a significant difference between the two samples. These measurements are shown in Figure 26. The sample grown at 300K absorbs light over the infrared wavelength range significantly better than the sample grown at 100K. The "INTO" absorptance is slightly higher than the "AGAINST" absorptance at wavelengths lower than about 5 µm. This measurement corresponds well to the indices presented in Figure 23. For example, the imaginary portion of the index along $\boldsymbol{\gamma}$ is very low, which matches very well with the much lower absorptance for the "ACROSS" measurement.

For the 100K sample, all three orientations have nearly identical absorptance at wavelengths longer than about 6 µm. At shorter wavelengths, the “INTO” orientation has a much stronger absorptance than the other two orientations. This is a characteristic shared by both samples. “ACROSS” and “AGAINST” have very similar absorptances throughout the entire range of wavelengths examined here. Again, this matches well with the indices in Figure 23. The $\boldsymbol{\alpha}$ axis has a much higher imaginary index, correlating with the higher absorptance.

The absorptance measurement can also be decomposed into separate polarization states. This is shown in Figure 27. Additional measurements (not shown here) show that the differences are due to an inability for the sample to transmit the parallel (TM) polarization state. Normally, this state is easily transmitted through the sample. The inability to transmit this energy, which has already been coupled into the material, manifests as increased absorptance.

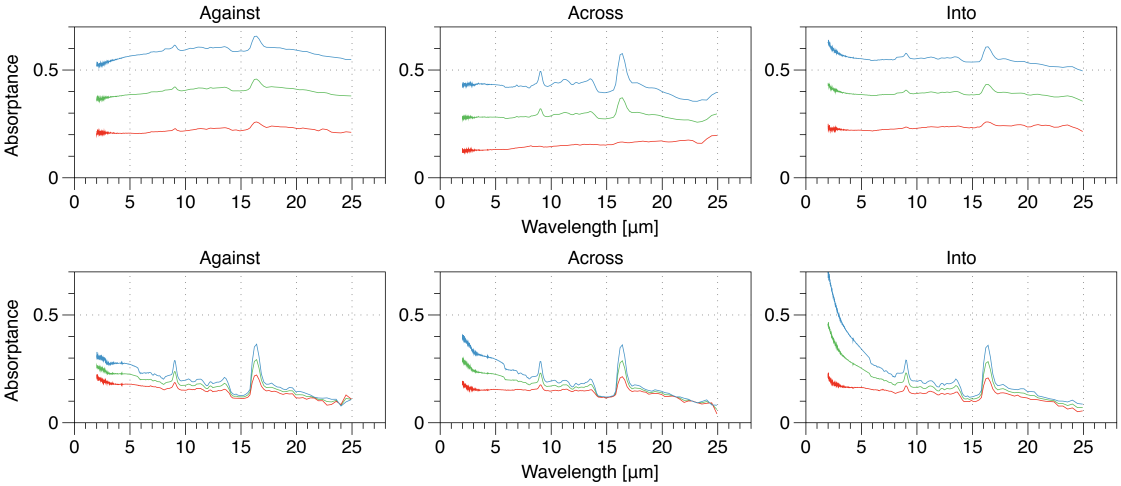

Figure 27. Polarization-based absorptance for the sample grown at 300K (above) and 100k (below). Blue is the parallel (TM) polarization state, red is the perpendicular (TE) polarization state. The green line is unpolarized.

Furthermore, the polarization-based absorptance displays some unique characteristics. The absorptance shows a very clear polarization dependence of the 300K material. In all orientations, the parallel polarization is most strongly absorbed. The

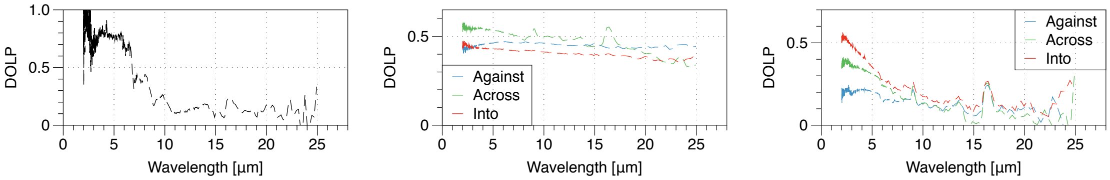

Figure 28. DOLP measurement for Si substrate (left), sample grown at 300K (center), and sample grown at 100K (right).

"INTO" absorptance shows the least difference between polarizations, likely due to the light being incident on the top of the nanorods. Because of the cylindrical symmetry, there is very little difference between polarization states. This would explain the lower Degree of Linear Polarization (DOLP) for this orientation in Figure 28.

The "AGAINST" orientation shows the highest difference in absorptance between polarization states. In this case, the direction of the incident light is normal to the nanorods, which would explain why the two polarization states interact with the material so differently. "ACROSS" shows similar trends to the other two orientations, but to a lesser degree.

The polarization-based absorptance data for the sample grown at 300K shows very little polarization-based absorptance (Figure 27 (top)). All three orientations have similar DOLP values in Figure 28, averaging around 0.5. These values are very different than the DOLP for the Si substrate (also shown in Figure 28, which averages around 0.75 between 2 and 7 µm, and then drops to around 0.25.

3.5 Conclusion

These Ag nanorod thin films have exhibited strong metamaterial properties in the sense that they are well described by an effective medium approximation. Glancing angle deposition at cryogenic temperatures created a nanorod sample that has significantly different morphological properties than a similar sample grown at room temperature. Ellipsometry reveals that these two samples have greatly varying optical properties. Notably, the optical axis with the highest refractive index changed places with respect to the axes defined by the morphological features of the nanorods between the samples. The 300K sample demonstrates a much higher set of indices than does the 100K sample. The 100K has significantly different behavior than that of the 300K sample. The absorptance of both samples has been measured. Absorptance measurements correspond well with the measured material indices. The 100K sample exhibits a much lower difference in absorptance at wavelengths longer than 6 µm, while proving strongly orientation dependent in the shorter wavelengths. The 300K sample shows a smaller orientation dependence, but across the entire infrared band. These measurements show the impact of the sub-wavelength structures on the observable optical properties of nanorod metamaterials.

IV. Parameter Extraction

Ultimately, the goal of this research is to determine the relationship between the geometry and the optical characteristics of the nanorods. As demonstrated in the previous chapter, there is a clear difference between the optical properties of the two samples. This indicates that there is a clear relationship between the optical characteristics of the material and the underlying physical geometry. Understanding this relationship will allow for the design of materials tailored for specific uses. These relationships are best determined through extracting the effective material parameters from simulated models of the materials.

Finding closed-form solutions to the fields scattered by anisotropic materials quickly becomes intractable [42]. The complexity of a solution given some incident field grows exponentially with the geometry of the problem [11]. Because of this, it is often much easier to turn Computational Electromagnetics (CEM) to understand how light interacts with a structure. CEM takes a problem that would be impossible to solve analytically, and transforms it into a problem which can be easily solved by a machine [98]. The sacrifice of this particular methodology is that the computational solution introduces an error that would not be present otherwise. However, it has the advantage that nearly any problem that can be posed in the physical world can be solved in the circuits of the computer.

However, the simulations of a computer only give information about the fields. This information is next to useless on its own. Unless the topic of discussion is how light at that frequency reflects off that surface at that angle, the simulation does not provide any useful information. The problem then becomes, what information can be gained from performing a simulation? The answer is, the effective characteristics of the material can be determined based on the fields scattered [88]. CEM modeling gives information about the fields, which gives information about the effective parameters.

These effective parameters can be used to begin to answer those questions stated above.

The goal of this chapter is to explain the process of how effective material parameters are extracted from a computational electromagnetic simulation. This process was designed over the course of my candidacy specifically for this particular project. Most effective parameter extraction processes require specific sets of assumptions. Specifically, other methodologies assume the alignment of the optical axes with the frame of reference of the experiment. In some structures, such as the ones examined in this work, this is not a viable assumption; the axes are not orthogonal, much less aligned. The methodology detailed here is free of this particular assumption, which enables it to be used in places where previous techniques cannot be used.

This chapter goes through the derivation of the Permittivity and Permeability Tensor Extraction (PPTE) technique, and then uses it on a small set of situations to establish both its accuracy and its usefulness in this particular problem. The chapter begins with the fundamental process of ellipsometry, which is the only extraction technique that is viable with structures such as nanorods, and explains why the process is not ideal.

The next section encompasses the calculation of the T matrix, which is the last step in the Four-by-four Matrix Formalism, and the first step in PPTE. From there, the matrix Δ_B is easily found. This matrix contains the information necessary to find the permittivity and permeability. The equations required for this are detailed in the next section of the chapter. Finally, several simulations are analyzed using this technique to establish both the accuracy and the utility of the PPTE technique. The majority of this research was recently accepted for publication within the IEEE Photonics Journal [13].

4.1 Ellipsometry process versus an ideal process

Everything in ellipsometry is governed by the figure of merit [44]. In order to arrive at the model of some sample, there is a two-branch process which needs to be performed some number of times. This becomes an iterative process [43], with the measured data being the metric by which the model is judged. A computer is used to automatically vary the parameters of the model. These variations affect the figure of merit, which is used to guide the computer towards the solution. Typically, algorithms such as a Levenburg-Marquette solver are used to minimize the figure of merit [46]. The solution determined by the algorithm may be the best solution, or may require some user intervention to arrive at a better solution. Much of the process is dependent on the skill of the person in control of the process.

This solution is presently necessary in laboratory work due to certain physical constraints. As the wavelength of light decreases, determining the absolute phase of a wave becomes impossible [37]. This limits the amount of usable information present. Ellipsometry combats this constraint by limiting the measurement and calculations to the relative phase and amplitude of the waves. This step imposes limits on the amount of collected information, but is necessary for laboratory work.

This is a constraint that is not present in simulations. The process of ellipsometry has a final, non-invertible step (as shown in Section 2.3.3) that does not need to be non-invertible. Using the extra information that is present in a simulation, the process can be altered slightly. Instead of comparing relative phases generated by a model to those measured in an experiment, the absolute phases can be used to calculate the T matrix used in generalized ellipsometry, which can be used to yield the parameters of interest.

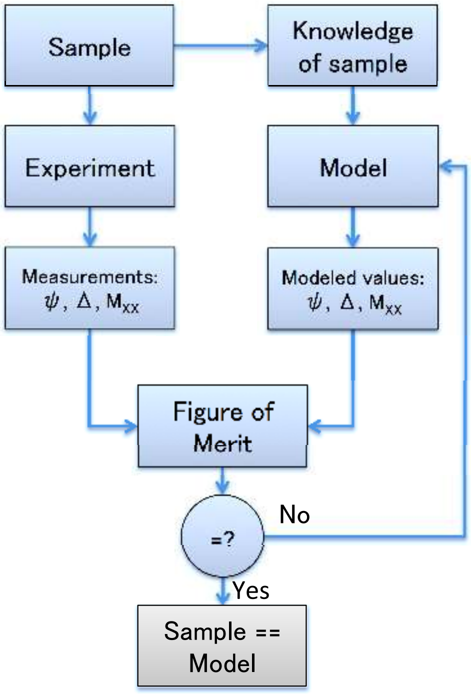

Figure 29. Process of Ellipsometry. Note that this is an iterative process based on the Figure of Merit.

4.1.1 Process of Ellipsometry.

Performing ellipsometry is a process with two distinct branches [1], which is depicted in Figure 29. The first branch is an experimental branch. A sample is placed in the instrument, the sample is illuminated with polarized light, the reflected or transmitted light is detected, analyzed, and processed into ellipsometric data. This data typically takes the form of the Ψ and Δ angles, or sometimes the elements of the Mueller matrix as a function of wavelength.

The second branch begins with some sort of knowledge of the sample being measured. What are the material components? How thick are the layers? Is there some unique property of some layer? It's not unreasonable to assume that many of these are known to an extent (for example, a layer designed to be 250 nanometers thick should be approximately 250 nanometers thick, not 20 nanometers or 2 microns). The more complex the sample is, the more about it needs to be known; for instance, the nanocolumns need to be analyzed knowing that they are biaxial in nature, and have some known, approximate orientation.

From this known information, a model is created [45]. This model utilizes as few or as many variables as the user desires. The process is often begun assuming that the materials are ideal materials, where their permittivities are the same as those of a measured canonical sample. The beginning model typically utilizes a small number of variables, such as layer thicknesses and perhaps layer roughnesses. The number of variables can be expanded from here to include any number of things. For instance, a group of variables might describe a layer permittivity as a sum of oscillators, as seen in Section 2.2.3.

The model is then used to compute ellipsometric data. This ellipsometric data is compared against the measured data using some FoM [44], as detailed in Section 2.3.4. The FoM gives a single, positive, real valued number to describe the degree of sameness between the measured and modeled data. When the two data sets are the same, the FoM returns a value of zero. For experimental work, measurement noise means the FoM can only approach zero. The software performing the ellipsometry must then use the FoM to determine a better model to describe the data. A gradient-based approach is often used, analyzing each variable to determine what change will bring about a better FoM. The model is then changed, and the ellipsometric values are recalculated. At some point, the FoM will reach a minimum, be it local or global, at which point the process comes to a halt.

It is up to the user at this point to determine what to do next. The user might decide to change the model in some way, perhaps adding or subtracting variables. The user might decide to begin the process anew using a new initial condition. The user might decide that the current model is optimal, and move forward assuming that the parameters estimated by the process are correct.

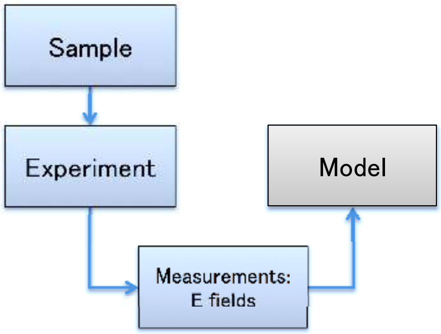

Figure 30. Process of Permittivity and Permeability Tensor Extraction. This process is linear.

This iterative process has been used in an extraordinarily wide number of cases [9, 16, 27, 28, 38, 49, 76, 77, 85].

4.1.2 Permittivity and Permeability Tensor Extraction Technique.

Ellipsometry is not an invertible process. The ellipsometric data generated by the experiment cannot be directly examined for any relevant information about the sample being measured. This is due, in part, to the inability for an ellipsometer (and indeed, almost any optical experimental setup using waves shorter than microwaves) to record the absolute phase of the wave [37]. The process is fundamentally reliant on a set of incomplete information. This is not to say that the answers derived from this process are wrong, just that it requires a different process to arrive at the best solution.

In simulation, this unobtainable information is readily available. This more complete set of information can be used to make the process underlying ellipsometry an invertible process. This process is shown in Figure 30.

The Four-by-four Matrix Formalism is a method for dealing with anisotropic samples. It uses a 4x4 matrix which relates the E fields on one side of the sample to those found on the other. Ellipsometry does not have access to these E fields; instead, it uses the relative amplitude and relative phase within the process. This process converting from relative amplitudes and phases is non-invertible, but necessary. Within the optical regime, calculating the exact phase of a wave is almost impossible.

In this extraction process using simulated fields, these absolute phases are known. This transforms the relationship between the "measured" (simulated) data and the four-by-four matrix into one which is almost always invertible. (The cases where it is not will be addressed in depth in this chapter.) Using a set of four simulations encompassing 16 measurements, all 16 complex elements of the four-by-four matrix can be known explicitly.

The process between the four-by-four matrix and the permittivities is also an invertible process. The projection matrices used within the process are invertible by definition, and the remainder of the process is simple linear algebra using known values. This gives the matrix Δ_B as a function of the simulated data.

The matrix Δ_B has a distinct form which is given by Berreman [15]. His derivation calculates how a plane wave of a given frequency and angle propagates through a infinite planar slab of some material with a given permittivity, permeability, and electro-optic coupling tensors. His work is the cornerstone of the four-by-four matrix method [79], and is thus utilized in all anisotropic ellipsometry. The underlying form of the matrix Δ_B can be used to analyze the calculated value of Δ_B to unambiguously extract the values of these tensors. In ellipsometry, it is assumed that only the permittivity tensor is pertinent [10], but the following derivation assumes generalized permittivity and permeability tensors. This technique could likely be extended into even more generalized materials, but these cases will not be explored here.

This gives an invertible process to go from simulated data directly to effective material parameters.

4.2 Problem Setup

The parameter extraction process follows a five step process. The first is the calculation of the T matrix, which describes the interaction between the incident, reflected, transmitted, and back-traveling waves. The second step uses the calculated T matrix to calculate T_{Π}, which performs the same function as it did in the ellipsometry process. From T_{Π}, step four involves calculating the matrix Δ_B. Finally, the permittivities and permeabilities are extracted from the matrix (or, in some cases, multiple matrices) Δ_B.

4.2.1 Methodology advantages.

The first and most obvious advantage of this process is the fact that this is a linear process. Data in the form of measured fields or coefficients are input into a process which will always result in the same permittivities and permeabilities. There are no parameter estimation or error correction processes. Another advantage is that there is no solution ambiguity. Ellipsometric quantities are always given with uncertainties, to indicate how unsure the process is of the result. This method does not provide these uncertainties separate from the measurement noise, as the extracted quantities can be used to return to the measured quantities.

4.2.2 Methodology short comings.

The biggest difficultly with this process is the reliance on absolute amplitudes and phases of the fields. It is possible that these values are not as necessary as proposed here, but as of the writing of this document, the absolute amplitudes and phases are needed. This makes this process intractable for most laboratory work in the infrared and higher frequencies. The amplitudes and phases of microwaves and longer wavelengths can be known, and this process can be hypothetically used within this regime. However, it is at present not useable in a laboratory setting.

Another difficulty is a lack of an uncertainty of the extracted values. Tracking uncertainty is possible for the initial step or two, but tracking uncertainty through inverting an matrix exponential operation is prohibitively difficult. The actual uncertainty of the extracted values is not addressed in this document.

4.3 T matrix conversions

In traditional ellipsometry, the T matrix is an intermediate step between defining the permittivities and finding the ellipsometric ratios. In this extraction methodology, the T matrix takes on a slightly more prominent role. One use is in going from the E fields to the extracted parameters. The other use is in starting with parameters, and converting to the scattered fields. This requires the conversions involving the T matrix to be more robust here than how it has been used traditionally. Here, its conversions are defined and examined.

4.3.1 Finding the T matrix given the E fields.

Finding the T matrix given the E fields begins by assuming a few simple linear relations. It assumes there exists a

1. linear relationship between incident and reflected waves,
2. linear relationship between incident and transmitted waves,
3. linear relationship between back-traveling and reflected waves, and
4. linear relationship between back-traveling and transmitted waves.

These are fundamental assumptions in any kind of parameter extraction, and are well founded assumptions for passive metamaterials in regions where the effective medium approximation is valid. (Typically, the effective medium regime is at wavelengths greater than ten times the feature size. In practice, it is much closer to two or three times feature size [65].)

Calculating the T matrix begins with two experiments: one where the incident light is S-pol oriented, and one where the incident light is P-pol oriented. The incident light can have any amplitude and phase, but it makes more sense to talk of the experiment where the incident light is normalized to have an amplitude of 1 and a phase of 0. The reflected waves will have the same values as the complex reflection/-transmission coefficients under these conditions. Performing these two experiments will result in the following values:

$$\left.\begin{array}{ll} E_S^r(i:S) & E_S^r(i:P) \\ E_P^r(i:S) & E_P^r(i:P) \\ E_S^t(i:S) & E_S^t(i:P) \\ E_P^t(i:S) & E_P^t(i:P) \end{array}\right\} . \tag{137}$$

The superscripts refer to the measurement being either of the reflected (r) or transmitted (t) wave. The subscripts refer to the measurement of either the S-pol or P-pol wave. The notation inside the parentheses indicates that the measurement was made while either S-pol or P-pol light was incident ($i : S$ or $i : P$, respectively). The locations and orientations of these waves is shown in Figure 31. This figure is very similar to Figure 15, but with the inclusion of the back-traveling wave.

The Four-by-four Matrix Formalism, described in Section 2.3.3, gives that the relationship between the measurements can be expressed in the following two equations,

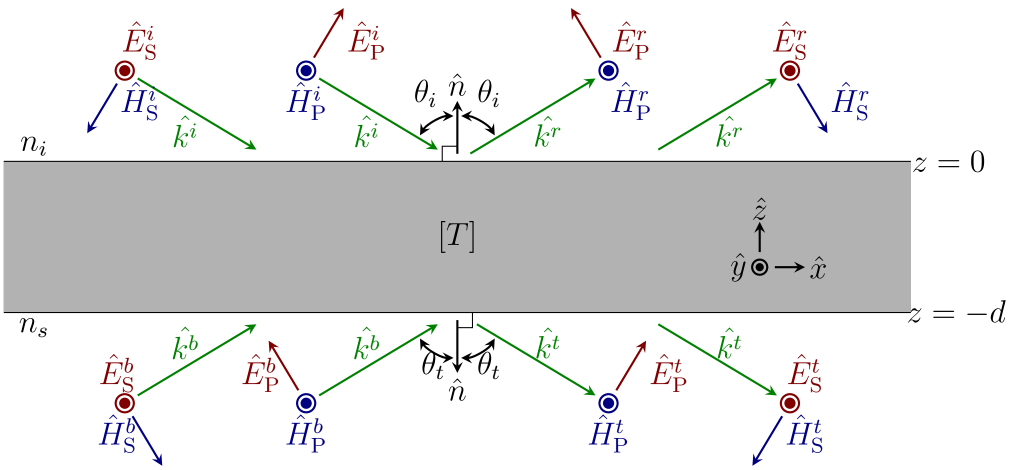

Figure 31. The T matrix converts from the incident and reflected fields to back-traveling and transmitted fields. The i superscript indicates incident fields, r indicates reflected fields, b indicates back-traveling fields, and t indicates transmitted fields. The k vectors indicate the direction of propagation.

as stated previously in Equation (86). For S-pol light incident,

$$\begin{bmatrix} 1 \\ E^r_S(i:S) \\ 0 \\ E^r_P(i:S) \end{bmatrix} = \begin{bmatrix} T_{11} & T_{12} & T_{13} & T_{14} \\ T_{21} & T_{22} & T_{23} & T_{24} \\ T_{31} & T_{32} & T_{33} & T_{34} \\ T_{41} & T_{42} & T_{43} & T_{44} \end{bmatrix} \begin{bmatrix} E^t_S(i:S) \\ 0 \\ E^t_P(i:S) \\ 0 \end{bmatrix}. \tag{138}$$

The incident light is purely S-pol, which leads to the 1 and 0 in the first and third position of the left-hand-side vector. Since there is no back-traveling wave, the right-side vector has zeros in both the second and fourth position. For P-pol light incident, the equation changes slightly, and uses the second set of measurements:

$$\begin{bmatrix} 0 \\ E^r_S(i:P) \\ 1 \\ E^r_P(i:P) \end{bmatrix} = \begin{bmatrix} T_{11} & T_{12} & T_{13} & T_{14} \\ T_{21} & T_{22} & T_{23} & T_{24} \\ T_{31} & T_{32} & T_{33} & T_{34} \\ T_{41} & T_{42} & T_{43} & T_{44} \end{bmatrix} \begin{bmatrix} E^t_S(i:P) \\ 0 \\ E^t_P(i:P) \\ 0 \end{bmatrix}. \tag{139}$$

Since the right-hand side vector has two zeros in it, the second and fourth column of the matrix can be ignored, which simplifies the equations. This gives four sets of two equations each relating the various measurements:

$$\left.\begin{aligned} 1 &= T_{11}E_S^t(i:S) + T_{13}E_P^t(i:S) \\ 0 &= T_{11}E_S^t(i:P) + T_{13}E_P^t(i:P) \end{aligned}\right\} \tag{140}$$

$$\left.\begin{aligned} E_S^r(i:S) &= T_{11}E_S^t(i:S) + T_{13}E_P^t(i:S) \\ E_S^r(i:P) &= T_{11}E_S^t(i:P) + T_{13}E_P^t(i:P) \end{aligned}\right\} \tag{141}$$

$$\left.\begin{aligned} 0 &= T_{11}E_S^t(i:S) + T_{13}E_P^t(i:S) \\ 1 &= T_{11}E_S^t(i:P) + T_{13}E_P^t(i:P) \end{aligned}\right\} \tag{142}$$

$$\left.\begin{aligned} E_P^r(i:S) &= T_{11}E_S^t(i:S) + T_{13}E_P^t(i:S) \\ E_P^r(i:P) &= T_{11}E_S^t(i:P) + T_{13}E_P^t(i:P) \end{aligned}\right\}. \tag{143}$$

Each of these sets of equations can be easily rewritten into matrix/vector form and solved trivially.

$$\begin{bmatrix} 1 \\ 0 \end{bmatrix} = \begin{bmatrix} E_S^t(i:S) & E_P^t(i:S) \\ E_S^t(i:P) & E_P^t(i:P) \end{bmatrix} \begin{bmatrix} T_{11} \\ T_{13} \end{bmatrix} \Rightarrow \begin{bmatrix} T_{11} \\ T_{13} \end{bmatrix} = \begin{bmatrix} E_S^t(i:S) & E_P^t(i:S) \\ E_S^t(i:P) & E_P^t(i:P) \end{bmatrix}^{-1} \begin{bmatrix} 1 \\ 0 \end{bmatrix} \tag{144}$$

$$\begin{bmatrix} E_S^r(i:S) \\ E_S^r(i:P) \end{bmatrix} = \begin{bmatrix} E_S^t(i:S) & E_P^t(i:S) \\ E_S^t(i:P) & E_P^t(i:P) \end{bmatrix} \begin{bmatrix} T_{21} \\ T_{23} \end{bmatrix} \Rightarrow \begin{bmatrix} T_{21} \\ T_{23} \end{bmatrix} = \begin{bmatrix} E_S^t(i:S) & E_P^t(i:S) \\ E_S^t(i:P) & E_P^t(i:P) \end{bmatrix}^{-1} \begin{bmatrix} E_S^r(i:S) \\ E_S^r(i:P) \end{bmatrix} \tag{145}$$

$$\begin{bmatrix} 0 \\ 1 \end{bmatrix} = \begin{bmatrix} E_S^t(i:S) & E_P^t(i:S) \\ E_S^t(i:P) & E_P^t(i:P) \end{bmatrix} \begin{bmatrix} T_{31} \\ T_{33} \end{bmatrix} \Rightarrow \begin{bmatrix} T_{31} \\ T_{33} \end{bmatrix} = \begin{bmatrix} E_S^t(i:S) & E_P^t(i:S) \\ E_S^t(i:P) & E_P^t(i:P) \end{bmatrix}^{-1} \begin{bmatrix} 0 \\ 1 \end{bmatrix} \tag{146}$$

$$\begin{bmatrix} E_P^r(i:S) \\ E_P^r(i:P) \end{bmatrix} = \begin{bmatrix} E_S^t(i:S) & E_P^t(i:S) \\ E_S^t(i:P) & E_P^t(i:P) \end{bmatrix} \begin{bmatrix} T_{41} \\ T_{43} \end{bmatrix} \Rightarrow \begin{bmatrix} T_{41} \\ T_{43} \end{bmatrix} = \begin{bmatrix} E_S^t(i:S) & E_P^t(i:S) \\ E_S^t(i:P) & E_P^t(i:P) \end{bmatrix}^{-1} \begin{bmatrix} E_P^r(i:S) \\ E_P^r(i:P) \end{bmatrix} \tag{147}$$

Note that this now introduces a new set of assumptions into the solution. Reformulating these equations in this way forces certain conditions onto the transmitted measurements. The three relevant conditions are

1. $E_S^t(i:S)$ and $E_S^t(i:P)$ cannot both be equal to zero at the same time,
2. $E_P^t(i:S)$ and $E_P^t(i:P)$ cannot both be equal to zero at the same time, and
3. $[E_S^t(i:S), E_P^t(i:S)]$ and $[E_S^t(i:P), E_P^t(i:P)]$ cannot be related by a scalar.

These restrictions are due to the linear algebra necessary to carry out the matrix inversion [89], and carry some interesting physical implications.

In order to satisfy the first two conditions, both experiments must include some transmitted wave. This implies that opaque substrates cannot be used. In simulations, this is not an issue; typically, these simulations are performed with either no substrate, or a non-lossy substrate. This does prevent Perfect Electric Conductors (PEC) from being used as a layer boundary within the simulation, which can be inconvenient in some circumstances. However, the lack of a PEC is irrelevant to this particular research.

The third limitation is slightly more restricting, but easily avoidable. This limitation requires that both experiments generate unique polarization states. If both generated polarization states are the same, the matrix inversion results in a divide-by-zero, which fails to give a solution. This will most commonly occur when one of the polarization states is fully extinguished upon transmission, which occurs at Brewster's angle. This actually implies that Brewster's angle is the one point at which the experiment cannot be preformed, which runs contrary to the most common ellipsometry advice [30]. It only takes a small difference to avoid this effect, which means that angles around Brewster's angle can still be used for the experiment. (Angles around Brewster's angle might still be poor choices, but this would be due to effects such as measurement noise as opposed to the underlying physics.)

Now, after finding the first and third columns of the T matrix, two more experiments can be performed to find the remaining eight elements. The second set of experiments are identical to the first, except that the back-traveling wave will be excited this time. This produces a new set of measurements

$$\left.\begin{array}{ll} E_S^r(b:S) & E_S^r(b:P) \\ E_P^r(b:S) & E_P^r(b:P) \\ E_S^t(b:S) & E_S^t(b:P) \\ E_P^t(b:S) & E_P^t(b:P) \end{array}\right\} . \tag{148}$$

For simplicity, the waves will be defined as they are shown in Figure 31, which means the wave transmitted through the sample will be referenced as the reflected wave, and the wave reflected from the sample will be referred to as the transmitted wave.

In some cases, symmetry may be useful in minimizing the number of necessary simulations. For example, one of the structures examined at the end of this chapter is a tilted nanorod, similar to those studied in Chapter III. This structure exhibits symmetry such that the back-traveling simulation is the same as the forward simulation at $\phi_{\text{back}} = \phi_{\text{forward}} + 180°$, which is shown in Figure 32. This reduces the number of necessary simulations, which can greatly reduce the needed computational time.

Extracting the remaining elements from this new set of measurements is simpler than extracting the first set of eight. Again, the four-by-four matrix method will be used to create a set of equations for extracting the final set of parameters. For S-pol

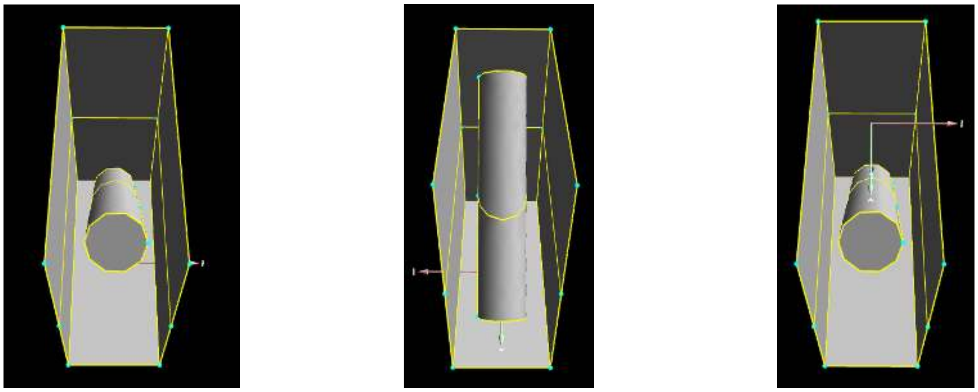

(a) $\phi = 0^\circ$
incident case.

(b) $\phi = 180^\circ$**.**
incident case.

(c) $\phi = 180^\circ$**,**
back-traveling case.

Figure 32. Three different simulations. Note that third experiment is the same as the first due to the symmetry of the layer being modeled.

light incident,

$$\begin{bmatrix} 0 \\ E_S^r(b:S) \\ 0 \\ E_P^r(b:S) \end{bmatrix} = \begin{bmatrix} T_{11} & T_{12} & T_{13} & T_{14} \\ T_{21} & T_{22} & T_{23} & T_{24} \\ T_{31} & T_{32} & T_{33} & T_{34} \\ T_{41} & T_{42} & T_{43} & T_{44} \end{bmatrix} \begin{bmatrix} E_S^t(b:S) \\ 1 \\ E_P^t(b:S) \\ 0 \end{bmatrix}. \tag{149}$$

For P-pol light incident, the equation changes slightly, and uses the second set of measurements:

$$\begin{bmatrix} 0 \\ E_S^r(b:P) \\ 0 \\ E_P^r(b:P) \end{bmatrix} = \begin{bmatrix} T_{11} & T_{12} & T_{13} & T_{14} \\ T_{21} & T_{22} & T_{23} & T_{24} \\ T_{31} & T_{32} & T_{33} & T_{34} \\ T_{41} & T_{42} & T_{43} & T_{44} \end{bmatrix} \begin{bmatrix} E_S^t(b:P) \\ 0 \\ E_P^t(b:P) \\ 1 \end{bmatrix}. \tag{150}$$

Equation (149) can be solved for the second column. A simple rearrangement gives the equation

$$\begin{bmatrix} T_{12} \\ T_{22} \\ T_{32} \\ T_{42} \end{bmatrix} = \begin{bmatrix} -T_{11} & 0 & T_{13} & 0 \\ -T_{21} & 1 & T_{23} & 0 \\ -T_{31} & 0 & T_{33} & 0 \\ -T_{41} & 0 & T_{43} & 1 \end{bmatrix} \begin{bmatrix} E_S^t(b:S) \\ E_S^r(b:S) \\ E_P^t(b:S) \\ E_P^r(b:S) \end{bmatrix}. \tag{151}$$

Similarly, equation (150) gives

$$\begin{bmatrix} T_{14} \\ T_{24} \\ T_{34} \\ T_{44} \end{bmatrix} = \begin{bmatrix} -T_{11} & 0 & T_{13} & 0 \\ -T_{21} & 1 & T_{23} & 0 \\ -T_{31} & 0 & T_{33} & 0 \\ -T_{41} & 0 & T_{43} & 1 \end{bmatrix} \begin{bmatrix} E_S^t(b:P) \\ E_S^r(b:P) \\ E_P^t(b:P) \\ E_P^r(b:P) \end{bmatrix}. \tag{152}$$

Solving these equations, due to their simple linear nature, does not impress any further assumptions onto the problem.

4.3.2 Solving the E fields given the T matrix.

Finding the E fields given the matrix T (detailed in Section 2.3.3) is often necessary. Typically, this is to either compare the simulated and predicted E fields, or for the purposes of calibration, to make sure that the T matrix is being calculated correctly. An error in phase with the incident fields can lead to incorrect matrices being calculated.

The set of assumptions regarding linearity above are used to calculate the fields given the incomplete information present in the system. Each of the vectors in, say, equation (138), are only half populated at the beginning of the calculation. For example, calculating the reflected and transmitted fields for the case where S-pol light is incident results in

$$\begin{bmatrix} 1 \\ E^r_S(i:S) \\ 0 \\ E^r_P(i:S) \end{bmatrix} = \begin{bmatrix} T_{11} & T_{12} & T_{13} & T_{14} \\ T_{21} & T_{22} & T_{23} & T_{24} \\ T_{31} & T_{32} & T_{33} & T_{34} \\ T_{41} & T_{42} & T_{43} & T_{44} \end{bmatrix} \begin{bmatrix} E^t_S(i:S) \\ 0 \\ E^t_P(i:S) \\ 0 \end{bmatrix} \tag{153}$$

where T is now known, and the E fields are the variable to be found.

The linearity assumptions aid in calculating the unknown fields in this equation. The transmitted fields are found first, using the following equation:

$$\begin{bmatrix} 1 \\ 0 \end{bmatrix} = \begin{bmatrix} T_{11} & T_{13} \\ T_{31} & T_{33} \end{bmatrix} \begin{bmatrix} E^t_S(i:S) \\ E^t_P(i:S) \end{bmatrix} \Rightarrow \begin{bmatrix} E^t_S(i:S) \\ E^t_P(i:S) \end{bmatrix} = \begin{bmatrix} T_{11} & T_{13} \\ T_{31} & T_{33} \end{bmatrix}^{-1} \begin{bmatrix} 1 \\ 0 \end{bmatrix}. \tag{154}$$

The conditions regarding invertibility at this stage are similar to the ones given above in Section 4.3.1. These elements of the T matrix relate incident light with the transmitted light. If the transmitted light generated by each state is identical, then this sub-matrix cannot be inverted. Finding the reflected fields after calculating the transmitted fields is trivial.

$$\begin{bmatrix} T_{21} & T_{23} \\ T_{41} & T_{43} \end{bmatrix} \begin{bmatrix} E^t_S(i:S) \\ E^t_P(i:S) \end{bmatrix} = \begin{bmatrix} E^r_S(i:S) \\ E^r_P(i:S) \end{bmatrix}. \tag{155}$$

The complete T matrix can be used instead of the sub-matrix to verify the process; if correct, the top element of the calculated vector will be 1, while the third will be 0.

The same process is used to find the transmitted and reflected fields for the P-pol incident case:

$$\begin{bmatrix} 0 \\ 1 \end{bmatrix} = \begin{bmatrix} T_{11} & T_{13} \\ T_{31} & T_{33} \end{bmatrix} \begin{bmatrix} E_S^t(i:P) \\ E_P^t(i:P) \end{bmatrix} \Rightarrow \begin{bmatrix} E_S^t(i:P) \\ E_P^t(i:P) \end{bmatrix} = \begin{bmatrix} T_{11} & T_{13} \\ T_{31} & T_{33} \end{bmatrix}^{-1} \begin{bmatrix} 0 \\ 1 \end{bmatrix} \tag{156}$$

$$\begin{bmatrix} T_{21} & T_{23} \\ T_{41} & T_{43} \end{bmatrix} \begin{bmatrix} E_S^t(i:P) \\ E_P^t(i:P) \end{bmatrix} = \begin{bmatrix} E_S^r(i:S) \\ E_P^r(i:S) \end{bmatrix}. \tag{157}$$

Determining the fields generated by the back-traveling wave is slightly more difficult. In the case where there is a S-pol back-traveling wave, the problem can be described with the equation

$$\begin{bmatrix} 0 \\ E_S^r(b:S) \\ 0 \\ E_P^r(b:S) \end{bmatrix} = \begin{bmatrix} T_{11} & T_{12} & T_{13} & T_{14} \\ T_{21} & T_{22} & T_{23} & T_{24} \\ T_{31} & T_{32} & T_{33} & T_{34} \\ T_{41} & T_{42} & T_{43} & T_{44} \end{bmatrix} \begin{bmatrix} E_S^t(b:S) \\ 1 \\ E_P^t(b:S) \\ 0 \end{bmatrix}. \tag{158}$$

The number of unknowns in the problem can be reduced from four to two (both transmitted and reflected fields to just transmitted) by removing the calculations necessary for the reflected waves. Written in equation form, equation (158) becomes

$$0 = T_{11}E_S^t(b:S) + T_{12} + T_{13}E_P^t(b:S) \tag{159}$$

$$0 = T_{31}E_S^t(b:S) + T_{32} + T_{33}E_P^t(b:S) \tag{160}$$

or

$$\begin{bmatrix} -T_{12} \\ -T_{32} \end{bmatrix} = \begin{bmatrix} T_{11} & T_{13} \\ T_{31} & T_{33} \end{bmatrix} \begin{bmatrix} E_S^t(b:S) \\ E_P^t(b:S) \end{bmatrix}. \tag{161}$$

Inverting the matrix here is reliant again on the assumptions stated at the beginning of this section. Knowing the transmitted fields, the forward fields are easily found as

$$\begin{bmatrix} E_S^r(b:S) \\ E_P^r(b:S) \end{bmatrix} = \begin{bmatrix} T_{21} & T_{22} & T_{23} \\ T_{41} & T_{42} & T_{43} \end{bmatrix} \begin{bmatrix} E_S^t(b:S) \\ 1 \\ E_P^t(b:S) \end{bmatrix}. \tag{162}$$

The same process gives the following two equations for the back-traveling P-pol wave problem:

$$\begin{bmatrix} -T_{14} \\ -T_{34} \end{bmatrix} = \begin{bmatrix} T_{11} & T_{13} \\ T_{31} & T_{33} \end{bmatrix} \begin{bmatrix} E_S^t(b:P) \\ E_P^t(b:P) \end{bmatrix} \Rightarrow \begin{bmatrix} E_S^t(b:P) \\ E_P^t(b:P) \end{bmatrix} = \begin{bmatrix} T_{11} & T_{13} \\ T_{31} & T_{33} \end{bmatrix}^{-1} \begin{bmatrix} -T_{14} \\ -T_{34} \end{bmatrix}, \tag{163}$$

$$\begin{bmatrix} E_S^r(b:P) \\ E_P^r(b:P) \end{bmatrix} = \begin{bmatrix} T_{21} & T_{23} & T_{24} \\ T_{41} & T_{43} & T_{44} \end{bmatrix} \begin{bmatrix} E_S^t(b:P) \\ E_P^t(b:P) \\ 1 \end{bmatrix}. \tag{164}$$

These equations along with the equations in the preceding section show that the relationship between the E fields and the T matrix is an invertible one. This stands in contrast with the equations used to relate the T matrix with those of the ellipsometric angles, which is strictly non-invertible. The proof of this is simple: there are twelve ellipsometric angles, which are combined to create six complex reflection and transmission coefficients. There is no way to recover even eight elements of the T matrix given only six numbers. Using the E fields instead, which is at present only possible in simulations, gives much more information, and allows for the remainder of this process.

4.4 Converting from T matrix to Δ_B

While the T matrix contains all of the information about how light propagates through a structure, it tells nothing of the relevant properties, such as permittivity or layer thickness. Measuring the T matrix gives no new information about the problem. However, the T matrix is a function of the material properties such as permittivity and layer thickness. Therefore, these quantities of interest can be extracted from the measured T matrix.

The general process of the parameter extraction is the same as in ellipsometry, only in reverse. The T matrix is equal to

$$T = L_i T_\Pi L_t^{-1} = L_i \prod_{p=1}^{N_P} T_p L_t^{-1} \tag{165}$$

where N_P is the total number of layers. The first and last matrices in this equation are simple projection matrices given by Equations (88) and (89). Now, if the partial projection matrix is used, then the inside product cannot be determined; the partial projection matrix removes half of the information necessary to find the inside product. However, the full projection matrix (which is the partial projection matrix with the addition of the back-traveling wave) is fully invertible. Therefore,

$$T_\Pi = L_i^{-1} T L_t. \tag{166}$$

Both projection matrices are found using information known about the experiment, specifically the angle of incidence and the index of the incident and transmitted material.

If the experiment has only a single layer, then T_Π is the matrix of interest. If there are multiple layers present, for example a metamaterial on top of a known substrate, then some additional matrix math must take place in order to isolate the layer of interest. These extra layers can be easily accounted for, but only if they are composed of known materials. In general, this is the case; a substrate is typically a simple homogenous layer of known thickness.

The T_p matrix of a single unknown layer (shown here as T_1) can be found in the following fashion:

$$T_\Pi = \prod_{p=1}^{N_P} T_p = T_1 \prod_{p=2}^{N_P} T_p \tag{167}$$

therefore

$$T_1 = T_\Pi \prod_{p=2}^{N_P} (T_p)^{-1} \tag{168}$$

where T_Π is the calculated product found in (166), and T_p inside the product is the T_p matrix of the individual known layers present in the problem. These are calculated straightforwardly from the known layer thicknesses and permittivities using equations (92) and (93).

But are each of these matrices invertible? The answer is yes. The invertible matrix theorem gives us that if the determinate of a matrix is not equal to zero, the matrix must be invertible. So, what is the determinate of the matrix T_p? The matrix T_p was defined as

$$T_p = \exp\left(-i\frac{c}{\omega}\Delta_B d\right). \tag{169}$$

The determinate of T_p is then

$$\begin{aligned}\det(T_p) &= \det\left(\exp\left[-i\frac{2\pi}{\lambda_0}\Delta_B d\right]\right)\\ &= \exp\left(\mathrm{Tr}\left[-i\frac{2\pi}{\lambda_0}\Delta_B d\right]\right)\\ &= \exp\left(-i\frac{2\pi}{\lambda_0}\mathrm{Tr}\left[\Delta_B\right] d\right)\end{aligned} \tag{170}$$

where Tr denotes the trace operator. Since the determinant of the matrix is equal to the exponential of a complex number, there is no way for the determinant to be equal to zero. Therefore, the matrix T_p is always invertible.

Once the unknown matrix T_p is found, the next step in the process is to determine the value of the matrix Δ_B. In general, the layer thickness is known, or can be easily assumed from the problem. The layer depth is chosen to be a convenient value. (This process can be repeated where d is an unknown value that is found or assumed at the very end of the extraction process, but this shows that d is a value that simply scales the extracted values. In essence, d compresses the permittivity and permeability tensors, which ultimately leads back to the same optical properties.) In other words, it is seen that the effective thickness is almost exactly the same as the assumed thickness, so the thickness is assumed in this derivation.

Equation (169) gives the relationship between T_p and Δ_B. This gives the matrix Δ_B as

$$\begin{aligned}\Delta_B &= i\frac{c}{\omega d}\mathrm{ixp}(T_p) &(171)\\ &= i\frac{c}{\omega d}\mathrm{ixp}\left(L_i^{-1}TL_t\right) &(172)\end{aligned}$$

where ixp() is a function which inverts the exponential. Some of the time, this function is equal to the natural-log function. This is covered in depth in the next Chapter V. The function will be assumed to have the property

$$\mathrm{ixp}\left(\exp A\right) = A, \tag{173}$$

for every square matrix A. This property not shared with the ln() function. The physics of the application here allows for the assumption of this particular property within this particular problem, but this property cannot be generally assumed.

This matrix describes how light propagates through a layer, but again gives little information about the quantities of interest. However, there is an underlying structure to this matrix, which allow for the extraction of these parameters.

4.5 Structure of Δ_B

Section 2.3.3 previously covered the structure of Δ_B. For a non-magnetic anisotropic material, Schmidt [79] gives this matrix as

$$\Delta_B = \begin{bmatrix} -K_{xx}\frac{\epsilon_{zx}}{\epsilon_{zz}} & -K_{xx}\frac{\epsilon_{zy}}{\epsilon_{zz}} & 0 & 1-\frac{K_{xx}^2}{\epsilon_{zz}} \\ 0 & 0 & -1 & 0 \\ \epsilon_{yz}\frac{\epsilon_{zx}}{\epsilon_{zz}} - \epsilon_{yx} & K_{xx}^2 - \epsilon_{yy} + \epsilon_{yz}\frac{\epsilon_{zy}}{\epsilon_{zz}} & 0 & K_{xx}\frac{\epsilon_{yz}}{\epsilon_{zz}} \\ \epsilon_{xx} - \epsilon_{xz}\frac{\epsilon_{zx}}{\epsilon_{zz}} & \epsilon_{xy} - \epsilon_{xz}\frac{\epsilon_{zy}}{\epsilon_{zz}} & 0 & -K_{xx}\frac{\epsilon_{xz}}{\epsilon_{zz}} \end{bmatrix}, \tag{174}$$

where K_{xx} is defined as $n_i \sin\theta_i$, and the ϵ variables are taken from the permittivity tensor

$$\epsilon = \begin{bmatrix} \epsilon_{xx} & \epsilon_{xy} & \epsilon_{xz} \\ \epsilon_{yx} & \epsilon_{yy} & \epsilon_{yz} \\ \epsilon_{zx} & \epsilon_{zy} & \epsilon_{zz} \end{bmatrix}. \tag{175}$$

His work was derived from an earlier work by Berreman [15]. Berreman solved for the propagation of a plane wave through a layer with arbitrary permittivity, permeability, and optical-rotation terms. The matrix Δ_B when:

1. permittivity is some arbitrary tensor $\boldsymbol{\epsilon}$;
2. permeability is some arbitrary tensor $\boldsymbol{\mu}$;
3. both optical-rotation tensors are equal to zero;

is

$$\Delta_B = \begin{bmatrix} -K_{xx}\dfrac{\epsilon_{zx}}{\epsilon_{zz}} & K_{xx}\left[\dfrac{\mu_{yz}}{\mu_{zz}} - \dfrac{\epsilon_{zy}}{\epsilon_{zz}}\right] & \mu_{yx} - \dfrac{\mu_{yz}\mu_{zx}}{\mu_{zz}} & \mu_{yy} - \dfrac{\mu_{yz}\mu_{zy}}{\mu_{zz}} - \dfrac{K_{xx}^2}{\epsilon_{zz}} \\ 0 & -K_{xx}\dfrac{\mu_{xz}}{\mu_{zz}} & \dfrac{\mu_{xz}\mu_{zx}}{\mu_{zz}} - \mu_{xx} & \dfrac{\mu_{xz}\mu_{zy}}{\mu_{zz}} - \mu_{xy} \\ \dfrac{\epsilon_{yz}\epsilon_{zx}}{\epsilon_{zz}} - \epsilon_{yx} & \dfrac{K_{xx}^2}{\mu_{zz}} + \dfrac{\epsilon_{yz}\epsilon_{zy}}{\epsilon_{zz}} - \epsilon_{yy} & -K_{xx}\dfrac{\mu_{zx}}{\mu_{zz}} & K_{xx}\left[\dfrac{\epsilon_{yz}}{\epsilon_{zz}} - \dfrac{\mu_{zy}}{\mu_{zz}}\right] \\ \epsilon_{xx} - \dfrac{\epsilon_{xz}\epsilon_{zx}}{\epsilon_{zz}} & \epsilon_{xy} - \dfrac{\epsilon_{xz}\epsilon_{zy}}{\epsilon_{zz}} & 0 & -K_{xx}\dfrac{\epsilon_{xz}}{\epsilon_{zz}} \end{bmatrix} \tag{176}$$

where

$$\boldsymbol{\epsilon} = \begin{bmatrix} \epsilon_{xx} & \epsilon_{xy} & \epsilon_{xz} \\ \epsilon_{yx} & \epsilon_{yy} & \epsilon_{yz} \\ \epsilon_{zx} & \epsilon_{zy} & \epsilon_{zz} \end{bmatrix} \quad \text{and} \quad \boldsymbol{\mu} = \begin{bmatrix} \mu_{xx} & \mu_{xy} & \mu_{xz} \\ \mu_{yx} & \mu_{yy} & \mu_{yz} \\ \mu_{zx} & \mu_{zy} & \mu_{zz} \end{bmatrix}. \tag{177}$$

4.6 Extracting the Permittivity and Permeability

Extracting the permittivity when $\boldsymbol{\mu}$ is the identity matrix is fairly straightforward. The zz element of the permittivity tensor is easily found from the Δ_{14} element of Equation (174):

$$\epsilon_{zz} = \frac{K_{xx}^2}{1 - \Delta_{14}}. \tag{178}$$

The elements containing z can be found using the top and right edge of the Δ_B matrix.

$$\epsilon_{xz} = -\Delta_{44}\frac{\epsilon_{zz}}{K_{xx}} \tag{179}$$

$$\epsilon_{yz} = \Delta_{34}\frac{\epsilon_{zz}}{K_{xx}} \tag{180}$$

$$\epsilon_{zx} = -\Delta_{11}\frac{\epsilon_{zz}}{K_{xx}} \tag{181}$$

$$\epsilon_{zy} = -\Delta_{12}\frac{\epsilon_{zz}}{K_{xx}} \tag{182}$$

The remaining components of the tensor can then be found in the lower-left quadrant.

$$\epsilon_{xx} = \frac{\epsilon_{xz}\epsilon_{zx}}{\epsilon_{zz}} + \Delta_{41} \tag{183}$$

$$\epsilon_{xy} = \frac{\epsilon_{xz}\epsilon_{zy}}{\epsilon_{zz}} + \Delta_{42} \tag{184}$$

$$\epsilon_{yx} = \frac{\epsilon_{yz}\epsilon_{zx}}{\epsilon_{zz}} - \Delta_{31} \tag{185}$$

$$\epsilon_{yy} = K_{xx}^2 + \frac{\epsilon_{yz}\epsilon_{zy}}{\epsilon_{zz}} - \Delta_{32} \tag{186}$$

Extracting both the permittivity and permeability simultaneously is more difficult. One of the first difficulties encountered is the fact that it is an under-defined problem. The Δ_B matrix has 14 non-zero elements, and the problem has 18 unknowns. This implies that some other assumption would be needed to solve the problem. An example of one such assumption might be assuming some kind of symmetry in both of the tensors. However, by taking a second set of measurements and determining 28 non-zero values, all of the 18 parameters can be extracted unambiguously. Most can be found in two different methods.

The Δ_B matrix used up until now will now be referred to as $\Delta^{(xx)}$. This is the Δ_B matrix measured at some sample rotation, not necessarily $\phi^{(xx)} = 0$. Let there be a second measurement at the initial sample rotation plus 90 degrees. This will give a new T matrix, and therefore a new Δ_B matrix, denoted $\Delta^{(xy)}$.

This is a new simulation. Because the sample rotation has been changed, there is a new permittivity and permeability matrix. Havrilla [36] shows that given some rotation matrix A, the new rotated tensor is given by

$$\boldsymbol{\epsilon}_R = R\boldsymbol{\epsilon}R^{-1} \quad \text{and} \quad \boldsymbol{\mu}_R = R\boldsymbol{\mu}R^{-1}. \tag{187}$$

Since the sample rotation about $\hat{z}$ was changed by 90 degrees,

$$R = \begin{bmatrix} 0 & -1 & 0 \\ 1 & 0 & 0 \\ 0 & 0 & 1 \end{bmatrix}. \tag{188}$$

This means that the second experiment will have the tensors

$$\boldsymbol{\epsilon}^{(xy)} = \begin{bmatrix} \epsilon_{yy} & -\epsilon_{yx} & -\epsilon_{yz} \\ -\epsilon_{xy} & \epsilon_{xx} & \epsilon_{xz} \\ -\epsilon_{zy} & \epsilon_{zx} & \epsilon_{zz} \end{bmatrix} \quad \text{and} \quad \boldsymbol{\mu}^{(xy)} = \begin{bmatrix} \mu_{yy} & -\mu_{yx} & -\mu_{yz} \\ -\mu_{xy} & \mu_{xx} & \mu_{xz} \\ -\mu_{zy} & \mu_{zx} & \mu_{zz} \end{bmatrix}, \tag{189}$$

which gives a slightly different form to the matrix $\Delta^{(xy)}$:

$$\Delta^{(xy)} = \begin{bmatrix} K_{yy}\dfrac{\epsilon_{zy}}{\epsilon_{zz}} & K_{yy}\left[\dfrac{\mu_{xz}}{\mu_{zz}} - \dfrac{\epsilon_{zx}}{\epsilon_{zz}}\right] & \dfrac{\mu_{xz}\mu_{zy}}{\mu_{zz}} - \mu_{xy} & \mu_{xx} - \dfrac{\mu_{xz}\mu_{zx}}{\mu_{zz}} - \dfrac{K_{yy}^2}{\epsilon_{zz}} \\ 0 & K_{yy}\dfrac{\mu_{yz}}{\mu_{zz}} & \dfrac{\mu_{yz}\mu_{zy}}{\mu_{zz}} - \mu_{yy} & \mu_{yx} - \dfrac{\mu_{yz}\mu_{zx}}{\mu_{zz}} \\ \epsilon_{xy} - \dfrac{\epsilon_{xz}\epsilon_{zy}}{\epsilon_{zz}} & \dfrac{K_{yy}^2}{\mu_{zz}} + \dfrac{\epsilon_{xz}\epsilon_{zx}}{\epsilon_{zz}} - \epsilon_{xx} & K_{yy}\dfrac{\mu_{zy}}{\mu_{zz}} & K_{yy}\left[\dfrac{\epsilon_{xz}}{\epsilon_{zz}} - \dfrac{\mu_{zx}}{\mu_{zz}}\right] \\ \epsilon_{yy} - \dfrac{\epsilon_{yz}\epsilon_{zy}}{\epsilon_{zz}} & \dfrac{\epsilon_{yz}\epsilon_{zx}}{\epsilon_{zz}} - \epsilon_{yx} & 0 & K_{yy}\dfrac{\epsilon_{yz}}{\epsilon_{zz}} \end{bmatrix} \tag{190}$$

where $K_{yy} = n_i \sin\theta_i^{(xy)}$. The angle of the measurement does not need to be the same as the (xx) case; however, it will be assumed to be identical. Throughout the rest of this document, it will be assumed that $K_{yy} = K_{xx}$.

The first elements extracted are the zz elements. Using the equations

$$\Delta_{14}^{(xx)} + \Delta_{23}^{(xy)} = \mu_{yy} - \frac{\mu_{yz}\mu_{zy}}{\mu_{zz}} - \frac{K_{xx}^2}{\epsilon_{zz}} + \frac{\mu_{yz}\mu_{zy}}{\mu_{zz}} - \mu_{yy} \tag{191}$$

$$\Delta_{32}^{(xx)} + \Delta_{41}^{(xy)} = \frac{K_{xx}^2}{\mu_{zz}} + \frac{\epsilon_{yz}\epsilon_{zy}}{\epsilon_{zz}} - \epsilon_{yy} + \epsilon_{yy} - \frac{\epsilon_{yz}\epsilon_{zy}}{\epsilon_{zz}}, \tag{192}$$

ϵ_{zz} and μ_{zz} can be found as

$$\epsilon_{zz} = \frac{-K_{xx}^2}{\Delta_{14}^{(xx)} + \Delta_{23}^{(xy)}}. \tag{193}$$

$$\mu_{zz} = \frac{K_{xx}^2}{\Delta_{32}^{(xx)} + \Delta_{41}^{(xy)}}. \tag{194}$$

Following this come the xz, yz, zx, and zy elements:

$$\epsilon_{xz} = -\Delta_{44}^{(xx)} \frac{\epsilon_{zz}}{K_{xx}} \tag{195}$$

$$\epsilon_{yz} = \Delta_{44}^{(xy)} \frac{\epsilon_{zz}}{K_{xx}} \tag{196}$$

$$\epsilon_{zx} = -\Delta_{11}^{(xx)} \frac{\epsilon_{zz}}{K_{xx}} \tag{197}$$

$$\epsilon_{zy} = \Delta_{11}^{(xy)} \frac{\epsilon_{zz}}{K_{xx}} \tag{198}$$

$$\mu_{zx} = -\Delta_{33}^{(xx)} \frac{\mu_{zz}}{K_{xx}} \tag{199}$$

$$\mu_{zy} = \Delta_{33}^{(xy)} \frac{\mu_{zz}}{K_{xx}} \tag{200}$$

$$\mu_{xz} = -\Delta_{22}^{(xx)} \frac{\mu_{zz}}{K_{xx}} \tag{201}$$

$$\mu_{yz} = \Delta_{22}^{(xy)} \frac{\mu_{zz}}{K_{xx}} \tag{202}$$

The final four scaled elements can be found knowing the previously extracted values.

$$\epsilon_{xx} = \frac{\epsilon_{xz}\epsilon_{zx}}{\epsilon_{zz}} + \Delta_{41}^{(xx)} \tag{203}$$

$$\epsilon_{xy} = \frac{\epsilon_{xz}\epsilon_{zy}}{\epsilon_{zz}} + \Delta_{42}^{(xx)} \tag{204}$$

$$\epsilon_{yx} = \frac{\epsilon_{yz}\epsilon_{zx}}{\epsilon_{zz}} - \Delta_{31}^{(xx)} \tag{205}$$

$$\epsilon_{yy} = \frac{K_{xx}^2}{\mu_{zz}} + \frac{\epsilon_{yz}\epsilon_{zy}}{\epsilon_{zz}} - \Delta_{32}^{(xx)} \tag{206}$$

$$\mu_{xx} = \frac{\mu_{xz}\mu_{zx}}{\mu_{zz}} - \Delta_{23}^{(xx)} \tag{207}$$

$$\mu_{xy} = \frac{\mu_{xz}\mu_{xy}}{\mu_{zz}} - \Delta_{24}^{(xx)} \tag{208}$$

$$\mu_{yx} = \frac{\mu_{yz}\mu_{zx}}{\mu_{zz}} + \Delta_{13}^{(xx)} \tag{209}$$

$$\mu_{yy} = \frac{\mu_{yz}\mu_{zy}}{\mu_{zz}} + \frac{K_{xx}^2}{\epsilon_{zz}} + \Delta_{14}^{(xx)} \tag{210}$$

This gives all 18 elements of the permittivity and permeability tensors unambiguously.

Note that the same values can be found using the $\Delta^{(xy)}$ instead of the $\Delta^{(xx)}$. For instance, using the relationship

$$\Delta_{14}^{(xy)} + \Delta_{23}^{(xx)} = \mu_{yy} - \frac{\mu_{yz}\mu_{zy}}{\mu_{zz}} - \frac{K_{xx}^2}{\epsilon_{zz}} - \mu_{yy} + \frac{\mu_{yz}\mu_{zy}}{\mu_{zz}}, \tag{211}$$

ϵ_{zz} can be found as

$$\epsilon_{zz} = \frac{-K_{xx}^2}{\Delta_{14}^{(xy)} + \Delta_{23}^{(xx)}}. \tag{212}$$

This allows for the determination of ϵ_{zz} from $\Delta_{14}^{(xy)}$ and $\Delta_{23}^{(xx)}$, as opposed to $\Delta_{14}^{(xx)}$ $\Delta_{23}^{(xy)}$. This gives a slightly different set of equations for determining the remaining elements of the tensors.

$$\mu_{zz} = \frac{K_{xx}^2}{\Delta_{32}^{(xy)} + \Delta_{41}^{(xx)}}. \tag{213}$$

The xz, yz, zx and zy equations remain the same:

$$\epsilon_{xz} = -\Delta_{44}^{(xx)} \frac{\epsilon_{zz}}{K_{xx}} \tag{214}$$

$$\epsilon_{yz} = \Delta_{44}^{(xy)} \frac{\epsilon_{zz}}{K_{xx}} \tag{215}$$

$$\epsilon_{zx} = -\Delta_{11}^{(xx)} \frac{\epsilon_{zz}}{K_{xx}} \tag{216}$$

$$\epsilon_{zy} = \Delta_{11}^{(xy)} \frac{\epsilon_{zz}}{K_{xx}} \tag{217}$$

$$\mu_{zx} = -\Delta_{33}^{(xx)} \frac{\mu_{zz}}{K_{xx}} \tag{218}$$

$$\mu_{zy} = \Delta_{33}^{(xy)} \frac{\mu_{zz}}{K_{xx}} \tag{219}$$

$$\mu_{xz} = -\Delta_{22}^{(xx)} \frac{\mu_{zz}}{K_{xx}} \tag{220}$$

$$\mu_{yz} = \Delta_{22}^{(xy)} \frac{\mu_{zz}}{K_{xx}} \tag{221}$$

The remaining elements are exclusively found from the $\Delta^{(xy)}$ matrix:

$$\epsilon_{xx} = \frac{K_{xx}^2}{\mu_{zz}} + \frac{\epsilon_{xz}\epsilon_{zx}}{\epsilon_{zz}} - \Delta_{32}^{(xy)} \tag{222}$$

$$\epsilon_{xy} = \frac{\epsilon_{xz}\epsilon_{zy}}{\epsilon_{zz}} + \Delta_{31}^{(xy)} \tag{223}$$

$$\epsilon_{yx} = \frac{\epsilon_{yz}\epsilon_{zx}}{\epsilon_{zz}} - \Delta_{42}^{(xy)} \tag{224}$$

$$\epsilon_{yy} = \frac{\epsilon_{yz}\epsilon_{zy}}{\epsilon_{zz}} + \Delta_{41}^{(xy)} \tag{225}$$

$$\mu_{xx} = \frac{K_{xx}^2}{\epsilon_{zz}} + \frac{\mu_{xz}\mu_{zx}}{\mu_{zz}} + \Delta_{14}^{(xy)} \tag{226}$$

$$\mu_{xy} = \frac{\mu_{xz}\mu_{xy}}{\mu_{zz}} - \Delta_{13}^{(xy)} \tag{227}$$

$$\mu_{yx} = \frac{\mu_{yz}\mu_{zx}}{\mu_{zz}} + \Delta_{24}^{(xx)} \tag{228}$$

$$\mu_{yy} = \frac{\mu_{yz}\mu_{zy}}{\mu_{zz}} - \Delta_{14}^{(xx)} \tag{229}$$

This alternate set of equations can be used to check the validity of the extracted parameters, or can be averaged with the other set of extracted values to increase accuracy. In general, the first set of equations is perfectly accurate at $\phi = 0$ and has some error at $\phi = 90$ degrees, while the second is perfectly accurate at $\phi = 90$ degrees and has some error at $\phi = 0$. Averaging the two sets results in a lower average error.

4.7 Simulations

4.7.1 FLO_K.

The following simulations were performed using the software FLO_K . FLO_K is a finite-element-method-based computational electromagnetics solver, developed as an offshoot of the SENTRi software under the CREATE program [6], and designed for analyzing periodic structures. The software using a floquet-based set of equations to calculate complex reflection and transmission coefficients for periodic structures. It is capable of solving for the coefficients of multiple grating orders, but only the (0,0) orders (specular reflection and transmission) are needed for the following analyses. Meshes are generated using the CAPSTONE software, also part of the CREATE program.

4.7.2 Plane with known permittivity.

The first material examined here will be a plane of known thickness with a defined permittivity. This provides the most obvious common-sense check against the extraction technique, and provides some valuable insights into noise characteristics and ideal operating parameters.

In this simulation, an isotropic plane of a known permittivity is illuminated with a planewave with an angle of incidence of 10 degrees from normal. The light is a single frequency for each simulation, and the complex reflection and transmission coefficients are recorded at each wavelength. Since this material is an isotropic plane, the Fresnel equations can be used to calculate the correct reflection and transmission coefficients, which can be compared with the FLO_K results.

The equations needed to predict the reflection and transmission coefficients of a planar slab can be found in Born and Wolf [19]. They give the complex reflection r and transmission coefficients t as

$$r = \frac{r_{12} + r_{23}\exp(2i\beta)}{1 + r_{12}r_{23}\exp(2i\beta)} \tag{230}$$

$$t = \frac{t_{12}t_{23}\exp(i\beta)}{1 + r_{12}r_{23}\exp(2i\beta)} \tag{231}$$

where

$$r_{12}^s = \frac{n_s \cos\theta_i - n_i \cos\theta_s}{n_s \cos\theta_i + n_i \cos\theta_s} \tag{232}$$

$$r_{23}^s = \frac{n_i \cos\theta_s - n_s \cos\theta_i}{n_i \cos\theta_s + n_s \cos\theta_i} \tag{233}$$

$$t_{12}^s = \frac{2n_i \cos\theta_i}{n_i \cos\theta_i + n_s \cos\theta_s} \tag{234}$$

$$t_{23}^s = \frac{2n_s \cos\theta_s}{n_s \cos\theta_s + n_i \cos\theta_i} \tag{235}$$

for the S-pol case, and

$$r_{12}^p = \frac{n_i \cos\theta_i - n_s \cos\theta_s}{n_i \cos\theta_i + n_s \cos\theta_s} \tag{236}$$

$$r_{23}^p = \frac{n_s \cos\theta_s - n_i \cos\theta_i}{n_s \cos\theta_s + n_i \cos\theta_i} \tag{237}$$

$$t_{12}^p = \frac{2n_i \cos\theta_i}{n_s \cos\theta_i + n_i \cos\theta_s} \tag{238}$$

$$t_{23}^p = \frac{2n_s \cos\theta_s}{n_i \cos\theta_s + n_s \cos\theta_i} \tag{239}$$

for the P-pol case. For both cases,

$$\beta = \frac{\omega}{c} n_s d \cos\theta_s. \tag{240}$$

For the equations above, n_i is the incident and terminating medium, n_s is the medium of the planar slab (the permittivity is shown in Figure 33), θ_i is the angle of incidence in the incident medium, and θ_s is the angle of propagation within the slab. d is the thickness of the slab, which is 100 nanometers. FLO_K returns the amplitude and phase, which is easily found from the coefficients as the absolute value of r and t, or the angle of r and t. The comparison of the amplitudes is shown in Figure 34, which also contains the residual difference between the equations and FLO_K .

Figure 34 shows that there is very good agreement between the results of the slab

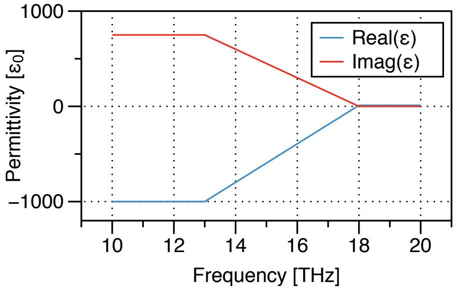

Figure 33. Slab permittivity. The permeability of the slab is $\mu = 1$.

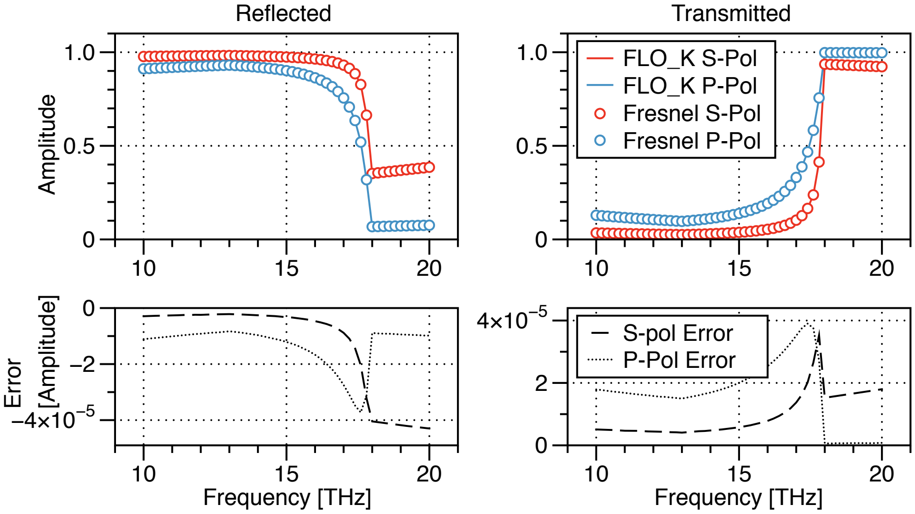

Figure 34. (Top) Compared reflection and transmission amplitudes for FLO_K and Fresnel equation. The residual difference between the Fresnel prediction and FLO_K simulation is shown at the bottom. $\theta = 60$ degrees.

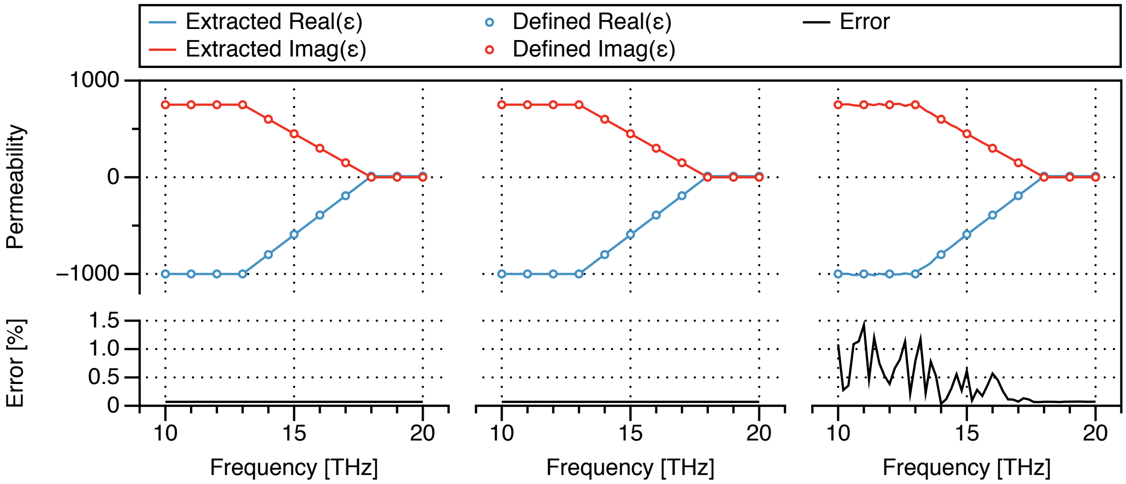

Figure 35. (Top) Extracted permittivity tensor elements for high-to-low transition material. $\theta = 60$ degrees. The relative error for each element is shown on the bottom.

modeled with FLO_K , and one modeled using Fresnel's equations applied to a thin slab. There is a relative error of approximately $10^{-3}\%$ across the frequency spectrum simulated here. This difference is slightly above the noise floor of the simulator (data output is truncated to nearest 10^{-7}). Even so, it shows that the FLO_K software does a great job at predicting the behavior of the plane.

Knowing that the reflection and transmission coefficients are reasonably accurate, the next step is to use this data to extract the permittivities of the slab and compare them to the known values. The fields are used to calculate the T matrix, which is easily converted to T_p. The matrix is then processed to calculate the matrix Δ_B, which is used to calculate the permittivity and permeability of the planar slab. The extracted permittivities and associated error is shown in Figure 35.

This simulation goes to show that there is some error present in the extraction process when the permittivity of the material is high; there is a clear decrease in error as the permittivity drops towards $\epsilon = 11$. A simulation where the high and low permittivity are swapped show that the error is clearly associated solely with the higher permittivity. The extracted permittivity is shown in Figure 36. A third

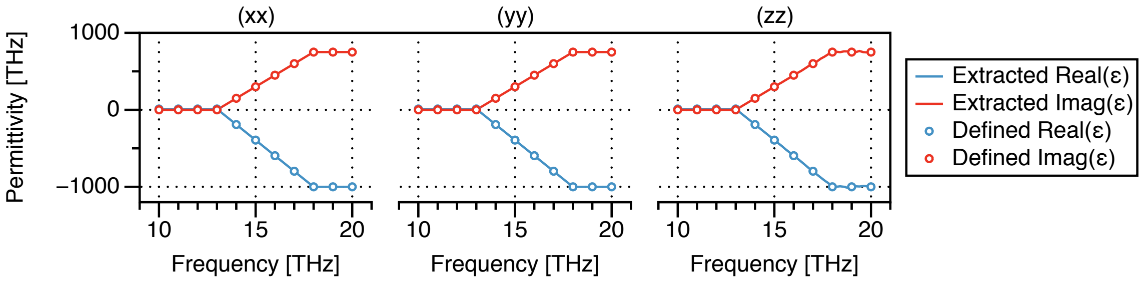

Figure 36. Extracted permittivity tensor elements for low-to-high transition material. $\theta = 60$ degrees. The relative error is similar to Fig. 35, in that the relative error is highest when the permittivity is high.

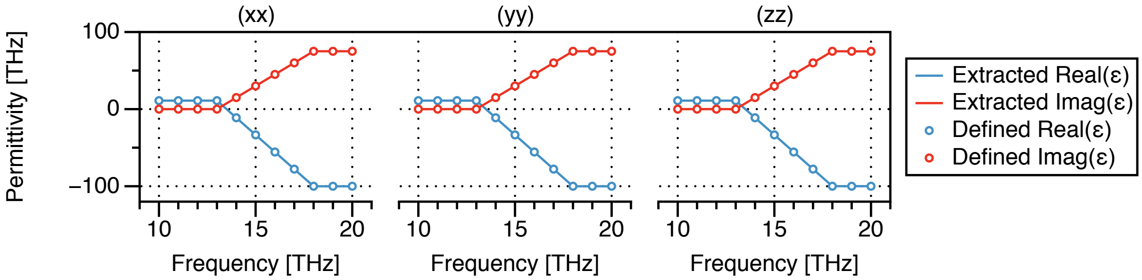

Figure 37. Extracted permittivity tensor elements for low-to-high transition material with lower peak permittivity than Figure 36. $\theta = 60$ degrees. The relative error of ϵ_{zz} is very low ($< 0.5\%$) throughout the range of frequencies.

simulation was done where the high permittivity was a factor of ten lower (-100+75i). This is shown in Figure 37, and has much lower noise than the higher index simulations ($< 0.5\%$ over the frequency range).

It should be noted that the angle of incidence plays a part in the error of the extracted permittivity. Another simulation was carried out with the same permittivities, but where the angle of incidence was $\theta = 10$ degrees. This is shown in Figure 38. This simulation showed much higher noise than the simulation at $\theta = 60$ degrees. One possible explanation of this phenomenon is due to the fact that during extraction, K_{xx}^2/ϵ_{zz} is calculated. The overall signal of this term decreases with the angle of incidence, which could make simulation noise more significant. However, the noise decreases significantly with the overall permittivity; a permittivity of $\epsilon = -1000 + 750i$ is an order of magnitude higher than many of the other materials examined in this

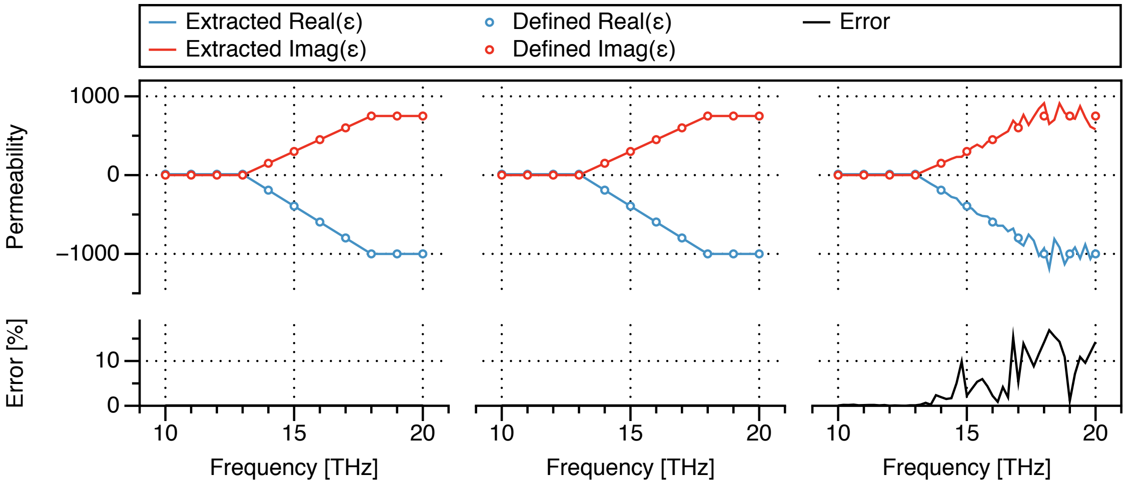

Figure 38. Extracted permittivity tensor elements (top) for low-to-high transition material. $\theta = 10$ degrees. The error (bottom) is much higher at the higher permittivities due to the higher angle of incidence.

chapter.

All of this goes to show that this extraction methodology can determine the permittivity of an isotropic slab fairly accurately under most circumstances. Some care must be taken in situations where the permittivity is high or at angles closer to normal incidence, but overall the process is fairly robust in this simple case.

4.7.3 Aligned anisotropic medium.

The aligned anisotropic structure examined here was taken from the research of Alex Knisley, who recently graduated from AFIT with a Master's degree from the Department of Electrical and Computer Engineering. His research had been focused on studying the effective permittivities of aligned anisotropic structures within microwave waveguides. One of the structures he studied was a slab with air inclusions which permeated the length of the structure. The size of the inclusion was chosen to introduce certain resonant features, which cause spectral features to occur in the permittivity and permeability of the structure. His research ties in particularly well with what has been presented in this document, as he used traditional techniques to

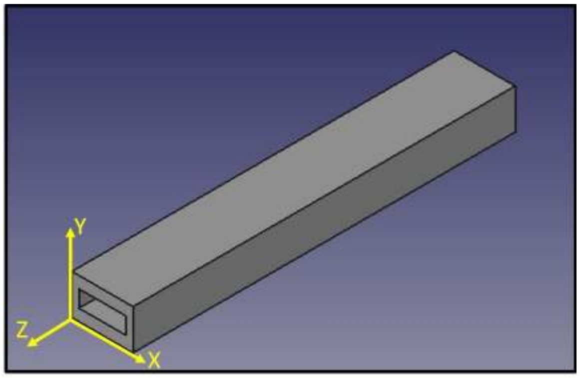

Figure 39. Aligned anisotropic medium scene. The unit cell has dimensions 3.66 millimeters in $\hat{x}$, and 2.39 millimeters in $\hat{y}$. The cell is 22.86 millimeters long in the $\hat{z}$ direction. The inclusion has dimensions 2.79 millimeters wide in $\hat{x}$, 1 millimeters wide in $\hat{y}$, and spans the length of the unit cell.

extract the xx and yy elements of the tensors, which can be directly compared to those of the PPTE technique.

The geometry of this particular structure is fairly simple. Note that this is a structure which is designed for a microwave waveguide, hence the use of millimeter-sized structures. The unit-cell has dimensions 3.66 millimeters in $\hat{x}$ and 2.39 millimeters in $\hat{y}$, and has a depth of 22.86 millimeters. The inclusion has a width of 2.79 millimeters in $\hat{x}$ and 1 millimeters in $\hat{y}$, and spans the length of the cell. A picture of the structure is shown in Figure 39. The permittivity of the slab is defined as $\epsilon = 2.86 + 0.04i$, and is held constant over the frequency range simulated here. The inclusion has the permittivity of free space.

Knisley used the 2-D Newton root search method to form the Nicolson-Ross-Weir material parameter extraction equations [83]. This technique finds the relative permittivity and permeability values for the xx and yy tensor elements from the normal reflection and transmission values. The reflection and transmission coefficients were calculated using FLO_K for frequencies ranging from 8.2 GHz to 12.4 GHz, which covers the X-band. Knisley notes that the permittivity and permeability demonstrates unique transverse permittivities and exhibits half-wavelength resonances around 9

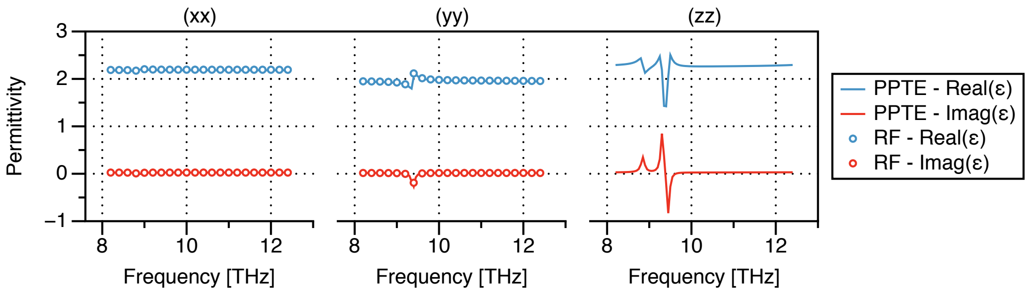

Figure 40. Extracted diagonal elements of the permittivity tensor for the aligned anisotropic medium (RF refers to Root-Finding results). The off-diagonal elements all have amplitudes less than 1e-8.

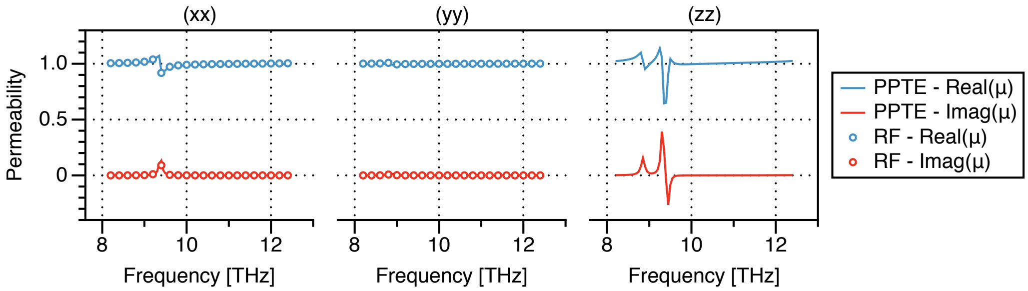

Figure 41. Extracted diagonal elements of the permeability tensor for the aligned anisotropic medium (RF refers to Root-Finding results). The off-diagonal elements all have amplitudes less than 1e-12.

GHz. The 9 GHz resonance is especially important, as it is the most obvious spectral feature occurring over the wavelength range in question. The extracted permittivity and permeability are shown in Figures 40 and 41 as the "Root Finding" result.

The PPTE extraction technique requires off-normal reflection and transmission coefficients, so an incidence angle of 5 degrees was chosen for these simulations. The same frequencies were used. Two simulations are performed at 0° and 90° to calculate the $\Delta^{(xx)}$ and $\Delta^{(xy)}$ information. (Note that the symmetries of the problem cause the forward case to be the same as the back-traveling case.) The permittivities and permeabilities extracted using PPTE aligned excellently with those found in Knisley's work. The xx, yy, and zz tensor elements can be seen in Figures 40 and 41 as the "PPTE" result. Note that zz element shows substantial activity, which is not observed using the Root Finding technique.

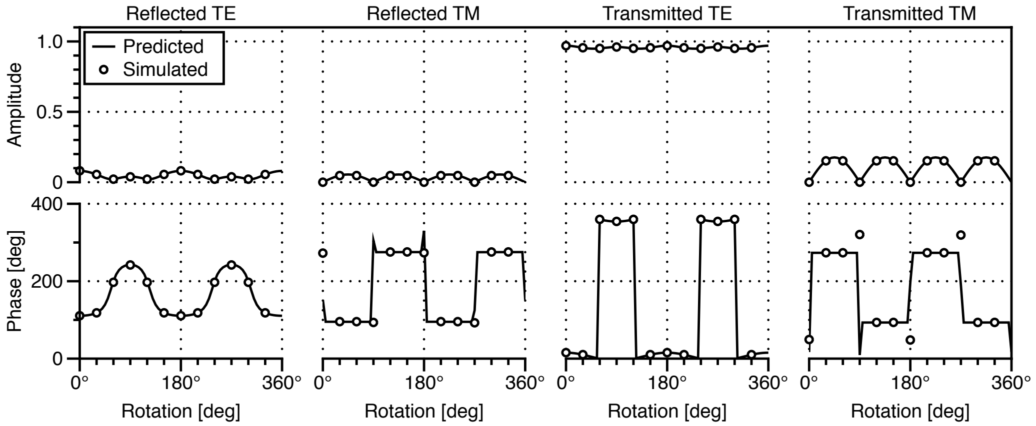

Figure 42. Simulated versus predicted fields given S-pol light incident for aligned anisotropic medium at 9 GHz and $\theta = 5$ degrees.

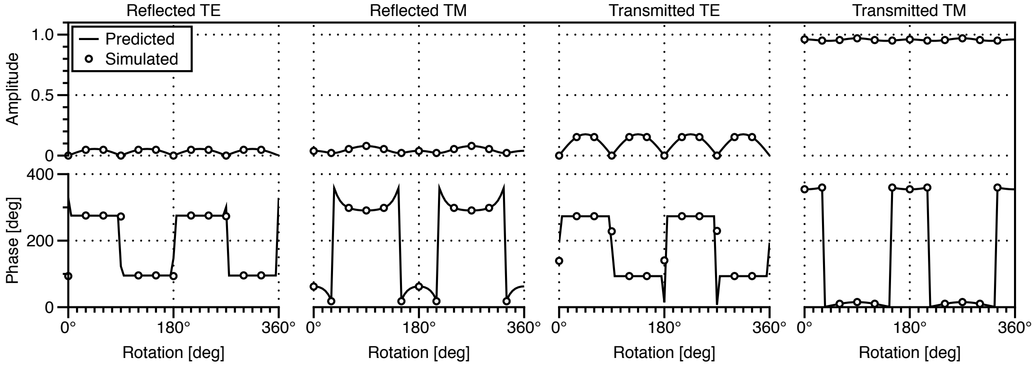

Figure 43. Simulated versus predicted fields given P-pol light incident for aligned anisotropic medium at 9 GHz and $\theta = 5$ degrees.

The test of the accuracy of these extracted values is found in their predictive power. Using the 4x4 matrix methodology, the predicted fields of the structure can be found at any angle of incidence and sample rotation given the permittivity and permeability tensor. This provides an excellent check, as FLO_K can easily simulate the structure and calculate coefficients, and these can be directly compared with the PPTE predictions. Both the PPTE and FLO_K results are shown in Figures 42 and 43 for the TE and TM incident cases at 9 GHz.

The relative error between the predicted fields and the simulated fields are shown in Figure 44. The error is calculated as a percentage, treating the FLO_K simulation as the correct result. The average relative error per frequency is shown in Figure 44.

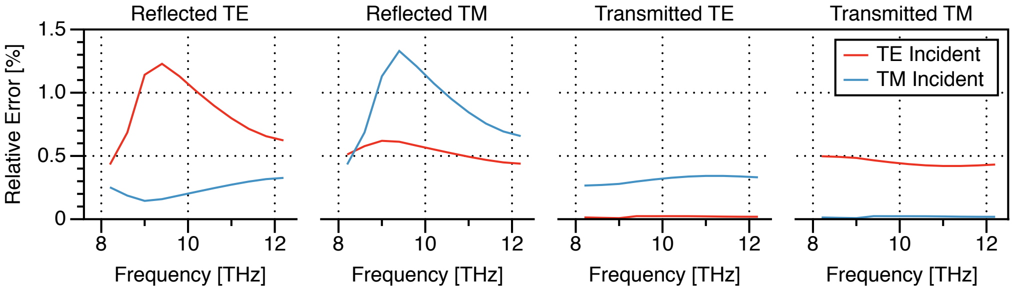

Figure 44. Relative field amplitude errors for aligned anisotropic medium. The error is calculated assuming that the FLO_K simulation is the correct value.

The average relative error is higher for the reflection case, which is likely due to the lower overall signal. The transmission error is much lower. In almost all cases, the cross-polarization case error is higher than the same-polarization case. The maximum relative error for this group of simulations and predictions is less than 1.5%, which is remarkably low. This shows that the extracted permittivities and permeabilities show excellent predictive capabilities, and can be used to accurately predict fields for a wide variety of situations. It should be noted that this is all for a single angle of incidence.

Note that there is a huge difference in the time it takes for each of these calculations. FLO_K takes roughly 2 minutes per angle of incidence per sample rotation per frequency. The predictions offered by PPTE is calculated using a MATLAB script in a fraction of a minute for all angles and frequencies. For instance: a 360 degree sample rotation with 30 degree increments at 12 frequencies would take FLO_K approximately four-and-a-half hours to complete. The PPTE prediction for eight times as many frequencies and 5 degree sample rotation increments takes 15 seconds, which includes 3 seconds to calculate the effective permittivities and permeabilities.

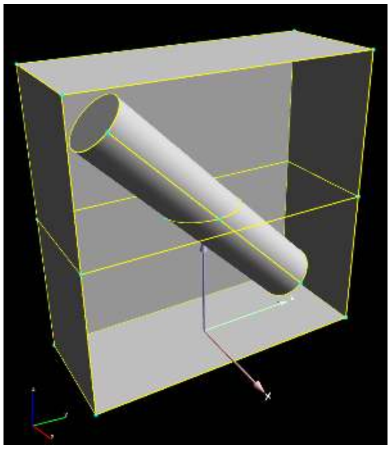

Figure 45. Picture of tilted nanorod. The rod is 500 nanometers long, 100 nanometers in diameter, and tilted at 45 degrees with respect to $\hat{x}$. The unit cell has dimensions 200 nanometers in $\hat{x}$ by 500 nanometers in $\hat{y}$, and the substrate is 500 nanometers thick (in $\hat{z}$).

4.7.4 Full Tensor Metamaterial.

The two samples examined previously are both samples which can be analyzed using traditional permittivity and permeability extraction techniques. They are valuable to examine, as they show that the extraction methodology proposed here can give accurate results, but do not model the kinds of behaviors which require this particular technique. The next sample examined here does have such behaviors, and thus requires the proposed extraction technique.

The scene itself is straighforward; it is a small metallic rod suspended in a silicon-like substrate, as shown in Figure 45. The reason this extraction technique is needed is due to the orientation of the rod; the rod is tilted at 45 degrees with respect to normal. This has the effect of making a crystalline-like permittivity, as shown in works such as Schmidt's [75–77]. Crystalline structures often have non-diagonalized tensors, which this structure will be shown to exhibit.

The actual geometry of the structure is fairly simple. The metallic rod is defined as 500 nanometers in length, with a diameter of 100 nanometers. The rod is suspended in the middle of the substrate, rotated at 45 degrees about the x-axis. The rod's

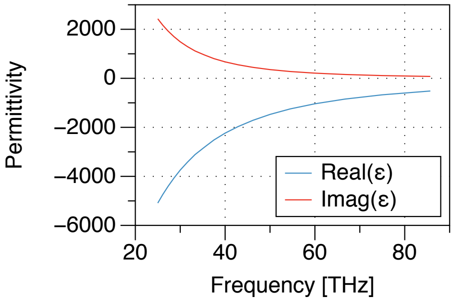

Figure 46. Silver permittivity. The data is interpolated using oscillators from the measurements of Rakic [69].

permittivity is shown in Figure 46, and was chosen to model silver's bulk permittivity as closely as possible, given the reference data of Rakic [69]. The substrate has a permittivity of 11, which is similar to the permittivity of silicon over the frequency range modeled here. As the following structures are simulated within the terahertz regime, the relative permeability of all materials is treated as 1 [92]. The unit cell is 200 nanometers by 500 nanometers in $\hat{x}$ and $\hat{y}$ respectively, and is 500 nanometers thick.

The extraction process is fairly straightforward. There are four simulations which are performed which simulate the reflection and transmission coefficients. Each simulation is done at a single angle of incidence and sample rotation. For this process, the four sample rotations are

1. $\phi = 0°$, used as the forward experiment in $\Delta^{(xx)}$,
2. $\phi = 90°$, used as the forward experiment in $\Delta^{(xy)}$,
3. $\phi = 180°$, used as the backward experiment in $\Delta^{(xy)}$ (due to sample symmetry), and
4. $\phi = 270°$, used as the backward experiment in $\Delta^{(xy)}$ (due to sample symmetry).

Performing the simulations in this way was mentioned earlier in Section 4.3.1, and can be seen in Figure 32.

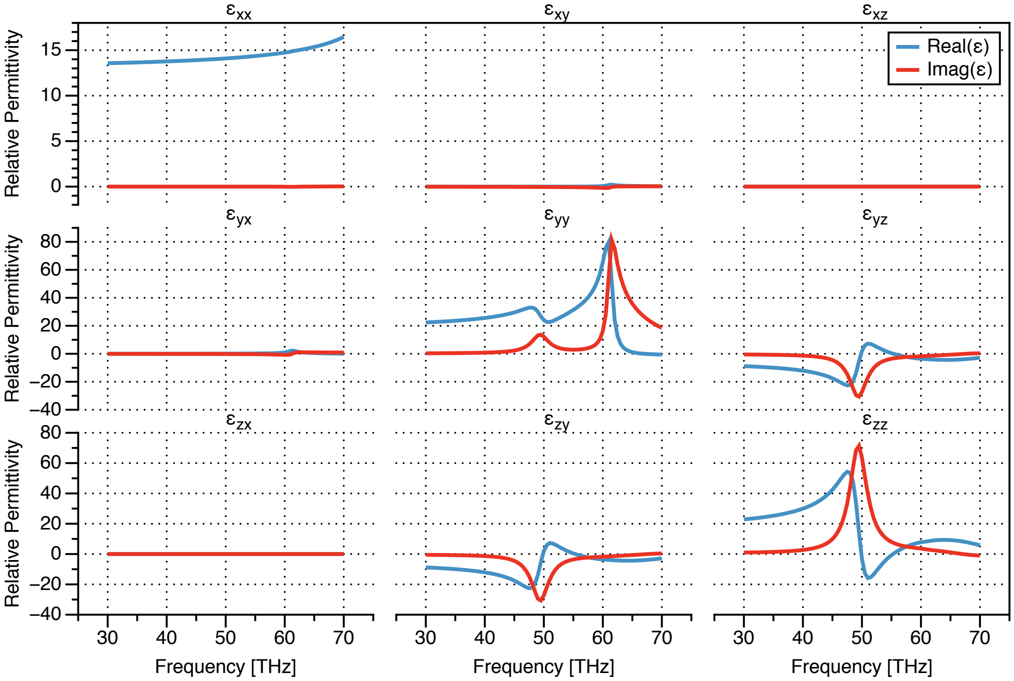

Figure 47. Tilted nanorod permittivity tensor extracted using PPTE. The xy, xz, yx, and zx elements are not zero, but are small compared to the other tensor elements.

In all four simulations, $\theta = 5$ degrees. The frequencies utilized here are 30 to 70 Terahertz (4.5 to 10 microns), at a spacing of 0.5 THz. The extracted permittivity and permeability using the PPTE technique is shown in Figures 47 and 48. Since the effective material permittivity is shown here to be fairly low, there is a unnoticeable amount of noise on the extracted zz components.

The amplitude of the off-diagonal elements shows that there is significant optical activity off of the lab axes. The activity points towards a coupling effect between the $\hat{y}$ and $\hat{z}$ axes. The high absorption in the zz element with the negative absorption in the yz and zy elements elements indicates that power incident along $\hat{z}$ excites waves along the $\hat{y}$ axis.

One of the questions that may arise is the impact of the mesh size on the simulations. Two sets of simulations were carried out using the same geometry, but different meshing, to compare the extracted elements. These extractions are shown in Figures

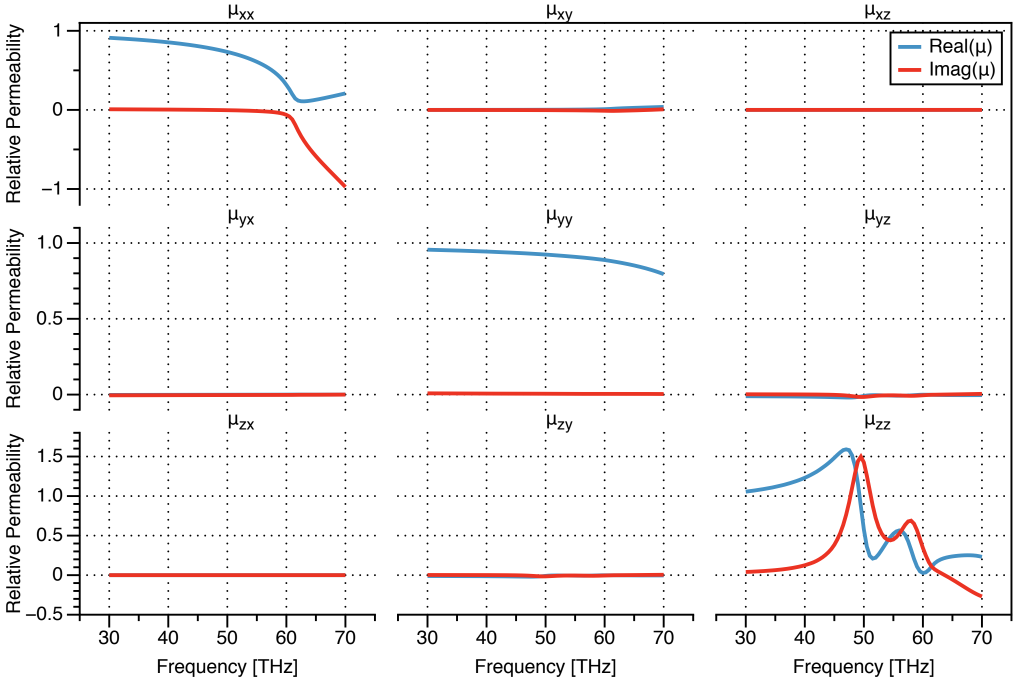

Figure 48. Tilted nanorod permeability tensor extracted using PPTE. The off-diagonal tensor elements are not zero, but are small compared to the other tensor elements.

49 and 50. The high-resolution mesh had roughly twice the volumetric elements as the mid-resolution mesh. The lower resolution seems to have little impact on the overall numbers, save for the lower amplitude on the xz and zx elements. These two tensor elements were significantly stronger in the mid-resolution case than the high-resolution case, but still are insignificant compared to the other tensor elements such as the zz element. Overall, there are negligible differences between the two simulation sets, other than the much longer computational time for the higher resolution.

The extracted permittivity and permeability tensors accurately predict the reflection and transmission coefficients of the material. Using the methods detailed in the previous section, the reflection and transmission coefficients can be calculated for any angle of incidence given the permittivity and permeability tensors. These predictions can be directly compared to the outputs of the FLO_K simulations. A comparison of the predictions and the simulations can be seen in Figure 51. The simulations have

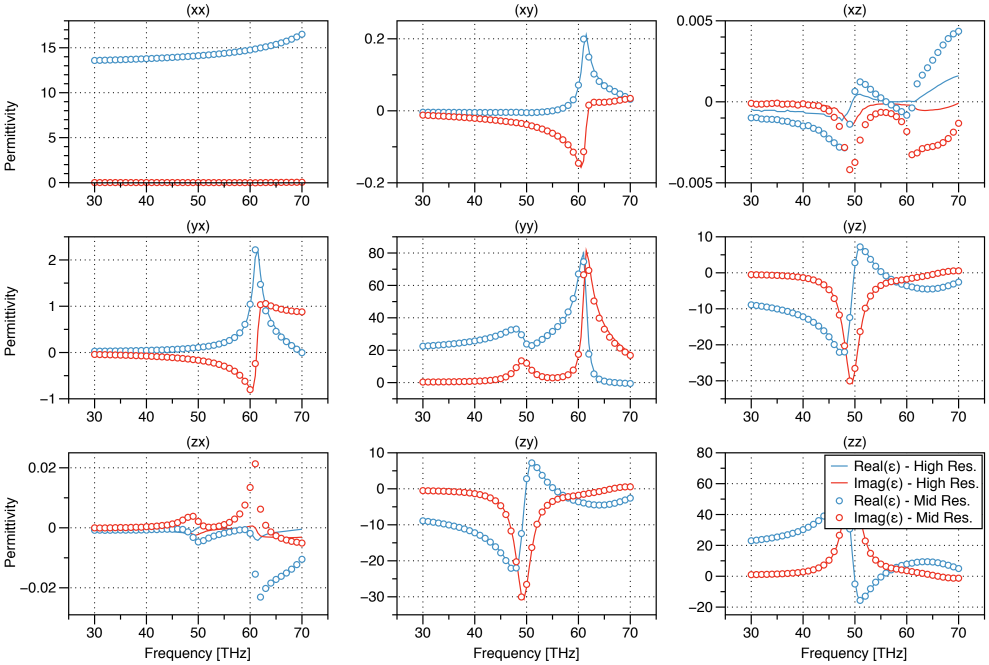

Figure 49. Comparison between the extracted permittivity tensors for the mid-resolution and the high-resolution scene. The xz and zx tensor elements are much closer to zero for the high-resolution case; the other elements are very similar.

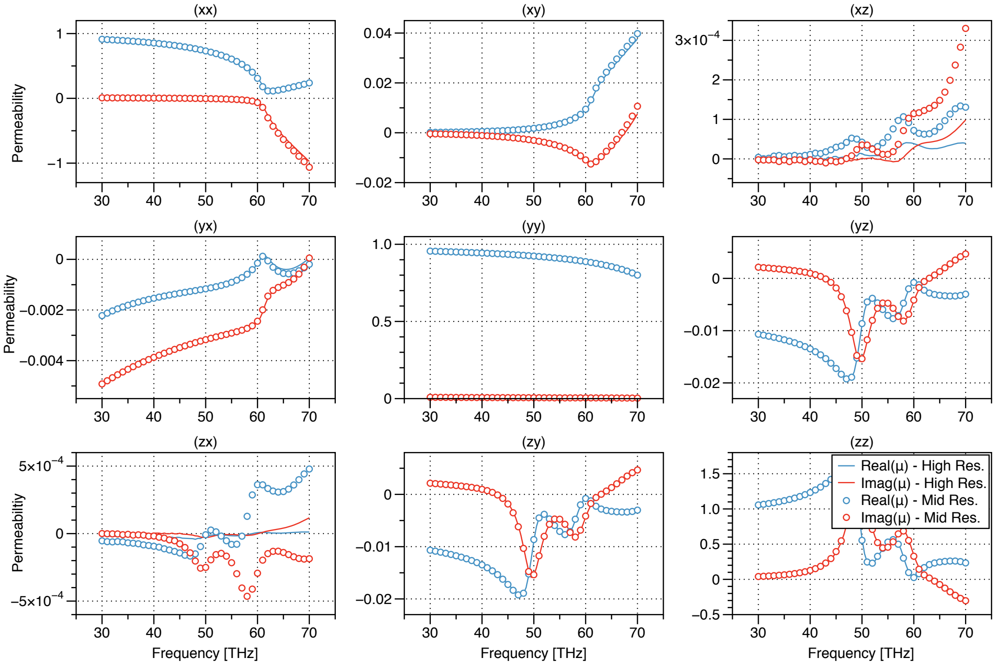

Figure 50. Comparison between the extracted permeability tensors for the mid-resolution and the high-resolution scene. The xz and zx tensor elements are much closer to zero for the high-resolution case; the other elements are very similar.

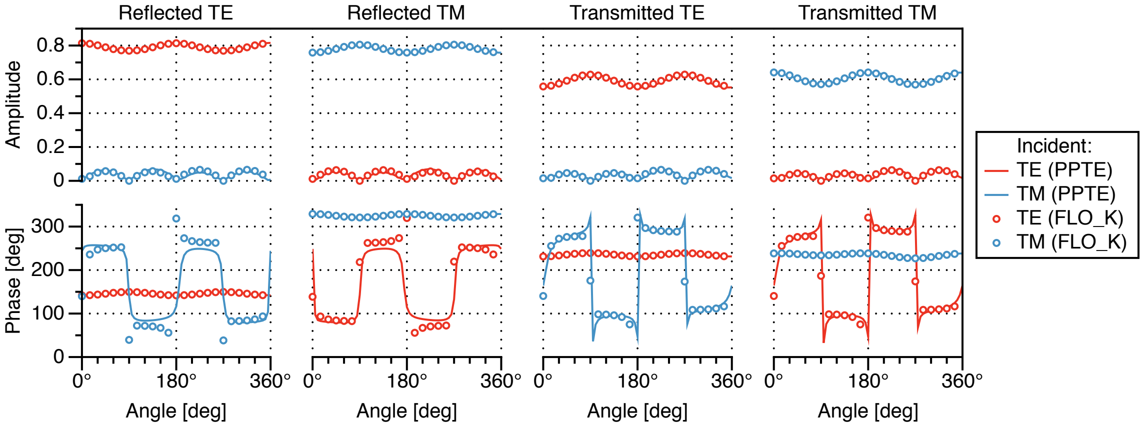

Figure 51. Predicted and simulated fields of the nanorod sample at 65 THz.

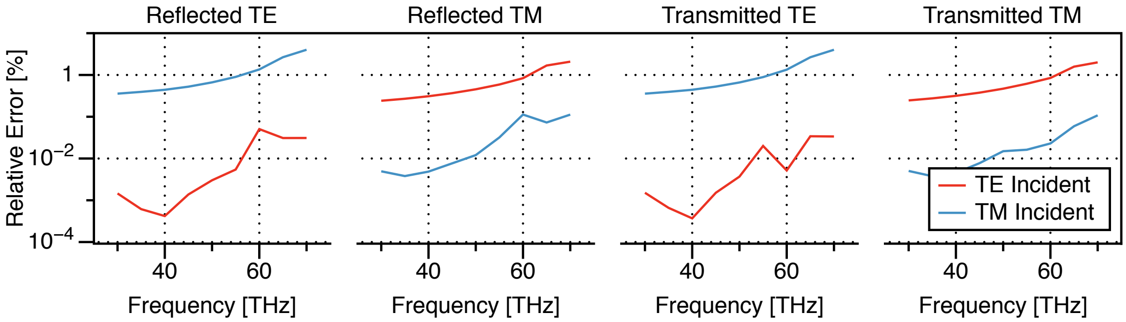

Figure 52. Relative error plot of the titled nanorods, comparing the predicted fields to the simulated fields. The simulated fields are considered to be the correct fields.

been shown to be very accurate under many circumstances. The error is frequency dependent; lower frequencies tend to indicate lower error. This is mainly due to the effective medium approximation, which does not hold as the wavelength approaches the feature size. A figure indicating the relative error as a function of wavelength at $\theta = 10$ degrees is shown in Figure 52.

It is shown in Figure 52 that the average relative error is overall very low, especially in the case of the same-polarization waves (such as TE incident and TE reflected). The cross-polarization waves have a higher error, which peaks for this particular simulation around 7%. The cross-polarization error is $< 2.5\%$ at all frequencies less than 65 THz. The optical activity at the higher frequencies likely makes the effective medium approximation invalid at these frequencies, which points to a physical basis for the error. Overall, this is very low error compared to the FLO_K simulations. It should be noted that, for this particular simulation, FLO_K took on the order of 24 hours for nine wavelengths and 24 angles, while the MATLAB code used to predict the optical activity took less than a minute. This goes to show that this is an accurate and valuable tool for predicting optical activity from a small quantity of simulated data.

4.8 Conclusion

This new parameter extraction process removes many of the previous limits on the abilities to extract effective material parameters. The PPTE technique allows for materials with any permittivity or permeability to be analyzed utilizing a straightforward process and a few basic assumptions. The process is shown here to be highly accurate in simple cases where the permittivity is known, as demonstrated by the isotropic case. The example of an aligned anisotropic case shows that the characteristics extracted by PPTE show excellent agreement with traditional parameter extraction techniques. The final sample analyzed in this chapter shows that PPTE can extract effective parameters when a metamaterial has a fully populated permittivity tensor; something that traditional techniques are unable to do. Furthermore, the agreement between the predicted fields using the PPTE extracted values and the CEM simulation shows that PPTE can be used to accurately predict how light is scattered from complex materials.

V. Inverting a Matrix Exponential

Chapter IV gives the PPTE technique for determining the effective material parameters of nonaligned anisotropic materials such as the silver nanorods which prompted this research. Within that process, there is a single step, the inversion of a matrix exponential operation, which requires a deeper level of analysis. The function which performs this step, ixp, will be defined and discussed in this chapter.

The field of metamaterial research has grown significantly within the last decade. Recently, researchers have begun to experiment with anisotropic structures that are not aligned with the laboratory frame of reference [28,54,76–78,81] . These structures have unique properties that cannot be found in other materials. These properties cannot be measured with traditional parameter extraction techniques due to the complexity of the materials.

In Chapter IV, the extraction methodology Permittivity and Permeability Tensor Extraction (PPTE) was proposed. This makes fewer assumptions about the material parameters than other techniques. The fewer assumptions yields an increase in the number of situations where the extraction methodology can be used, and allows for the analysis of non-aligned anisotropic materials. One of the steps involved in the process is the inversion of a matrix exponential operation, which is a difficult process due to the multiple roots of a logarithm.

This difficult step can be seen in inverting the operations present in Equation (169), where Δ_B is known, and T_p is calculated. Now, the following equation must be solved when $T_p(\omega)$ is known, but $\tilde{\Delta}(\omega)$ is unknown:

$$T_p(\omega) = \exp(\tilde{\Delta}).$$

While the natural logarithm, ln, function often correctly performs this inversion, there are many cases where the natural-log function returns a solution that is incongruous with the physics of the problem. This is due to the lack of injectivity (one-to-one) of the exponential function with complex inputs [53]. However, there are certain assumptions that can be impressed upon this problem so that an inverse of the exponential can be properly defined. These assumptions can be proved to be valid within the physics of this specific application. In the following section, the necessary assumptions to create an inverse-exponential function, ixp as seen in Equation (171), will be defined. Following this, several cases where this function is necessary to find the correct answer will be examined, both symbolically and through computational electromagnetic simulations.

5.1 Theory

The problem can be stated more generally: given a known complex square matrix B of size $N \times N$, solve for the unknown square matrix A when

$$B = \exp(A). \tag{241}$$

This problem is more difficult than many of the other examinations of this problem found elsewhere in literature due to the use of complex matrix elements [21–23]. Still, $\ln(\exp(A)) \neq A$ holds true in many situations [61].

While there are many ways to calculate the exponential of a matrix [62], the method most useful to this particular problem is to find the exponential of the eigenvalues of a matrix. If:

1. A and B are diagonalizable with a full set of shared linearly independent eigenvectors $\{\nu_1, \nu_2 \ldots \nu_N\}$,

2. A has eigenvalues $\{\lambda_1, \ldots \lambda_N\}$, counting repeated eigenvalues, and

3. B has eigenvalues $\{\Lambda_1, \dots \Lambda_N\}$, counting repeated eigenvalues,

then

$$\bar{\nu} \begin{bmatrix} \Lambda_1 & & & \\ & \Lambda_2 & & \\ & & \ddots & \\ & & & \Lambda_N \end{bmatrix} \bar{\nu}^{-1} = \bar{\nu} \begin{bmatrix} \exp \lambda_1 & & & \\ & \exp \lambda_2 & & \\ & & \ddots & \\ & & & \exp \lambda_N \end{bmatrix} \bar{\nu}^{-1} \tag{242}$$

where $\bar{\nu} = [\nu_1 | \dots | \nu_N]$, which is the matrix formed by concatenating the column eigenvectors.

These equations then imply for all $k \in \{1, \dots N\}$ that

$$\Lambda_k = \exp \lambda_k$$

therefore,

$$\log \Lambda_k = \log \left(\exp \left(\lambda_k \right) \right)$$

where log denotes the complex-valued logarithm function, so that

$$\log |\Lambda_k| + i \text{Arg } \Lambda_k + i2\pi m_k = \lambda_k \tag{243}$$

where Arg is the principal argument of the complex number, that is, $\text{Arg}\,(z) \in (-\pi, \pi]$ [100], and m_k is any integer. This gives a method for recovering Λ_k given λ_k, a known value, and m_k, which is an unknown integer. Therefore, the only problem left to solve is the inversion operation to find the correct m_k for the k^{th} entry.

This problem is has no unique solution given no extra constraints. Any $m_k \in \mathbb{Z}$ is a possible solution, which offers several solutions that may or may not be the desired matrix A. However, the physics of this particular application allow for an additional set of constraints that can be used to find the correct solution.

Now, the problem will be restated slightly to allow for an independent variable, that is,

$$B(\omega) = \exp(A(\omega)), \tag{244}$$

where ω is a known, positive frequency. This implies that the eigenvalues and eigenvectors of these two matrices will share the spectral attribute. Two new attributes will be assumed for the eigenvalues $\lambda_k(\omega)$:

1. $\lambda_k(\omega)$ is continuous with respect to ω, and therefore $\Lambda_k(\omega)$ is continuous with respect to ω.
2. $\mathrm{Im}\{\lambda_k(\omega)\}$ approaches 0 as ω approaches 0, and therefore $\mathrm{Im}\{\Lambda_k(\omega)\}$ approaches zero as ω approaches 0.

Note that the eigenvalues of a matrix are continuous if the individual elements of the matrix are continuous. The proof of this can be completed using the Implicit Function Theorem (IFT) [51, 66]. The eigenvalues of the matrix A can be found by solving the following equation for λ:

$$\det|A - \lambda I| = 0. \tag{245}$$

The determinant of a matrix will always be expressible as some polynomial. This means that Equation (245) can be expressed as

$$p(\overrightarrow{A}, \lambda) = 0 \tag{246}$$

where p is some polynomial, $\overrightarrow{A}$ is a vector made of the elements of A, and λ is some scalar to be determined.

The IFT gives that for the neighborhood around the matrix A_0 and the scalar λ, there exists some function g such that $\lambda = g(\overrightarrow{A})$ and $f(\overrightarrow{A}, g(\overrightarrow{A})) = 0$ for A in the neighborhood about A_0. Furthermore, IFT guarantees that the function g will be well behaved around this point. This shows that the eigenvalues of the matrix A will be continuous presuming that the elements of the matrix A are continuous.

If these two assumptions hold true, then there exists some $\omega = \omega_k$ such that

$$\log(\Lambda_k(\omega)) = \lambda_k(\omega) \quad \text{for all} \quad \omega < \omega_k. \tag{247}$$

This further implies that there is some frequency ω_0 such that $m_k = 0$ for all $k \in \{1, ..., N\}$. From ω_0, $m_k(\omega)$ can be chosen such that $\log \Lambda_k(\omega) + i2\pi m_k(\omega)$ is continuous in ω. This allows the value of $m_k(\omega)$ to be correctly determined for all ω given a single frequency ω_0 such that $m_k(\omega_0) = 0$ for all $k \in \{1, ..., N\}$. Then,

$$\lambda_k(\omega) = \log \Lambda_k(\omega) + i2\pi m_k(\omega), \tag{248}$$

and

$$A(\omega) = \bar{\nu}(\omega) \begin{bmatrix} \lambda_1(\omega) & & & \\ & \lambda_2(\omega) & & \\ & & \ddots & \\ & & & \lambda_N(\omega) \end{bmatrix} \bar{\nu}^{-1}(\omega). \tag{249}$$

One of the final aspects of the problem to address is the fact that routines and methods for extracting eigenvalues have no way to identify which eigenvalue is which. Routines will typically report the N eigenvalues of the problem with no sorting whatsoever. This problem can be overcome once again using the continuity of the eigenvalues. In general, the easiest way found to address this problem is to sort the eigenvalues by their real component, which is accurate before the m_k correction. After this sorting, identify points where the real portions of the eigenvalues cross, and correct them such that both the real and imaginary portions of the eigenvalues are continuous.

Identifying these points automatically can be done by comparing the dot product of one eigenvector with the same eigenvector at the previous frequency. If the dot product of the normalized eigenvectors is not close to one, it can be assumed that eigenvalues and eigenvectors need to be swapped with another eigenvalue to retain continuity. Note that the eigenvectors are, in general, not continuous with respect to ω, but are locally continuous in many cases. Typically, the problem is immediately obvious and easily correctable when a user examines a plot of the real and imaginary components of the eigenvalues. An example of this will be shown in Section 5.4.3.

5.2 Physical Application

Section 4.4 presented the equation

$$T_p(\omega) = \exp\left(i\frac{\omega}{c}\Delta_B(\omega)d\right) \equiv \exp\tilde{\Delta}(\omega) \tag{250}$$

where

$$\tilde{\Delta}(\omega) = i\frac{\omega}{c}\Delta_B(\omega)d. \tag{251}$$

Here, T_p is a known, extracted set of matrices, ω is the frequency of the light incident within the simulation, c is the speed of light, d is the layer thickness, and Δ_B is Berreman's matrix, an unknown matrix that is to be determined. $\tilde{\Delta}$ is the scaled version of the same matrix. As stated in Section 5.1, inverting the exponential operator in this step is not trivial. However, if the conditions stated above are true for this application, then there exists some algorithm which can solve the problem as

$$\Delta_B(\omega) = -i\frac{c}{\omega d}\mathrm{ixp}\left(T_p(\omega)\right). \tag{252}$$

Here, ixp() is the proposed algorithm for inverting the matrix exponential given the two assumptions stated above.

In order to confirm that these two assumptions are valid for this particular problem, the underlying structure of the matrix Δ_B must first be discussed. The structure of this matrix was given in Equation (176) as

$$\Delta_B = \begin{bmatrix} -K_{xx}\dfrac{\epsilon_{zx}}{\epsilon_{zz}} & K_{xx}\left[\dfrac{\mu_{yz}}{\mu_{zz}} - \dfrac{\epsilon_{zy}}{\epsilon_{zz}}\right] & \mu_{yx} - \dfrac{\mu_{yz}\mu_{zx}}{\mu_{zz}} & \mu_{yy} - \dfrac{\mu_{yz}\mu_{zy}}{\mu_{zz}} - \dfrac{K_{xx}^2}{\epsilon_{zz}} \\ 0 & -K_{xx}\dfrac{\mu_{xz}}{\mu_{zz}} & \dfrac{\mu_{xz}\mu_{zx}}{\mu_{zz}} - \mu_{xx} & \dfrac{\mu_{xz}\mu_{zy}}{\mu_{zz}} - \mu_{xy} \\ \dfrac{\epsilon_{yz}\epsilon_{zx}}{\epsilon_{zz}} - \epsilon_{yx} & \dfrac{K_{xx}^2}{\mu_{zz}} + \dfrac{\epsilon_{yz}\epsilon_{zy}}{\epsilon_{zz}} - \epsilon_{yy} & -K_{xx}\dfrac{\mu_{zx}}{\mu_{zz}} & K_{xx}\left[\dfrac{\epsilon_{yz}}{\epsilon_{zz}} - \dfrac{\mu_{zy}}{\mu_{zz}}\right] \\ \epsilon_{xx} - \dfrac{\epsilon_{xz}\epsilon_{zx}}{\epsilon_{zz}} & \epsilon_{xy} - \dfrac{\epsilon_{xz}\epsilon_{zy}}{\epsilon_{zz}} & 0 & -K_{xx}\dfrac{\epsilon_{xz}}{\epsilon_{zz}} \end{bmatrix} \tag{253}$$

where the permittivity tensor $\boldsymbol{\epsilon}$ and permeability tensor $\boldsymbol{\mu}$ are given as

$$\boldsymbol{\epsilon} = \begin{bmatrix} \epsilon_{xx} & \epsilon_{xy} & \epsilon_{xz} \\ \epsilon_{yx} & \epsilon_{yy} & \epsilon_{yz} \\ \epsilon_{zx} & \epsilon_{zy} & \epsilon_{zz} \end{bmatrix} \quad \text{and} \quad \boldsymbol{\mu} = \begin{bmatrix} \mu_{xx} & \mu_{xy} & \mu_{xz} \\ \mu_{yx} & \mu_{yy} & \mu_{yz} \\ \mu_{zx} & \mu_{zy} & \mu_{zz} \end{bmatrix}. \tag{254}$$

K_{xx} is a propagation constant, and is $= n_i \sin\theta_i$ where n_i is the incident medium of the problem and θ_i is the angle of incidence.

The first assumption in the previous section is the continuity of the eigenvalues λ_k, which are the eigenvalues of $\tilde{\Delta}(\omega)$. Expressing the eigenvalues in terms of the elements given in equation (253) is prohibitively difficult. However, if the individual elements of Δ_B are continuous, then the eigenvalues of $\tilde{\Delta}$ must be continuous via the IFT. Examining equation (253), if all of the $\boldsymbol{\epsilon}$ and $\boldsymbol{\mu}$ tensor elements are continuous, then the only time that the eigenvalues of Δ_B are not continuous is when ϵ_{zz} or μ_{zz} are equal to zero. PPTE already makes this assumption, so it can be assumed that the eigenvalues of $\tilde{\Delta}(\omega)$ are continuous.

The second assumption is that the imaginary portion of the eigenvalues can be forced to zero as ω goes to zero. This seems to be a fairly reasonable assumption given the problem statement. The eigenvalues of the matrix $\tilde{\Delta}$ are the same as the eigenvalues of Δ_B scaled by several constants as well as the frequency. If the frequency goes to zero, it is reasonable to assume that the eigenvalues of $\tilde{\Delta}$ go to zero as well, as the eigenvalues are scaled by the frequency. In the later section, several simplified cases will be examined, and this property will be shown to be true in these cases. In the event that the permittivities and permeabilities are modeled using classical oscillator models, such as the Drude and Lorentz oscillators covered in Section 2.2.3, it can be shown that the imaginary portion of the eigenvalues always goes to zero as the frequency approaches zero.

This gives a straightforward algorithm which performs the ixp() operation.

1. Extract eigenvalues and eigenvectors of $T_p(\omega_0)$ as Λ_k and ν_k, respectively.
2. Sort the eigenvalues by $\operatorname{Re}\{\log \Lambda_k\}$.
3. Switch eigenvalues and eigenvectors as needed.
4. $\lambda_k(\omega_0) = \log \Lambda_k(\omega_0)$
5. For each k, pick $m_k(\omega)$ such that $\log \Lambda_k + i2\pi m_k(\omega)$ is continuous with $\lambda_k(\omega_0)$.
6. $\tilde{\Delta}(\omega) = [\nu_1|\nu_2|\nu_3|\nu_4]\operatorname{diag}(\lambda_1, \lambda_2, \lambda_3, \lambda_4)\,[\nu_1|\nu_2|\nu_3|\nu_4]^{-1}$.

5.3 Eigenvalues of the scaled matrix Δ

5.3.1 Isotropic Case.

The underlying form of the matrix Δ_B is assumed and given in equation (253). Finding the eigenvalues of a 4-by-4 matrix is difficult, especially when there are 19 variables distributed over 14 matrix elements. However, there are some assumptions that can be used to simplify the problem greatly, and hint at the underlying physics of the problem.

The first case which will be examined here is where the material is isotropic. This makes the permittivity tensor $\boldsymbol{\epsilon} = \epsilon_i I$ and the permeability tensor $\boldsymbol{\mu} = \mu_i I$, where I is the identity matrix. The matrix Δ_B is

$$\Delta_B = \begin{bmatrix} 0 & 0 & 0 & \mu_i - \frac{K_{xx}^2}{\epsilon_i} \\ 0 & 0 & -\mu_i & 0 \\ 0 & \frac{K_{xx}^2}{\mu_i} - \epsilon_i & 0 & 0 \\ \epsilon_i & 0 & 0 & 0 \end{bmatrix}. \tag{255}$$

The eigenvalues of this matrix are then equal to $\left\{\pm\sqrt{\epsilon_i\mu_i - K_{xx}^2}\right\}$ which implies that the eigenvalues of the scaled matrix $\tilde{\Delta}$ are

$$\{\lambda_k\} = \left\{\pm i\frac{\omega}{c}d\sqrt{\epsilon\mu - K_{xx}^2}\right\}, \tag{256}$$

each repeated twice. Note that this demonstrates that even a simple material will have negative eigenvalues. For a brief discussion of the physical interpretation of eigenvalues and eigenvectors within this application, see Appendix C.

It can be seen from the equation (256) that the eigenvalues of an isotropic material are continuous provided that ϵ_i and μ_i are both continuous. The constants c (the speed of light) and d (layer thickness) are fixed, K_{xx}^2 is some real value between 0 and 1, and ω is the variable. This proves that, for the isotropic case, the two distinct eigenvalues are continuous functions.

Furthermore, these eigenvalues approach zero in nearly all cases. In general, optical metamaterials typically have a relative permeability of 1 at the lower frequencies.

If this permeability were to behave more like a Drude oscillator [93], then the assumption that the eigenvalues approaches zero would be a poor one. For example, if the permittivity of the isotropic medium were to be modeled by a Drude oscillator, the permittivity would be defined as

$$\epsilon_i = 1 - \frac{A_\epsilon}{\omega^2 + i\Gamma_\epsilon \omega} \tag{257}$$

where A_ϵ is the oscillator amplitude and Γ_ϵ is the oscillator broadening. If the permeability were to be described by the same model with amplitude A_μ and broadening Γ_μ, then the eigenvalues would be

$$\{\lambda_k\} = \left\{ \pm i \frac{\omega}{c} d \sqrt{\left[1 - \frac{A_\epsilon}{\omega^2 + i\Gamma_\epsilon \omega}\right] \left[1 - \frac{A_\mu}{\omega^2 + i\Gamma_\mu \omega}\right] - K_{xx}^2} \right\}, \tag{258}$$

each repeated twice. Taking the limit as $\omega \to 0$ gives

$$\begin{aligned} \{\lambda_k\} &= \left\{ \pm i \frac{d}{c} \sqrt{\lim_{\omega \to 0} \left[\frac{A_\epsilon A_\mu \omega^2}{\omega^4 - i(\Gamma_\epsilon + \Gamma_m u)\omega^3 - \Gamma_\epsilon \Gamma_\mu \omega^2} \right]} \right\}. \\ &= \left\{ \pm i \frac{d}{c} \sqrt{\frac{A_\epsilon A_\mu}{-\Gamma_\epsilon \Gamma_\mu}} \right\} = \left\{ \pm \frac{d}{c} \sqrt{\frac{A_\epsilon A_\mu}{\Gamma_\epsilon \Gamma_\mu}} \right\}. \end{aligned} \tag{259}$$

Note that A_ϵ, A_μ, Γ_ϵ, and Γ_μ are all positive real-valued. Therefore,

$$\operatorname{Im}\left\{ \lim_{\omega \to 0} \{\lambda_k\} \right\} = 0, \tag{260}$$

and the necessary conditions are shown to be met. Should either ϵ_i or μ_i be modeled by a Drude oscillator while the other is a constant at low frequencies, a similar analysis would show that the absolute value of the limit is zero. This is the most common case in practice.

5.3.2 Aligned Anisotropic.

In the case of an anisotropic material with orthogonal axes aligned with the lab frame of reference [52], the permittivity tensor becomes

$$\boldsymbol{\epsilon} = \begin{bmatrix} \epsilon_{xx} & 0 & 0 \\ 0 & \epsilon_{yy} & 0 \\ 0 & 0 & \epsilon_{zz} \end{bmatrix}$$

and the permeability tensor

$$\boldsymbol{\mu} = \begin{bmatrix} \mu_{xx} & 0 & 0 \\ 0 & \mu_{yy} & 0 \\ 0 & 0 & \mu_{zz} \end{bmatrix}.$$

The matrix Δ_B is then

$$\Delta_B = \begin{bmatrix} 0 & 0 & 0 & \mu_{yy} - \frac{K_{xx}^2}{\epsilon_{zz}} \\ 0 & 0 & -\mu_{xx} & 0 \\ 0 & \frac{K_{xx}^2}{\mu_{zz}} - \epsilon_{yy} & 0 & 0 \\ \epsilon_{xx} & 0 & 0 & 0 \end{bmatrix}.$$

This matrix has eigenvalues

$$\left\{ \pm\sqrt{\frac{\epsilon_{xx}}{\epsilon_{zz}}}\sqrt{\epsilon_{zz}\mu_{yy} - K_{xx}^2}, \pm\sqrt{\frac{\mu_{xx}}{\mu_{zz}}}\sqrt{\epsilon_{yy}\mu_{zz} - K_{xx}^2} \right\} \tag{261}$$

which gives

$$\{\lambda_k\} = \left\{ \pm\frac{\omega}{c}d\sqrt{\frac{\epsilon_{xx}}{\epsilon_{zz}}}\sqrt{\epsilon_{zz}\mu_{yy} - K_{xx}^2}, \pm\frac{\omega}{c}d\sqrt{\frac{\mu_{xx}}{\mu_{zz}}}\sqrt{\epsilon_{yy}\mu_{zz} - K_{xx}^2} \right\}. \tag{262}$$

These eigenvalues are continuous given that neither ϵ_{zz} nor μ_{zz} are equal to zero. This is one of the assumptions that is presumed within the PPTE technique, so it can be said that the eigenvalues of an aligned anisotropic medium are continuous in all cases where the PPTE technique is used. By lowering the frequency, the eigenvalues can be again forced towards zero in almost all cases. The cases where they cannot are similar to the isotropic case, but even more restrictive.

5.3.3 Generalized Anisotropic.

Calculating the eigenvalues and eigenvectors for the most generalized case is prohibitively difficult. There are nineteen values that all need to appear within the solution, which makes a closed-form solution complex to the point of uselessness. However, there are some additional characteristics of the eigenvalues that can be determined by analyzing the physics of the problem.

The eigenvectors of the matrix T_p are vectors that satisfy the following equation:

$$\Lambda_k \begin{bmatrix} E_x & E_y & H_x & H_y \end{bmatrix}^T = T_p \begin{bmatrix} E_x & E_y & H_x & H_y \end{bmatrix}^T \tag{263}$$

where E and H refer to the electric and magnetic fields at the layer boundaries. (This equation is similar to Equation (91) presented in Section 2.3.3.) This equation means that the eigenvectors are collections of fields that are identical on the top and bottom of the layer. One of the initial assumptions to PPTE (listed in Section 4.3.1) is that there are two unique polarization states that are transmitted through the material, which guarantees two unique eigenvectors. If it is assumed that light can similarly propagate through the material in the opposite direction, then there are two more unique eigenvectors. (Note that the eigenvalues with positive real components indicate that the associated eigenvectors are the back-traveling case, while the negative real component eigenvalues are for the forward propagating case.

Appendix C covers this in slightly more detail.) If there are four eigenvectors, there are four eigenvalues.

Unfortunately, the physics of the problem does not guarantee that the imaginary portion of all of these eigenvalues approaches zero in all conceivable cases, but it can be easily assumed that these eigenvalues share similar characteristics to the previously discussed cases. These assumptions have been valid in all of the cases examined here and in other research carried out with this methodology.

5.4 Simulations

5.4.1 Experimental results.

All of the simulations carried out in this section were performed using the FLO_K platform. For more details, see Section 4.7.

5.4.2 Isotropic Plane.

One of the most basic tests of this theory is to examine the case of an isotropic plane. The theory presented above provides that the plane will have four eigenvalues, two of which are duplicates of the other two. It needs to be shown that the imaginary portion of the eigenvalues goes towards zero as the frequency approaches zero. The two following cases demonstrate that this is true in materials which can be modeled with Drude-like oscillators, which is an oscillator often used to model the permittivities of metals [93].

The first isotropic case is one where the permittivity of the material is a single strong Drude oscillator chosen to closely model silver. The permeability of this material is that of free-space. The amplitude of the eigenvalues of the computed $\tilde{\Delta}$ matrix do go to zero with frequency, which is shown in Figure 53. The layer thickness was chosen as 350 nanometers. This causes the imaginary portion of the eigenvalues to

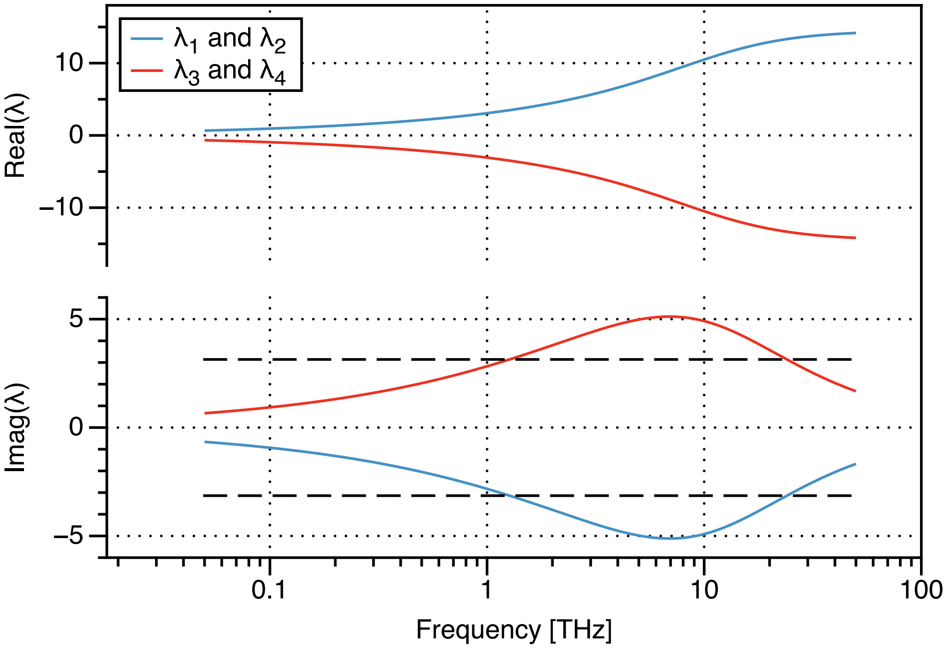

Figure 53. Eigenvalues of an isotropic slab with a silver-like permittivity. Real portions of the eigenvalues are on top; imaginary portion is on the bottom. The dashed lines note the $\pm\pi$ points.

increase past $\pm\pi$, which means the ixp algorithm is required to arrive at the correct values of λ_k. In this simulation, the imaginary portion crosses the $\pm\pi$ point twice, first at 1.3 THz, then again at 22 THz.

A second isotropic case is one where both the permittivity and the permeability of the material are modeled with Drude oscillators. To the best of my knowledge, this is a purely fictitious material; no material with a Drude-like permeability is known. This was shown above to be a sort-of "worst-case-scenario". Equation (260) shows that the eigenvalues will be purely real in the limit, which is what is demonstrated in Figure 54. The imaginary portion does go to zero, which allows the algorithm to identify and use the proper root in the extraction.

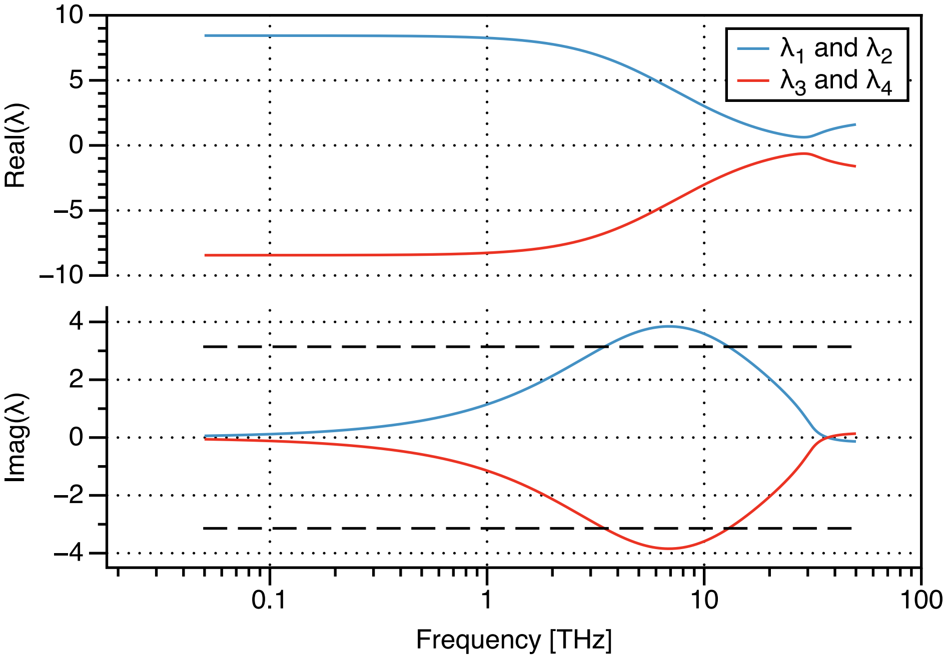

Figure 54. Eigenvalues of an isotropic slab with a drude-like permittivity and permeability (as opposed to Figure 53, which has a constant permeability). Real portions of the eigenvalues are on top; imaginary portion is on the bottom. The dashed lines note the $\pm\pi$ points.

5.4.3 Anisotropic Plane.

A simple anisotropic structure is a thick silicon plane with regularly-spaced, embedded silver nanocolumns. Assuming that the spacing is equal in both $\hat{x}$ and $\hat{y}$, it can be easily presumed that the plane will exhibit two unique permittivities and permeabilities; one across the plane, and one through the plane. If the layer is thick, then the imaginary portion of the eigenvalues will require correction.

The following is the results from a simulation with nanocolumns with a diameter of 200 nanometers and a length of 2 microns. The columns have silver permittivities and are embedded in a silicon-based substrate with permittivity $\epsilon = 11 + i0.1$. The lossy component is required to avoid some problems with constructive interference forcing the effective permittivity to zero. The columns are regularly spaced at 667 nanometers in both $\hat{x}$ and $\hat{y}$. The eigenvalues are shown in Figure 55, and the ex-

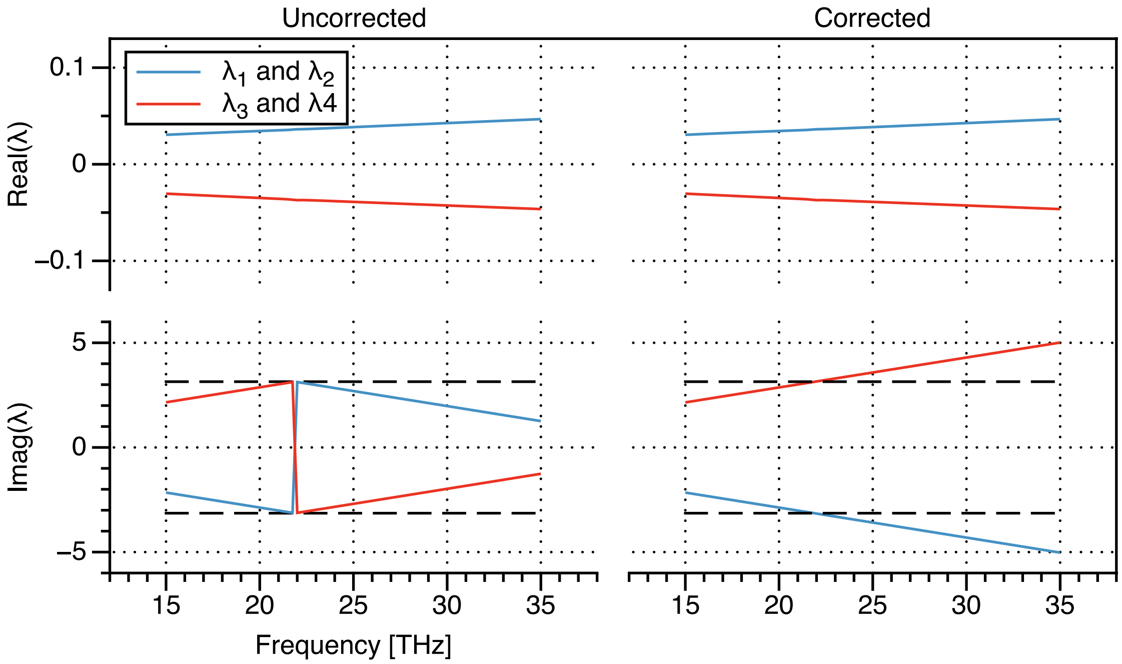

Figure 55. Eigenvalues of the anisotropic plane. The left plot demonstrates the uncorrected eigenvalues, while the right plot demonstrates the corrected values. $\lambda_1 = \lambda_2$ and $\lambda_3 = \lambda_4$ as the xx tensor elements are identical to the yy elements.

tracted permittivies and permeabilities are shown in Figure 56. Note the dashed black line in Figure 55 demonstrates the $\pm\pi$ range of the calculated eigenvalues; without the correction the information above or below this line would be incorrect.

If the natural log function was used to invert the matrix, the correction at 21.8 THz would not be present, which would lead to obviously incorrect results. An example of an extracted permittivity is shown in Figure 57. The extracted permeability shares similar characteristics; it abruptly drops from 0.8 to -1 at the same frequency, then steadily increases towards zero from there.

5.4.4 Tilted anisotropic structure.

The final material analyzed here is a metal cross tilted about $\hat{x}$. The geometry of this structure is shown in Figure 58. The cross is made of two perpendicular strips with widths of 200 nanometers. The long axis is one micron in length, while the

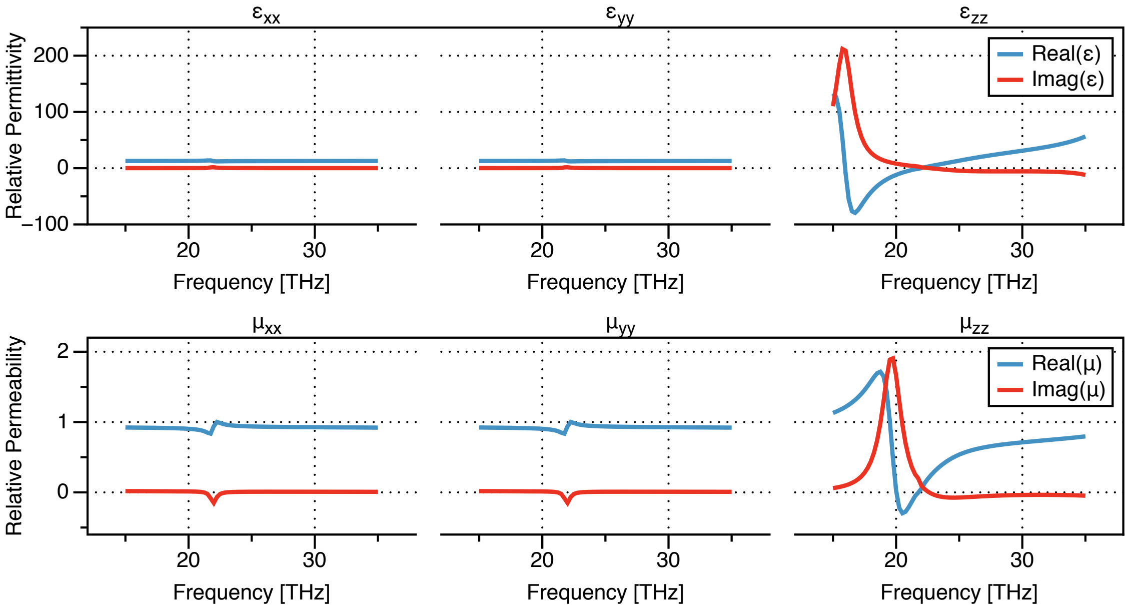

Figure 56. Permitivitty (top) and permeability (bottom) of the anisotropic plane.

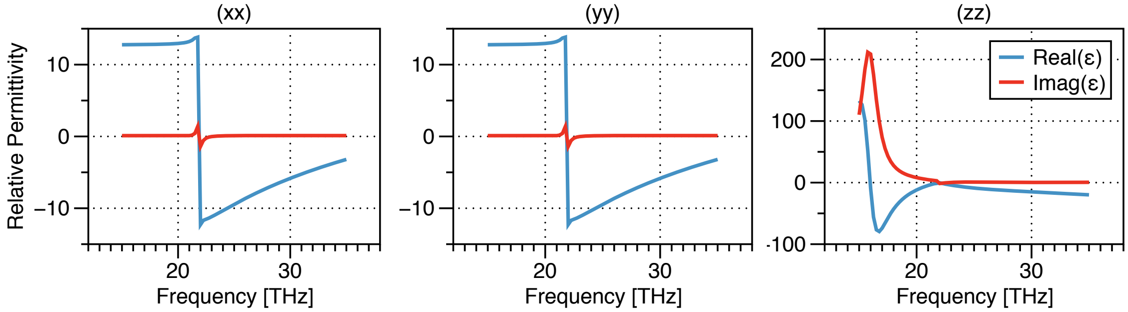

Figure 57. Permittivity extracted when the natural log function is used to invert the exponential. The extracted permeability shares similar characteristics.

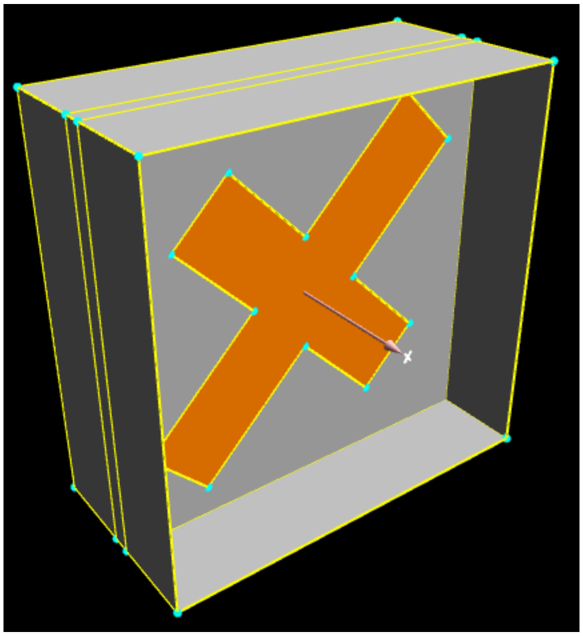

Figure 58. Geometry of tilted cross structure. The angle between the long portion of the cross and $\hat{z}$ is 45 degrees.

short axis is 750 nanometers long. Both strips are 50 nanometers thick. The entire structure is rotated about $\hat{x}$ by 45 degrees. The crosses are tiled in $\hat{x}$ and $\hat{y}$ with 500 nanometer periods in $\hat{x}$ and 1 micron periods in $\hat{y}$. The crosses are made of silver and are centered in a silicon substrate that is 1 micron thick.

The eigenvalues of the extracted $\tilde{\Delta}_{xx}$ and $\tilde{\Delta}_{xy}$ are shown in Figure 59. Because of the lack of symmetry in this problem, the two sets of eigenvalues are slightly different from one another. While the differences are not large, they are significant. One of the most obvious differences is the point where the imaginary portions of the eigenvalues cross $\pm\pi$. For the $\tilde{\Delta}_{xx}$ case, both cross at the same point, 34.69 THz. For the $\tilde{\Delta}_{xy}$ case, the two crossings happen at different points; λ_4 crosses $+i\pi$ at 35.35 THz, while λ_1 crosses $-i\pi$ at 33.81 THz. The permittivities and permeabilities extracted from the two $\tilde{\Delta}$ matrices is shown are Figures 60 and 61.

Generating the predicted reflection and transmitted fields from the extracted quantities demonstrates excellent agreement between the tensor-based model and the

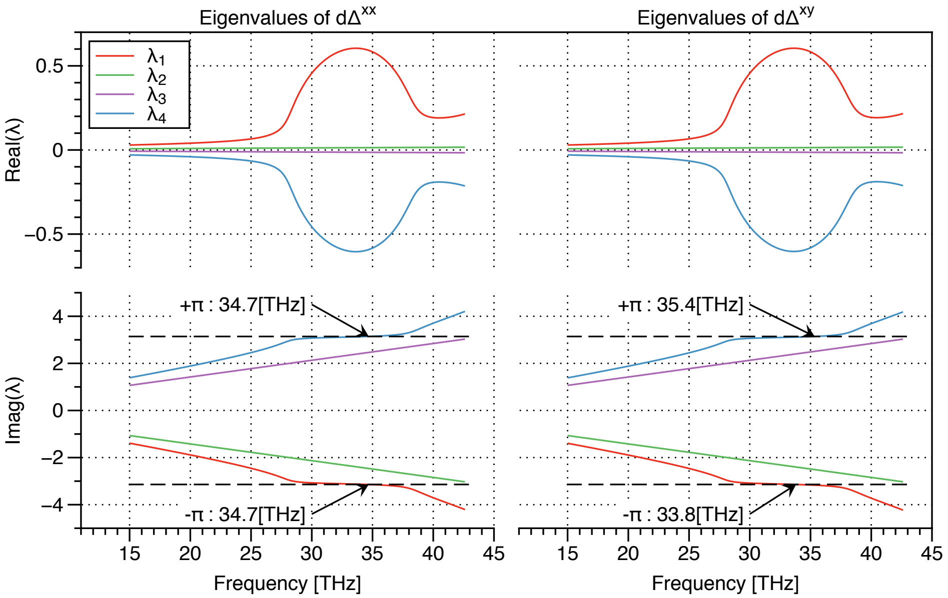

Figure 59. Eigenvalues of the tilted metal crosses.

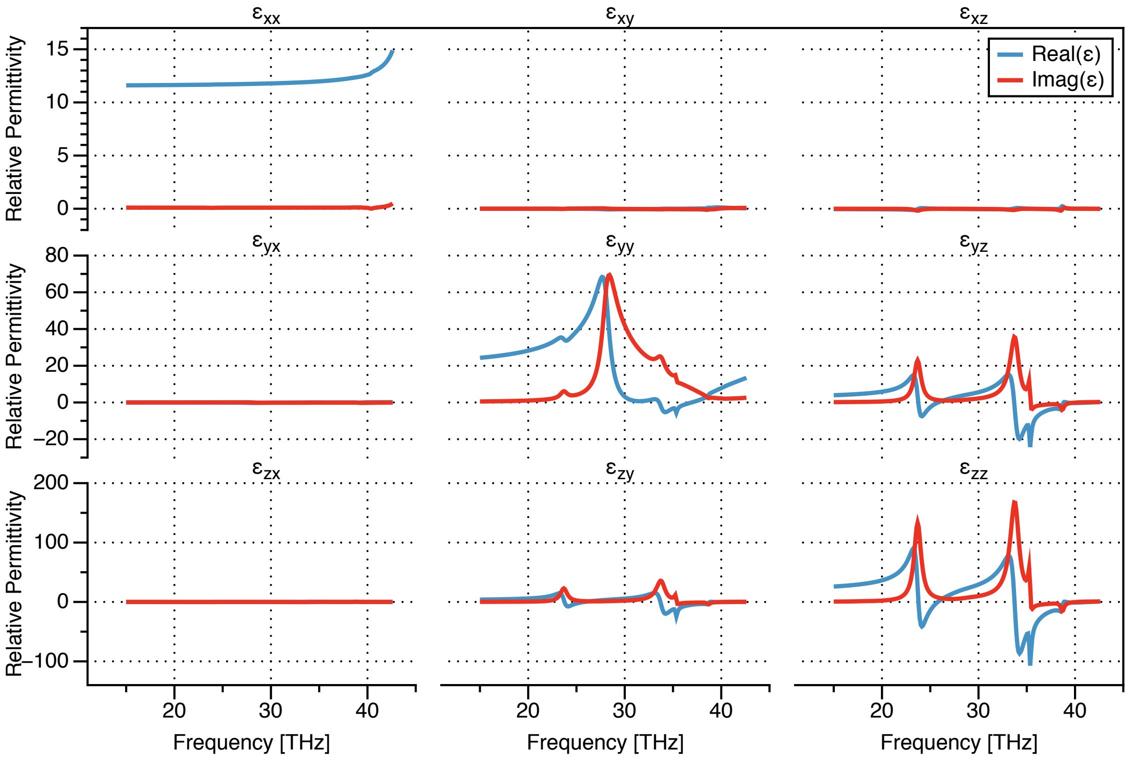

Figure 60. Permittivity tensor of the tilted metal crosses.

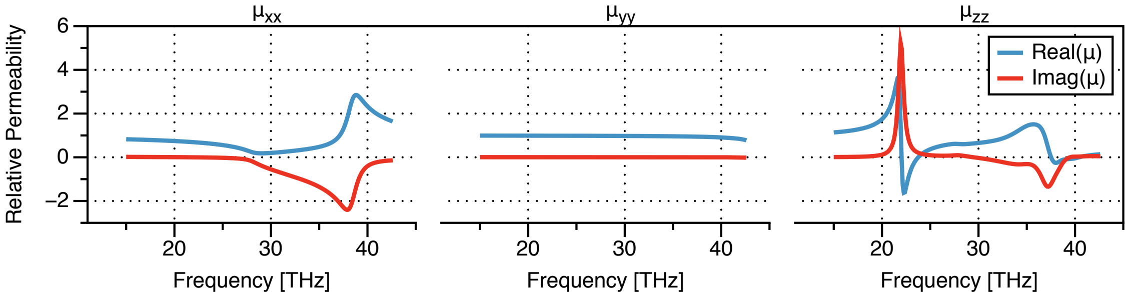

Figure 61. Diagonals of the permeability tensor of the tilted metal crosses. The off-diagonal elements are zero.

electromagnetic simulation. The error can be quantified by simulating the coefficients at various sample rotations, and comparing these numbers to the tensor-based predictions. The mean error for the polarization-preserving coefficients remains below 1% in all cases below 43 THz, while the cross-polarization coefficients remain below 2% over the same region. An example of the simulated and predicted fields is shown in Figure 62, while the mean field amplitude error over sample rotation as a function of frequency is shown in Figure 63.

5.5 Conclusion

An algorithm is proposed in this paper to enable the proper inversion of a matrix exponential within the PPTE technique. By extracting the eigenvalues and eigenvectors from the matrix $T_p(\omega)$, the correct root of the exponential can be chosen. From this, the correct matrix $\tilde{\Delta}(\omega)$ can be determined. Two assumptions are necessary for this process. These two assumptions are shown to be true in cases where the permittivities and permeabilities can be modeled using traditional models. Several simulations were presented to show that the assumptions hold true in practice, and can be used to extract meaningful information from the problem.

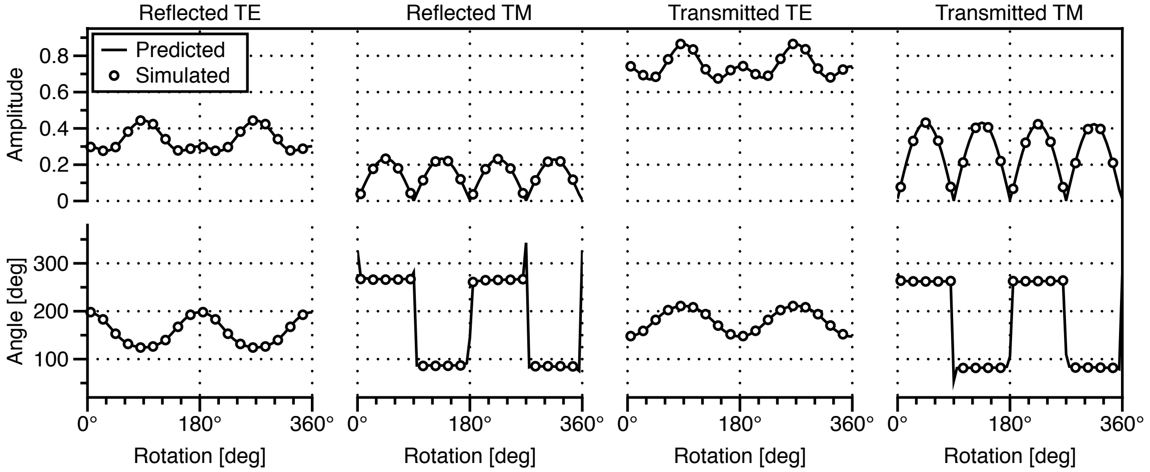

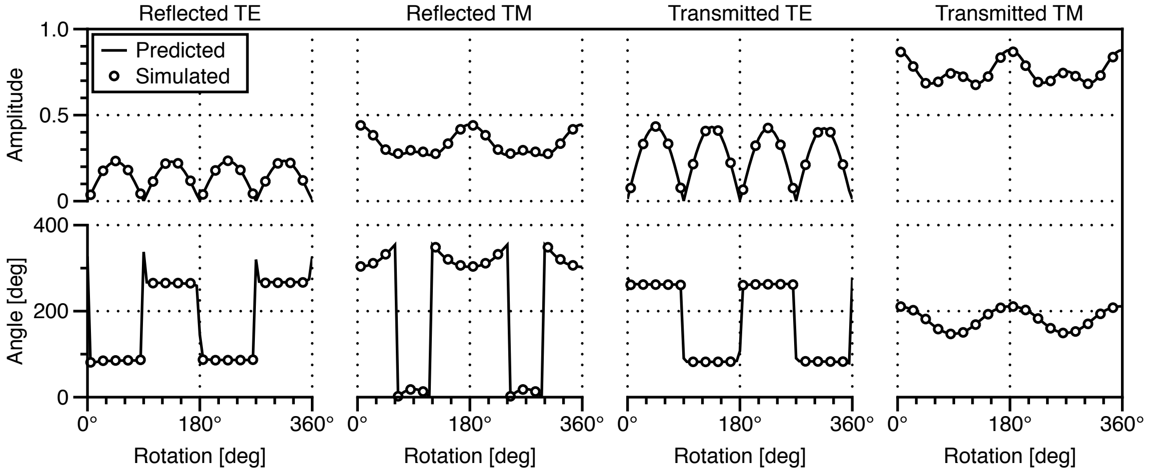

Figure 62. Simulated and predicted fields for tilted metal crosses. The TE fields are shown on top, while the TM fields are shown on the bottom.

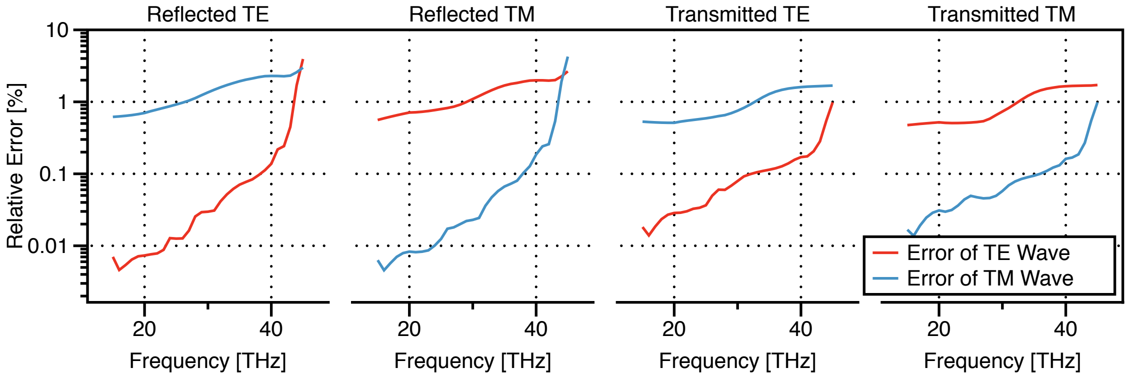

Figure 63. Mean relative error over sample rotation as a function of the simulation frequency.

VI. Examination of Geometric Metamaterial Properties

The PPTE technique allows for the extraction of the complete permittivity and permeability tensor from an anisotropic material. This provides much more information than other parameter extraction methodologies, such as ellipsometry. In this chapter, the underlying mechanics of the nanorods will be discussed. The nanorods have optical characteristics that have not been observed previously. One of the most notable findings is the wavelength dependent geometric transformations that is demonstrated by the material. This shows that these structures are capable of properties that are offered by few other materials, and can one day be used to create new materials for specific applications.

In ellipsometry, one of the underlying assumptions is that the permittivity tensor is a transformed diagonalized tensor [30,93,102]. This aligned tensor is then transformed by a tensor based on the physical geometry of the material into the permittivity tensor of the material [55]. This assumption is based on a simple geometric analysis of the scene [93], and used in an enormous quantity of work [28, 54, 76–78, 81]. Since PPTE extracts the entire permittivity tensor, this assumption is a testable hypothesis. The complete permittivity tensor can be diagonalized by extracting the eigenvalues and eigenvectors. This gives both the information about the diagonalized tensor as well as the tensor transformation. Comparing the tensor transformation to the classically assumed transformation allows for the following hypothesis to be tested: is the diagonalization of the permittivity tensor strictly a function of the material's geometry?

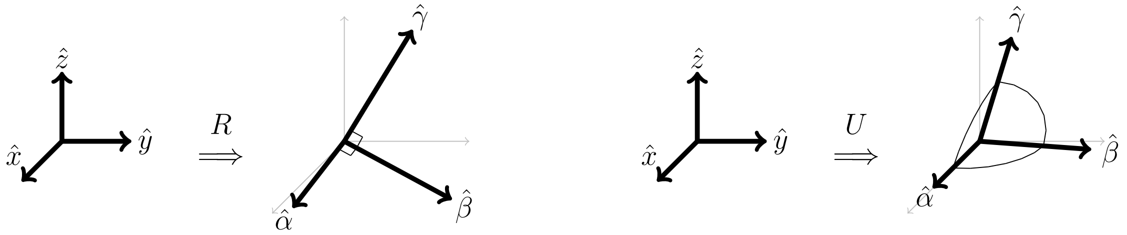

Figure 64. Examples of a rotational transformation (left) and triclinic transformation (right).

6.1 Theory

In “Spectroscopic Ellipsometry”, Fujiwara notes [30] that the permittivity tensor can be defined as

$$\boldsymbol{\epsilon} = R \begin{bmatrix} \epsilon_\alpha & 0 & 0 \\ 0 & \epsilon_\beta & 0 \\ 0 & 0 & \epsilon_\gamma \end{bmatrix} R^T \tag{264}$$

where R is a rotation matrix and ϵ_α, ϵ_β, and ϵ_γ are the principal permittivities. The matrix R is given as

$$R = \begin{bmatrix} \cos\psi_r & \sin\psi_r & 0 \\ -\sin\psi_r & \cos\psi_r & 0 \\ 0 & 0 & 1 \end{bmatrix} \begin{bmatrix} 1 & 0 & 0 \\ 0 & \cos\theta_r & \sin\theta_r \\ 0 & -\sin\theta_r & \cos\theta_r \end{bmatrix} \begin{bmatrix} \cos\phi_r & -\sin\phi_r & 0 \\ \sin\phi_r & \cos\phi_r & 0 \\ 0 & 0 & 1 \end{bmatrix} \tag{265}$$

where ψ_r, θ_r, and ϕ_r are $(z - x - z)$ Euler rotation angles. This presumes that the principal axes are perpendicular to one-another, which is a common assumption in many anisotropic materials. An example of this transformation is demonstrated in Figure 64.

Monoclinic and triclinic materials need an additional transformation to go from the principal permittivities to the permittivity tensor [77]. These terms come from the optical characteristics of crystals, which do not always have perpendicular optical axes. The extra transformation converts from perpendicular axes to axes that are not. The transformation U is defined as

$$U = \begin{bmatrix} \sin\beta_t & \frac{\cos\gamma_t - \cos\beta_t\cos\alpha_t}{\sin\beta_t} & 0 \\ 0 & \sqrt{\sin^2\alpha_t - \frac{\cos\gamma_t - \cos\beta_t\cos\alpha_t}{\sin\beta_t}} & 0 \\ \cos\beta_t & \cos\alpha_t & 1 \end{bmatrix} \tag{266}$$

where α_t, β_t, and γ_t are the internal angles of the material, also shown in Figure 64. Note that the rotation and triclinic transformations are not exclusive and can be used simultaneously, and are in many publications [76–78].

These transformations, either implicitly or explicitly, are assumed to not be wavelength dependent. Schmidt et al. in a section of "Ellipsometry of the Nanoscale" explicitly notes [55] "[...] A real valued rotation matrix A independent of wavelength can be found [...]". In a later section, the monoclinic and triclinic transformation is treated similarly to be non-spectral. If these transformations are geometric in nature, why would they change as a function of frequency?

The PPTE technique does not make this assumption, which allows the technique to better examine this assumption and test it for accuracy within the realm of metamaterial design. Wavelength independent transformations, even for complex materials, seems like a reasonable assumption, and is certainly one that has been traditionally assumed. Most, if not all, ellipsometry based papers have been written where metamaterials are treated as homogenous biaxial layers where the permittivity tensor is calculated as a diagonalized tensor modified by some wavelength independent transformation [28, 77, 81]. PPTE performs this backwards: the permittivity tensor is found, and can then be diagonalized to find the transformation.

A permittivity tensor $\boldsymbol{\epsilon}$ will have eigenvalues ϵ_α, ϵ_β, and ϵ_γ with eigenvectors ν_α,

ν_β, and ν_γ. This gives

$$\boldsymbol{\epsilon} = \begin{bmatrix} \nu_\alpha | \nu_\beta | \nu_\gamma \end{bmatrix} \begin{bmatrix} \epsilon_\alpha & 0 & 0 \\ 0 & \epsilon_\beta & 0 \\ 0 & 0 & \epsilon_\gamma \end{bmatrix} \begin{bmatrix} \nu_\alpha | \nu_\beta | \nu_\gamma \end{bmatrix}^{-1}. \tag{267}$$

If the permittivity tensor is three principal permittivities modified by a rotation and triclinic transformation, then

$$RU \begin{bmatrix} \epsilon_\alpha & 0 & 0 \\ 0 & \epsilon_\beta & 0 \\ 0 & 0 & \epsilon_\gamma \end{bmatrix} (RU)^{-1} = \boldsymbol{\epsilon} \tag{268}$$

which implies

$$\begin{bmatrix} \nu_\alpha | \nu_\beta | \nu_\gamma \end{bmatrix} = RU. \tag{269}$$

This relationship between the eigenvectors of the permittivity tensor and the transformation between the permittivity tensor and the principal permittivities allows for the testing of the underlying assumptions. If the only transformations present are the rotation transformation and the monoclinic/triclinic transformation, then firstly the eigenvectors will be purely real, and secondly the eigenvectors will not be wavelength dependent. Note that from a practical standpoint, eigenvalues and eigenvectors are calculated spectrally independent from one another, and may change positions depending on the wavelength. Similarly to Chapter V, the continuity of the principal permittivities will be assumed to differentiate between the eigenvalues and eigenvectors.

6.2 Simulations

All of the simulations carried out in this section were performed using the FLO_K platform. For more details, see Section 4.7.

6.2.1 Split-ring Resonators.

Split-ring resonators are a iconic feature within the landscape of metamaterials [17, 31, 84]. They have been deeply studied in a number of different places, and are well known for having spectral anisotropic features in both the permittivity and permeability tensors [18, 50]. Here, a split ring resonator made of silver [70] with the geometry shown in Figure 65 will be analyzed. Note that the gap of the rings are purposefully moved away from the tiling axes by 30 degrees to analyze the effects of rotating the structure. The forward and back-traveling cases are evaluated at sample rotations of 0 and 90 degrees (which is along the tiling axes) at a 5 degree angle of incidence, relative to normal. The frequency in the simulation is varied from 15 to 45 THz.

When the angle of the ring's rotation ϕ_{SRR} is 0, the permittivity and permeability tensors are predictably diagonalized, which has been studied extensively [31]. Rotating the rings introduces new optical activity in the ϵ_{xy} and ϵ_{yx} tensor elements, which is predicted using the rotational transformations in Equation (265). The permittivity tensor is shown in Figure 66. Similar activity was observed in the μ_{xy} and μ_{yx} elements, although to a much smaller degree. The μ_{xx} and μ_{yy} elements are very similar leading to a less obvious effect. Still, it has been observed that the same rotational transformations are necessary here for both the permittivity and permeability tensor.

An eigenvalue/eigenvector analysis is used to find the principal permittivities for the rotated simulation. The eigenvectors are then analyzed and compared to the ideal case as proposed by classical ellipsometric and crystallographic models. The results

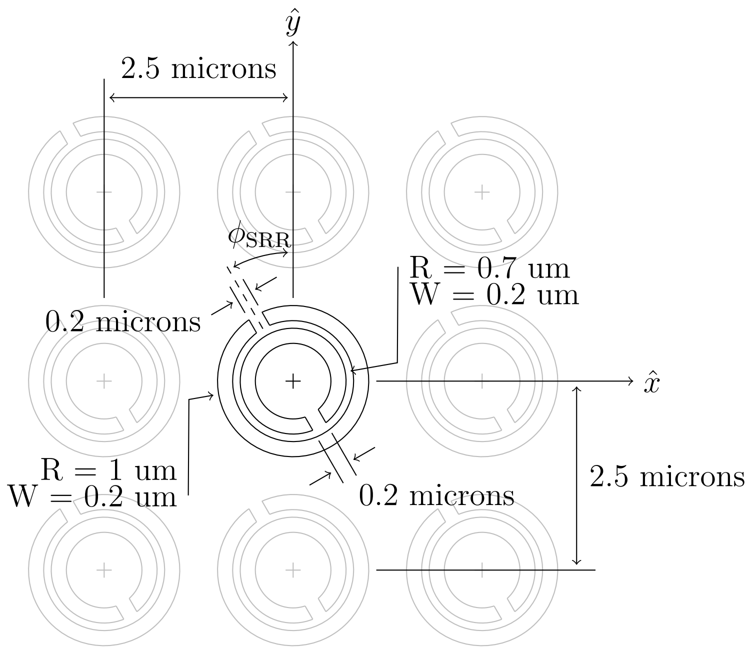

Figure 65. Split Ring Resonator geometry. The conductive strips are made of silver and are 0.1 microns thick. They are contained within a silicon layer of the same thickness.

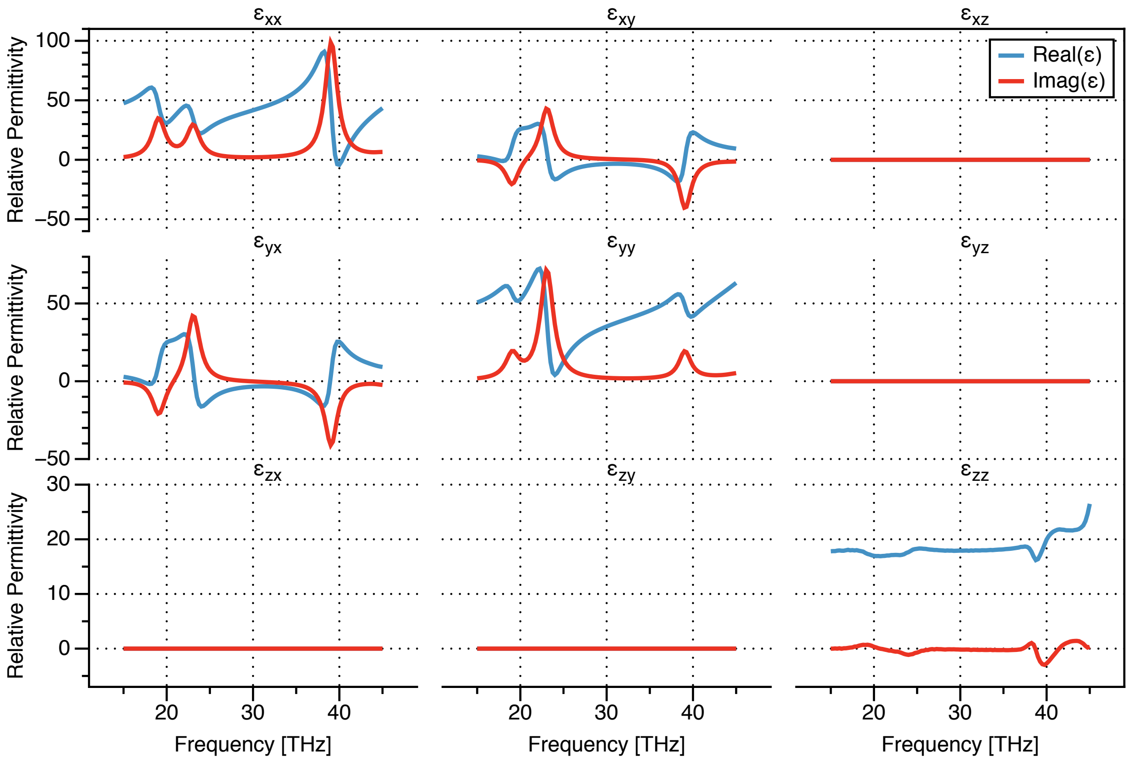

Figure 66. Permittivity tensor of the rotated split-ring resonators. The ϵ_{xy} and ϵ_{yx} tensor elements show a high degree of optical activity, which is predicted by the previously stated assumptions regarding material design.

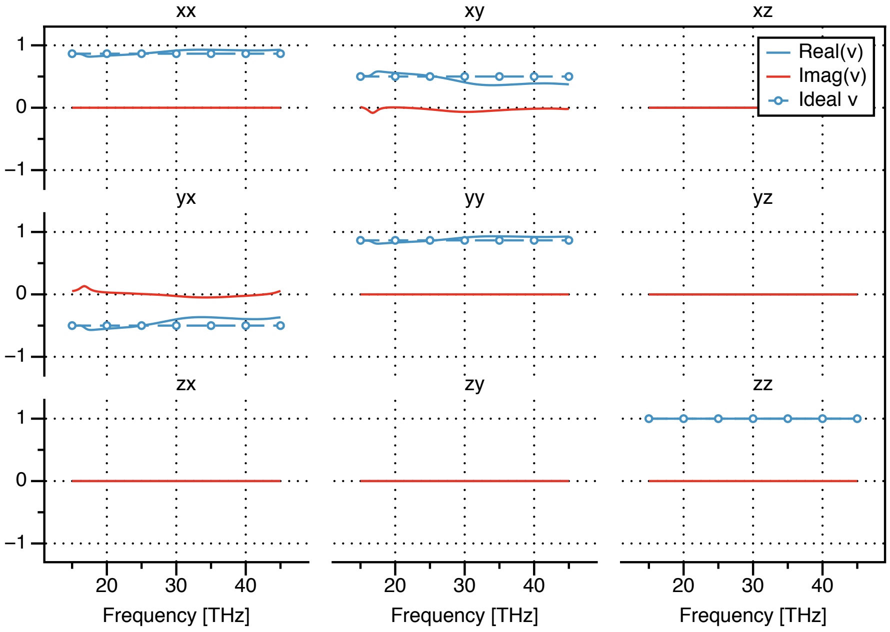

Figure 67. Eigenvectors of ϵ of the split-ring resonator when $\phi_{\mathbf{SRR}} = 30°$.

shown in Figure 67 show that the eigenvalues do have some amount of wavelength dependent structure to them. However, the average of the eigenvectors is very similar to the predicted transformation matrices. Using the model to predict the permittivity tensor demonstrates good agreement between the two. The principle permittivities are shown in Figure 68, while the measured/predicted permittivity tensors are compared in Figure 69. Similar simulations carried out at $\phi_{\mathrm{SRR}} = 15$ and 45 degrees demonstrate similar trends. The 45 degree case exhibited eigenvalues that were much closer to the ideal rotation matrix than either the 15 or 30 degree case.

There are several observations that should be made from this. The first is that this eigenvalue matrix in the case of a material rotated in-plane does change slightly as a function of frequency. In order to exactly return to the original permittivity tensor, the exact eigenvectors must be used. Utilizing a rotational matrix instead of the actual eigenvalues arrives at an approximation of the permittivity tensor. It is a good approximation, which results in a average relative error of about 10% in the predicted cross-polarization fields, and 1% in the same-polarization fields.

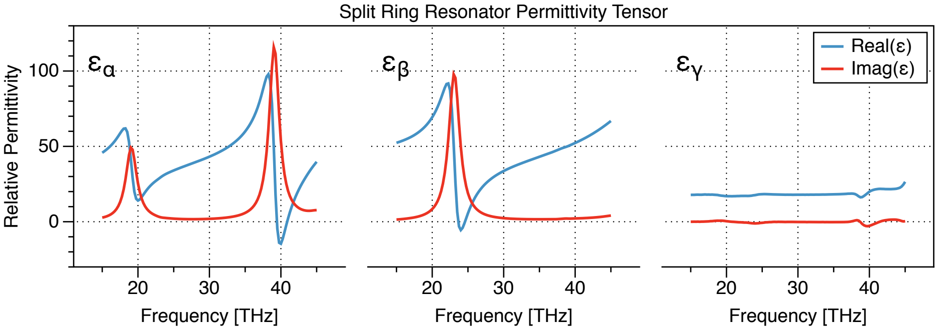

Figure 68. Principle permittivities of the rotated split-ring resonators. Increasing the rotation angle from 0 to 45 degrees increased the frequency of the second peak in ϵ_α.

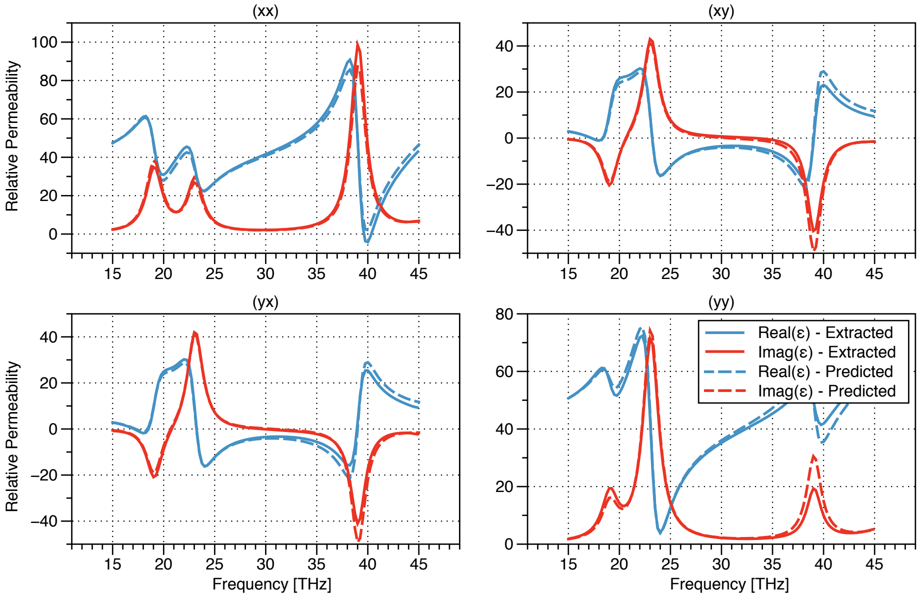

Figure 69. Comparison of extracted and predicted xx, xy, yx, and yy tensor elements for the $\phi_{\mathbf{SRR}}$ = 30 degree case. The zz elements were identical, while the xz, yz, zx, and zy elements are zeros.

Another observation is the presence of a small imaginary component in the eigenvectors. This is something that is not allowed in the classical material models, and for good reason. An imaginary component would imply that the real portion of the diagonalized permittivity could become the imaginary part upon applying the transformation, and vice-versa. This seems to run contradictory to classical electromagnetics. However, this term is small to the point of insignificance; assuming a rotational transformation gives an excellent approximation of the overall permittivity tensor for this particular case. The error induced by using an ideal rotation transformation in determining the permittivity tensor is around 5%, averaged over the frequency range examined here.

6.2.2 Tilted Nanorods.

One of the materials previously examined in Chapter IV was the tilted-nanorod sample. This is a small silver [70] rod 500-nanometers long and 100-nanometers wide suspended in a silicon substrate. The rod is tilted such that the length of the rod is in the $\hat{y} \cdot \hat{z}$ plane at 45 degrees from the z axis. The permittivity of the rod is taken to be that of silver. Due to the tilt of the rod, it should have optical activity in the yz and zy tensor elements. The geometry of the rod is displayed in Figure 70, while an example of the unit-cell of this material is shown in Figure 71. The extracted permittivity tensor is shown in Figure 72.

Two separate methods were used to extract the eigenvalues and eigenvectors; the first allowed only real eigenvectors while the second allowed for complex eigenvectors. The rotation used implies that the eigenvalues should be $[1, 0, 0]$, $\sqrt{2}/2 \times [0, 1, 1]$ and $\sqrt{2}/2 \times [0, -1, 1]$ for all frequencies, but this is not what is observed. The eigenvectors approximate this at the lower frequencies, but quickly diverge. The yy, yz, zy, and zz tensor elements of the eigenvector matrix are shown in Figure 73. The real eigenvector

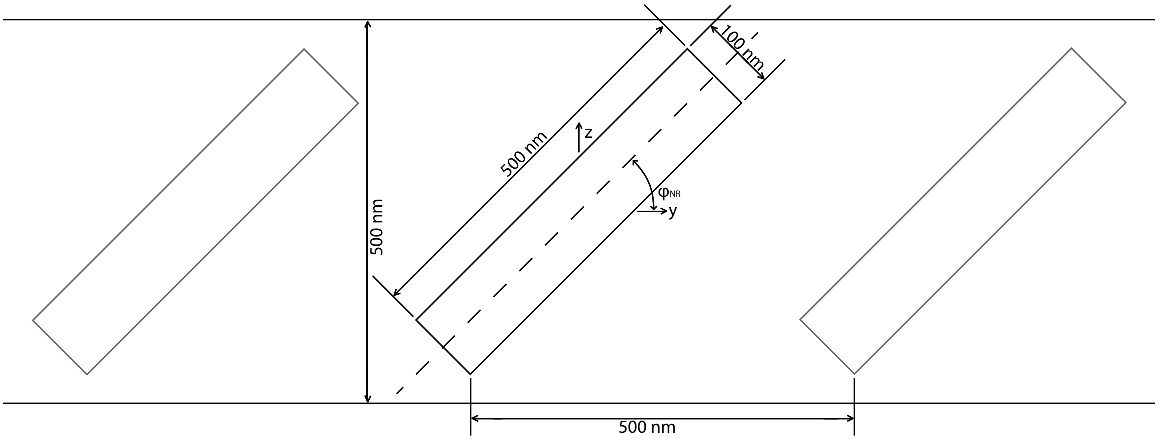

Figure 70. Diagram of nanorod geometry. The nanorods are cylindrical, and are spaced 200 nanometers apart in $\hat{x}$.

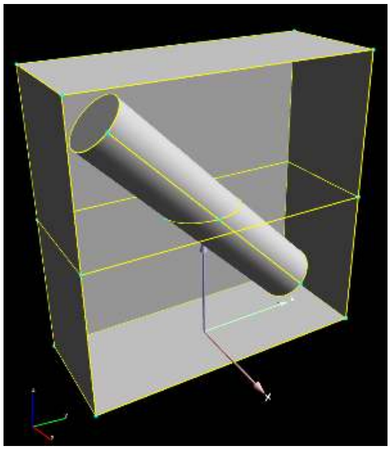

Figure 71. Picture of tilted nanorod. The rod is 500 nanometers long, 100 nanometers in diameter, and tilted at 45 degrees about the x axis. The unit cell has dimensions 200 nanometers in $\hat{x}$ by 500 nanometers in $\hat{y}$, and the substrate is 500 nanometers thick in $\hat{z}$.

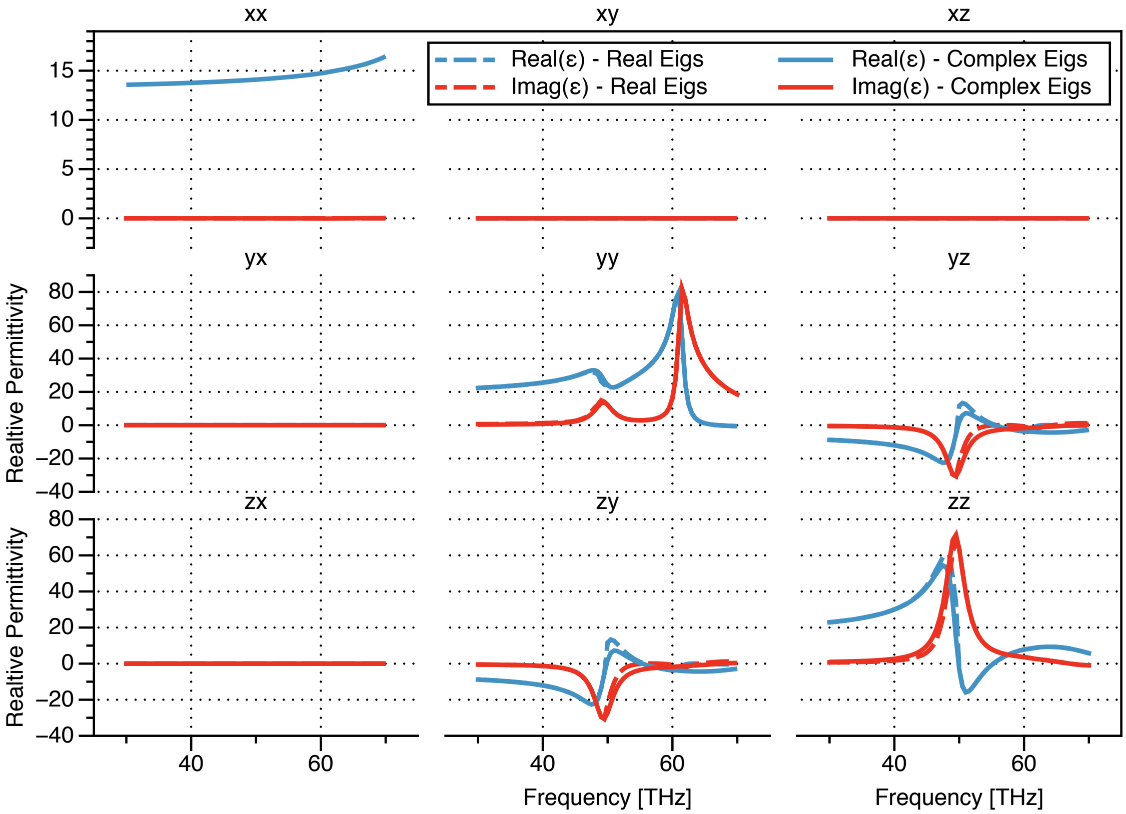

Figure 72. Comparison of extracted and predicted tensor elements for the rotated nanorod.

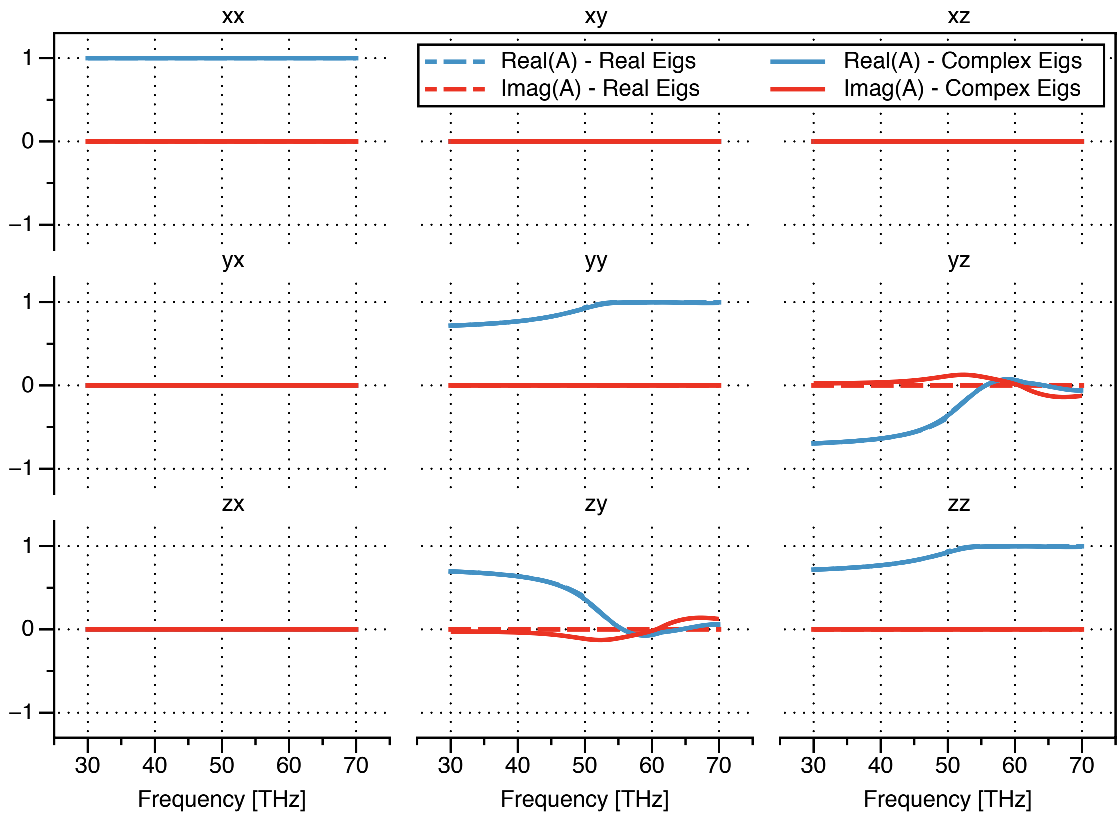

Figure 73. The eigenvector matrix of the rotated nanorod. The strictly real eigenvectors are very close to the complex eigenvalues, which is why the two are difficult to distinguish.

analysis failed to properly reconstruct the extracted tensor, and gave predictably worse results than the complex eigenvector analysis, as shown in Figure 72. The strictly real eigenvector analysis lead to significant error in the off-diagonal tensor terms compared to the complex eigenvector analysis, which resulted in a perfect recreation of the tensor. This error is shown in Figure 74.

This analysis demonstrates a few things. The first is that there is a very clear wavelength dependence to the eigenvectors of the permittivity tensor for the rotated material. It is fairly clear that the permittivity tensor cannot be reconstructed with any spectrally constant matrices; metamaterial design needs to include frequency dependent transformations to accurately model the permittivity tensor of the material. The nature of these transformations is something that will need to be explored in

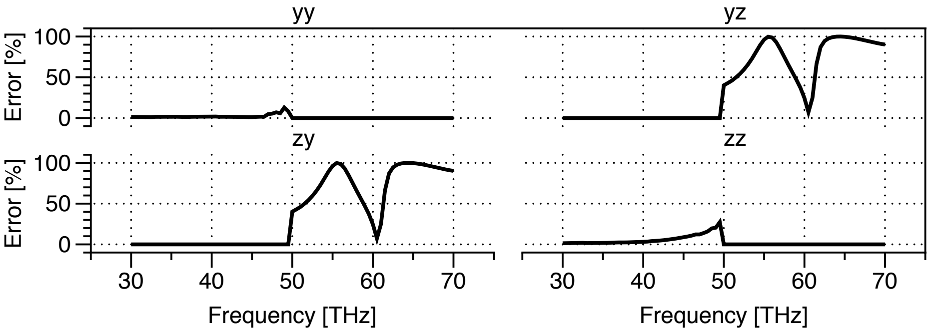

Figure 74. Error between extracted permittivity tensor and permittivity tensor calculated using strictly real eigenvectors.

detail. If the previous transformations were allowed to be spectrally dependent, they could reconstruct the permittivity tensor with reasonable accuracy. In this case, the average error would be around 10% over the frequency range examined here.

The other observation is that the transformation matrix needs to have imaginary components to correctly reconstruct the permittivity tensor. There is no way to arrive at the exact permittivity tensor without a complex transformation matrix. One possible explanation of the physics of an imaginary eigenvalue involves understanding the meaning of eigenvectors in general. The eigenvalues and eigenvectors are determined by solving $\boldsymbol{D} = \epsilon \boldsymbol{E}$ for the case where $\boldsymbol{D}$ is parallel to $\boldsymbol{E}$, that is

$$\boldsymbol{D} = \epsilon_{\{\alpha,\beta,\gamma\}} \boldsymbol{E}. \tag{270}$$

This implies that the displacement field $\boldsymbol{D}$ is related to the electric field $\boldsymbol{E}$ by the scalar $\epsilon_{\{\alpha,\beta,\gamma\}}$. Then, a complex eigenvector would imply that at least one component of the electric field requires a complex component in order to be considered an eigenvalue. Complex electric field amplitudes were discussed in Section 2.2.1, and simply indicates that the wave exists with a phase shift. Therefore, in this situation, the complex eigenvector implies that one component of the electric field requires some phase shift to be considered an eigenvector.

6.3 Conclusion

Here, some of the underlying assumptions regarding metamaterial design have been identified and tested. Rotating simple structures leads to complex electromagnetic behaviors that can be eventually used to design more complex materials. It was previously assumed that the principle permittivities can be transformed by simple geometric transformations to arrive at a material's permittivity tensor. This is an appropriate assumption for materials rotated in-plane, as demonstrated by the rotated split-ring resonator. For out-of-plane rotations, this assumption is a poor one; there is a clear frequency dependence to the geometric transformations to convert between the two permittivity expressions. In addition, the eigenvalue/eigenvector analysis demonstrates an imaginary portion of this transformation, which indicates a difficulty in modeling metamaterials using traditional analysis techniques.

VII. Conclusion

7.1 Research goals and accomplishments

Nanorods are complex metamaterials which demonstrate unique optical properties not observed in many other materials. The materials demonstrate three unique optical axes that are not aligned with the laboratory frame of reference, which makes both the measuring and the modeling of these structures very difficult. This research was begun in an attempt to understand the relationship between the underlying physical structures of these samples and the optical characteristics that they possess.

Generalized Ellipsometry was used to measure the optical characteristics of the two tilted nanorod samples. The first sample featured short, wide nanorods, which demonstrated a large difference between the index of refraction between optical axes. The second sample featured long, narrow nanorods, which demonstrated much less of a difference at long wavelengths, and very different behaviors at the shorter wavelengths. This demonstrates that the underlying physical structure of the materials, the only significant difference, is responsible for the optical characteristics.

These materials are too complex to model using closed-form electromagnetics, but can be easily modeled using computational electromagnetics. From these simulations, the effective material parameters can be determined. The sample complexities, namely the misalignment of the optical axes, prevents previous effective material parameter techniques from being used. The Permittivity and Permeability Tensor Extraction (PPTE) technique was created as part of my research to identify the effective material parameters of complex materials. PPTE allowed for a closer examination of the underlying assumptions of metamaterials, which are shown to be more complex than initially assumed by the community as a whole. In addition, the underlying mechanics of PPTE allows for reflected and transmitted fields of a material to be determined, which allows the utility of these effective parameters to be determined.

7.2 Overview of research

The research began with the study of the optical properties of two unique samples that Dr. Sarangan and Dr. Shah of the University of Dayton presented to Dr. Marciniak's research group. The samples consisted of silver tilted-nanorods on a substrate that were each created under different conditions and thus had unique geometric characteristics [14]. Assuming the accuracy of the previously used models, such as the Traditional Anisotropic Bruggeman Effective Medium Approximation [76–78], there should have been little difference between the two samples. This is not what was observed; the two materials exhibited very different optical characteristics. These differences were due to the underlying material structure [14].

The differences between these two samples also presented difficulties in comparing their optical properties. Traditionally, these materials are discussed using the standard crystalline terminology, in which the optical axes are distinguished based on the amplitude of their indices. This can create confusion while discussing similar materials in which the direction of the optical axes would differ. I proposed a naming scheme for these axes based instead on their morphological characteristics, which makes it easier to compare optical properties between similar materials [14].

Measuring the nanorods proved to be challenging as well. The field of Generalized Ellipsometry, especially as it pertains to highly anisotropic ellipsometry, is a relatively new field with sparse literature surrounding it [54, 71, 79]. The measurements of these materials have been researched by only a few groups, which makes the contributions of these measurements a significant advancement to the field. In addition, this research compared additional optical properties that were not previously considered, namely the absorptance as a function of direction. The absorptance measurements proves that these are interesting materials which can be created to have unique orientation dependent optical properties [14].

This research achieved the first portion of the goal, which was to determine the optical characteristics of these two silver-nanorod based samples. Measuring the optical properties of nanorods is an active field of research [76–78], and this work was able to contribute my measurements to the scientific community [14]. Future researchers examining these structures will be able to reference this paper and have a better method of communicating their results and identifying unique optical properties.

The second part of the goal was to model the permittivities of the nanorods. This was not previously possible due to the limitations of the previous techniques [64, 83, 99]. The field of anisotropic effective material parameters is also a young field of research. A review article from 2011 [86] notes that at the time of writing, there were two basic problems in the field: the extracted parameters were not a complete description of the operation of the materials, and the effective material parameters were difficult to verify as an appropriate description of the material.

Since the publication of this review article, research performed by other groups has continued to explore anisotropic effective material parameters [64, 83, 99]. However, the proposed techniques are limited in their scope; these techniques are only capable of extracting the effective parameters if the optical axes of the material are aligned with the laboratory frame of reference. This assumption immediately prevents using these techniques with the tilted nanorods. Since then, one paper has been published which shows that it can theoretically extract effective material parameters for materials where the optical axes are in the plane of the material [67], but even this is fairly constricting, as it cannot analyze materials tilted out of plane, such as the tilted nanorods which prompted this research.

This research removed these previous restrictions and demonstrated that these effective material parameters can communicate relevant information about the materials. The PPTE technique is a new process than can transform between simulated fields and effective material parameters under a small set of reasonable assumptions. The anisotropic effective material parameters can be extracted using PPTE regardless of the orientation of the optical axes. The technique utilizes a small set of assumptions that are viable in the vast majority of circumstances. By extracting the complete permittivity and permeability tensor, the optical characteristics of nearly any structure without optical rotation can be measured [13].

In addition, the PPTE technique gives a clear path from these effective parameters to the predicted electromagnetic fields. The predicted fields can be compared against the simulated fields to establish the validity and utility of the effective material parameters. This is one of the first times the utility of the effective material parameters has been measured. In the cases examined here, the extracted parameters prove to be very useful. The simulated case of aligned anisotropic inclusions demonstrate less than 1% error between the simulated and predicted fields. The simulated case of tilted nanorods, a significantly more complex material, demonstrated errors of less than 10% for the cross-polarization wave, and less than 2% for the same polarization. These calculations can be carried out orders-of-magnitudes faster than the necessary computational electromagnetic simulations [13].

The PPTE technique did require one step that is particularly challenging, which is the inversion of a matrix exponential operation. The mathematical basis of this process has been analyzed in Chapter VI in depth. There is a set of assumptions that, if true, would allow for the exponential function to be a fully invertible operation. The physics of the application within the PPTE shows that these assumptions are reasonable for the problem at hand, which allows for this process to be used here. The inversion of this operation allows PPTE to be used in a wider range of applications than would be otherwise possible, which further extends its use as a general purpose tool for extracting effective material parameters.

PPTE is the tool that allows for the examination of the theoretical characteristics of tilted nanorods and other complex metamaterials, as well as the underlying presumptions in the physics of tilted and non-aligned materials. One of these assumptions is that the permittivities of the optical axes is related to the permittivity of the material tensor via simple geometric transformations. This is an assumption that can now be tested using PPTE by geometrically manipulating these structures, and comparing the operations necessary to diagonalize their tensors with the appropriate geometric transformation.

PPTE was used to demonstrate that for materials rotated in plane, the expected geometric transformations convert between the diagonalized permittivities and the permittivity tensor very well, with an error of a few percent. A similar analysis on a material rotated out-of-plane, the tilted nanorods in this case, show that this assumption is a poor one; the operations necessary to diagonalize the tensor exhibit a high degree of frequency dependence. This is a property of metamaterials that has not been shown before, as the necessary tools for performing this analysis did not exist until PPTE was created.

7.3 Research utility and implications

The research performed and presented here is useful to the metamaterial community as a whole. My contributions can be broadly parsed into two sets: the contributions offered by the measurements and the contributions offered by the modeling. While these groups are traditionally separated, the research performed and presented in this document will be beneficial to both groups.

The measurements performed on the tilted-nanorod samples is of benefit to the materials community as a whole for several reasons. There is only a small collection of these measurements presented in literature today [16, 38, 71, 74, 75, 77, 78, 85]; my research contributes significantly to this small collection [14]. Performing experiments utilizing Generalized Ellipsometry is very difficult, which explains the small group of relevant research today. My research is unique in that it is a comparative study between two materials which demonstrates clear differences. These measurements also demonstrate interesting optical features, such as directional absorptance, which may be of interest to people designing new materials for specific uses. This research also provides a more clear language for communicating about these complex materials. Special care must be taken with non-aligned anisotropic materials to communicate their optical properties properly due to the confusion that can be accidentally induced by using traditional crystallographic terms.

The modeling of these materials is an even greater contribution to the metamaterial community as a whole. The field of anisotropic effective material parameters currently lacks an effective way to extract material parameters for the generalized case. PPTE is a new technique which extracts a more complete picture of the effective material parameters from a small set of simulations. It provides the means to quickly, easily, and accurately determine these parameters. In addition, PPTE provides a clear and straightforward means to move from effective parameters to predicted optical properties, which offers the opportunity to both verify the utility of the parameters and identify areas of interest before performing simulations or experiments [13].

These effective material parameters have been shown to accurately predict complex material behavior. This is one of the first times where this predictive capability has been demonstrated [13]. The aligned case presented here demonstrates less than 1% error between the prediction and the simulation. The more complex material demonstrated less than 10% error for the cross-polarization waves, and less than 2% for the same-polarization waves. These predictions were carried out in a fraction of the time as the simulations that they were compared against [13]. This clearly demonstrates the utility of these effective material parameters. Using a small set of simulations, the optical activity of a wide range of angles can be quickly, easily, and accurately determined. This can aid in both accurately describing these materials, as well as indicate areas of interest from a small set of data.

The matrix exponential inversion operation provided a way to use PPTE in a larger variety of circumstances. The ability of the method for addressing the multiple roots of the exponential has been clearly demonstrated. PPTE was used to examine some of the previous presuppositions regarding the operation of metamaterial. It was demonstrated here that the geometric manipulations previously used are good assumptions when materials are modified in-plane [30, 93, 102]. A clear wavelength dependence was demonstrated for materials rotated out-of-plane, such as the tilted-nanorods examined here.

All of this research will eventually lead to a greater understanding of optical metamaterials. The measurements clearly demonstrate that the titled-nanorods can be exhibit interesting optical properties. The PPTE technique allows for simulations to easily extract these same properties. Together, this can provide a platform for better engineering materials to accomplish specific design goals.

7.4 Future Research

Over the course of this research, many research opportunities were identified. Some of them fell outside of the scope of this research, while others were found too late to address adequately in this document. Some of them are now possible because of the research presented here.

7.4.1 Ellipsometry and Laboratory Measurements.

One such opportunity for future research is to reanalyze the ellipsometric data taken of the nanorods using oscillator based models. The data examined and discussed here was done by fitting the best n and k to each frequency. Recreating these results with oscillators could give a greater physical insight into the structure by demonstrating resonant wavelengths and other physical characteristics. In addition, this would make it much easier to create ellipsometric models using some of the other layer permittivity models, such as the TAB-EMA layer.

The original goal of this research was to begin with a sample, model it, and learn how the model works to create a new sample. The new sample would have engineered characteristics to demonstrate the ability of the material to be designed for specific applications. This original goal was not realized, as many of the tools necessary to perform the work simply did not exist. Now, PPTE is capable of extracting the required permittivities and permeabilities. Analyzing nanorods, or similar structures for the purpose of engineering them, and then physically creating them would be an excellent project that is now possible.

The PPTE technique is predicated on the knowledge of the absolute phase of the fields. Ellipsometry provides the relative phase between fields. The relative fields can be converted to absolute fields if the reference phase was known. Perhaps there is some way to assume the reference phase and find the absolute phase from the ellipsometric information? Or, perhaps, the absolute phase is not even needed? Answering these questions in a theoretical setting may lead to new ellipsometric techniques that can directly extract the information that is desired from a material.

7.4.2 Permittivity and Permeability Tensor Extraction.

The space in which to make predictions encompasses angle of incidence, sample rotation, wavelength, and polarization. In my research, I made the choice to simulate and compare data solely as a function of sample rotation. The possibility of comparing simulated and predicted fields as a function of angle of incidence was omitted from this work. Some of my initial results showed that the predictive power of the Homogenous Biaxial Layer Approximation (HBLA) model does not operate as well in this dimension as it does in sample rotation. Future research could identify the strengths and weakness of the HBLA model as it relates to angle of incidence and other dimensions. Furthermore, it could offer guidance to future researchers regarding where to make measurements for extracting effective material parameters for different uses.

The matrix Δ_B, the matrix from which the effective material parameters are extracted, is a simplified case of a complete solution. The simplified case was chosen as a result of its utility for the nanorods, but there are some materials that cannot be modeled with this simplified solution. Specifically, materials with optoelectric coupling terms cannot be modeled using this Δ_B. This matrix can be rederived to use the optoelectric terms instead of the complete permittivity and permeability tensor, which provides opportunities for measuring other metamaterials. It would be beneficial to develope a document or series of documents describing different Δ_B matrices and their applications.

Computational electromagnetic simulations require large computational resources and a lot of time. The simulation assumes an infinite grid of perfectly created structures with no variations, which is unrealizable within a physical setting. Simulating real structures is impractical, but the effects of these imperfections is something that could be determined. Understanding these effects would better allow for real material design.

7.4.3 Metamaterial Design.

Reading through the literature on ellipsometry and metamaterials, I did not locate any instances in which the transformations necessary to diagonalize the permittivity and permeability tensors could be a function of wavelength. It has been demonstrated in Chapter VI that this is in fact the case. The exact nature of these transformations is not known, and is a topic of future research. The imaginary portion of the eigenvalues in particular is very important, as it must have some physical significance.

One surprising feature identified while examining eigenvalues is the behavior demonstrated in Figure 59. Notice the presence of a large bump in the real part of the eigenvalue around the location of the $\pm i\pi$ point while the imaginary part flattens out dramatically. The $\pm i\pi$ point has a physical interpretation, being effectively the half-wave interference point of the material. However, in other materials, notably isotropic and simple anisotropic samples, these effects are not present. This suggests that the effect is due to some structural resonance around this half-wave point. Future research could explore the implications and significance of this spectral feature, and perhaps offer ways to utilize this for future materials.

The final research possibility that I would like to mention regards a design paper on the nanorods. There is definitely a relationship between the physical characteristics and the optical properties of the materials. It may be best to focus on performance characteristics instead of permittivities. For example, perhaps a metamaterial exhibits a characteristic peak at a certain wavelength, or a large absorptance at a certain angle. These features provide the most meaningful metrics, and could be the focus of new research.

Appendix A. Unit conversion and list of equations

A.1 Spectral Quantities

$$\lambda = \frac{1.24}{E} = \frac{300}{f} \tag{271}$$

λ - Wavelength (microns)	E - Energy (electron-volts)	f - Frequency (THz)
2 μm	0.62 eV	150 THz
5 μm	0.25 eV	60 THz
10 μm	0.124 eV	30 THz
25 μm	0.05 eV	12 THz

Table 3. Wavelength/energy/frequency conversion table.

A.2 Polarization

Perpendicular Polarization	S-pol	TE polarization
Parallel Polarization	P-pol	TM polarization

Table 4. Polarization terms.

A.3 Optical characteristics

$$\epsilon_1 + i\epsilon_2 = n^2 - k^2 - i2nk \tag{272}$$

where $\epsilon = \epsilon_1 + i\epsilon_2$.

$$n + ik = \frac{1}{\sqrt{2}} \left\{ \left[(\epsilon_1^2 + \epsilon_2^2) + \epsilon_1 \right]^{1/2} + i \left[(\epsilon_1^2 + \epsilon_2^2) - \epsilon_1 \right]^{1/2} \right\} \tag{273}$$

Material	Complex Index	Permittivity
Silver (1 μm)	0.21+7.0i	-49 - 2.98i
Vacuum	1	1
Silver (2 μm)	1.064+14.4i	-206 - 30.6i
Silicon (IR)	3.32	11
Split Ring Resonator peak (23 THz)	5.7 + 0.29i	33 + 3.3i
Nanorod peak (49.5 THz)	6.6 + 5.4i	14.2 + 71i
Nanorod peak (61.5 THz)	8.6 + 4.7i	81 + 52i
Split Ring Resonator peak (38 THz)	9.4 + 8.3i	21 + 156i

Table 5. Common material indexes and permittivities.

A.4 Sections to Equations Quick-reference

	First page	First equation	Last page	Last equation
Section 2.2	Pg. 16	(4)	Pg. 42	(67)
Section 2.3	Pg. 46	(69)	Pg. 67	(130)
Section 3.3	Pg. 75	(131)	Pg. 78	(136)
Section 4.3	Pg. 97	(137)	Pg. 103	(152)
Section 4.3.2	Pg. 104	(153)	Pg. 106	(164)
Section 4.4	Pg. 107	(165)	Pg. 109	(173)
Section 4.5	Pg. 110	(174)	Pg. 111	(177)
Section 4.6	Pg. 111	(178)	Pg. 117	(229)
Section 4.7	Pg. 118	(231)	Pg. 119	(240)
Section 5.1	Pg. 136	(241)	Pg. 139	(249)
Section 5.2	Pg. 140	(250)	Pg. 141	(254)
Section 5.3	Pg. 143	(255)	Pg. 146	(263)
Section 6.1	Pg. 157	(264)	Pg. 159	(269)

Table 6. List of sections and the equations they contain.

Appendix B. Solving for the permittivities of the Traditional Anisotropic Bruggeman Effective Medium Approximation

There are practical difficulties in solving the three equations composing the TAB-EMA formalism. For an EMA with two components, the equation will have two solutions. This is easy to see after simplifying the equation by multiplying the equation to remove the denominators. Which solution, then, is the correct solution? Some authors have suggested using bounds in order to ascertain which solution is correct [73]. One of the better ways I have found to identify the proper solution is similar to the approach taken by Rouseel et al in his work [73]. In his paper (which is focused on isotropic Bruggeman formalisms), he normalizes the quadratic equation in such a way that the correct solution is always found using a single root of the quadratic formula.

This approach can be easily extended to the TAB equations. The TAB equations are

$$f_a \frac{\epsilon_a - \epsilon_j}{\epsilon_j + L_j(\epsilon_a - \epsilon_j)} + f_b \frac{\epsilon_b - \epsilon_j}{\epsilon_j + L_j(\epsilon_b - \epsilon_j)} = 0 \tag{274}$$

where $j \in \{\alpha, \beta, \gamma\}$. It can be assumed, without loss of generality, that

$$0 \leq \angle(\epsilon_a) \leq \angle(\epsilon_b) \leq \pi.$$

This can be rewritten in the form of equation (1) of reference [57],

$$(1 - f_b) \frac{\epsilon_a - \epsilon_j}{\epsilon_a + L'_j \epsilon_j} = f_b \frac{\epsilon_j - \epsilon_b}{\epsilon_b + L'_j \epsilon_j} \tag{275}$$

where $L'_j = (1 - L_j)/L_j$. The only difference between this and the cited equation (other than the subscripts) is change from 2 to L'_j. This equation can be simplified into the following quadratic equation:

$$L'_j \epsilon_j^2 - \left[f_b \left(L'_j + 1 \right) \left(\epsilon_b - \epsilon_a \right) + L'_j \epsilon_a - \epsilon_b \right] \epsilon_j - \epsilon_a \epsilon_b = 0. \tag{276}$$

Following with Roussel et al's work, a new variable, z_j will be introduced:

$$z_j \equiv \epsilon_j (\epsilon_a \epsilon_b)^{-1/2}. \tag{277}$$

Now, the equation above can be rewritten as

$$L'_j z_j^2 - \left[f_b \left(L'_j + 1 \right) \left(p^{-1} - p \right) + L'_j p - p^{-1} \right] z - 1 = 0 \tag{278}$$

where $p \equiv \sqrt{\epsilon_a / \epsilon_b}$. This is further simplified as

$$L'_j z_j^2 - b_j z - 1 = 0 \tag{279}$$

where

$$b_j = \left[f_b \left(L'_j + 1 \right) \left(p^{-1} - p \right) + L'_j p - p^{-1} \right]. \tag{280}$$

The reasons for this normalization are not obvious to most. The advantage provided here comes from the work of Viète [97], which provides the following relationship between the two roots of the above equation:

$$z_{j,1} z_{j,2} = \frac{-1}{L'_j}. \tag{281}$$

This implies that the angle of the product of the two roots will be $-\pi$ when L'_j is greater than 0. Note that L'_j was defined as $(1 - L_j)/L_j$. The values of L_j are confined by the relationship

$$L_\alpha + L_\beta + L_\gamma = 1, \tag{282}$$

and are all positive. Therefore, L'_j must always be greater than zero, and this relationship between the angle of the product of the two roots will be $-\pi$. Therefore, $\angle z_{j,1} = \pi - \angle z_{j,2}$. From here, the rest of Roussel et al's derivation can be followed, and it can be shown that

$$z_j = \frac{b + \sqrt{b^2 + 4L'_j}}{2L'_j} \tag{283}$$

is the correct solution. The permittivity is then

$$\epsilon_j = z_j \sqrt{\epsilon_a \epsilon_b}. \tag{284}$$

This guarantees that ϵ_j will have a positive imaginary component, which is required for a physical solution.

Appendix C. Physics of the Eigenvalues of The Δ Matrix

C.1 Physics

The physics of the matrix Δ_B dictate that there is something interesting about its eigenvalues and eigenvectors. The matrix Δ_B comes about as the solution to this particular problem: what is the relationship between the fields in a material and the change of the fields in a material? The solution to that is straightforward:

$$\frac{\partial}{\partial z}\begin{bmatrix} E_x(z) \\ E_y(z) \\ H_x(z) \\ H_y(z) \end{bmatrix} = \frac{\omega}{c}\Delta \begin{bmatrix} E_x(z) \\ E_y(z) \\ H_x(z) \\ H_y(z) \end{bmatrix}. \tag{285}$$

Now, eigenvectors are special vectors that have their directionality preserved upon some transformation. The eigenvalues are then the relationship in amplitudes between the original vector and its transformed counterpart. This implies that, if the E and H vector above is an eigenvector, that the change in the vector is a scaled version of the original vector. Going back to basic calculus, this means that over some infinitesimally small distance, the new vector will be the same as the old one increased slightly by a scaled version of the same vector. Therefore, an eigenvector of the Δ matrix is a set of E and H fields that is not changed by the material. Since the collection of fields is not changed by the material, it must be the same on the top and the bottom, different only in amplitudes.

And what are the differences in amplitudes? Equation (247) gives us that the eigenvalues of the entire layer are the exponential of the eigenvalues of the matrix Δ_B. Explicitly, that relationship is

$$\Lambda_k = \exp\left(\lambda_k\right) \tag{286}$$

where Λ_k is the eigenvalue of the matrix T_p and λ_k is the eigenvalue of the scaled matrix $\tilde{\Delta}$. All of the eigenvalues in different cases examined in Chapter V show that there are two eigenvalues with positive real values, and two with negative real values. This has important physical significance to this problem. The eigenvalues with negative real portions indicate that the strength of the wave is decaying through the material. Given some combination of E and H fields on one side of the layer, the E and H fields on the opposite side are exactly the same, only reduced (and with a phase shift caused by the imaginary portion of the eigenvalue). Likewise, the eigenvalues with positive real components indicate that the wave is actually increasing with amplitude through the layer. As this is an impossibility in the simple structures examined here, it must be concluded that this is actually the back-traveling solution: the E and H fields on the bottom decay as they reach the top.

The physical interpretation of the eigenvalue solutions can be used to strengthen the claim that there will always be four eigenvalues to the matrix Δ_B. The assumption can now shift from "It is likely that there are four based on the simpler cases" to "There will be four if light can be transmitted through (a) in both directions with (b) two unique polarization states in each case". This is actually very similar to one of the underlying assumptions of the entire process (there is transmitted light, and there are two unique polarization states). Unfortunately, it does little to prove that the imaginary portion of the eigenvalue will tend towards zero in any and all cases.

Although, the imaginary portion does have physical significance as well. The imaginary portion refers to the phase shift between the top of a layer and the bottom of a layer. As the wavelength decreases, the phase-shift will decrease between the two sides, as the longer wavelengths will have less space to change phases. Again, this does not prove that the imaginary portion will go towards zero, but hopes to offer insight into why the assumption that it does is a good one.

Appendix D. Determinant and Eigenvalues of the Δ matrix

D.1 Determinant

Given a matrix Δ of the form

$$\Delta_B = \begin{bmatrix} -K_{xx}\dfrac{\epsilon_{zx}}{\epsilon_{zz}} & K_{xx}\left[\dfrac{\mu_{yz}}{\mu_{zz}} - \dfrac{\epsilon_{zy}}{\epsilon_{zz}}\right] & \mu_{yx} - \dfrac{\mu_{yz}\mu_{zx}}{\mu_{zz}} & \mu_{yy} - \dfrac{\mu_{yz}\mu_{zy}}{\mu_{zz}} - \dfrac{K_{xx}^2}{\epsilon_{zz}} \\ 0 & -K_{xx}\dfrac{\mu_{xz}}{\mu_{zz}} & \dfrac{\mu_{xz}\mu_{zx}}{\mu_{zz}} - \mu_{xx} & \dfrac{\mu_{xz}\mu_{zy}}{\mu_{zz}} - \mu_{xy} \\ \dfrac{\epsilon_{yz}\epsilon_{zx}}{\epsilon_{zz}} - \epsilon_{yx} & \dfrac{K_{xx}^2}{\mu_{zz}} + \dfrac{\epsilon_{yz}\epsilon_{zy}}{\epsilon_{zz}} - \epsilon_{yy} & -K_{xx}\dfrac{\mu_{zx}}{\mu_{zz}} & K_{xx}\left[\dfrac{\epsilon_{yz}}{\epsilon_{zz}} - \dfrac{\mu_{zy}}{\mu_{zz}}\right] \\ \epsilon_{xx} - \dfrac{\epsilon_{xz}\epsilon_{zx}}{\epsilon_{zz}} & \epsilon_{xy} - \dfrac{\epsilon_{xz}\epsilon_{zy}}{\epsilon_{zz}} & 0 & -K_{xx}\dfrac{\epsilon_{xz}}{\epsilon_{zz}} \end{bmatrix}, \tag{287}$$

the determinant can be found by using several simplifications and submatrices. To begin, the matrix will be rewritten as a 2 by 2 block matrix

$$\Delta_B = \left[\begin{array}{cc|cc} A_{11} & A_{12} & B_{11} & B_{12} \\ 0 & A_{22} & B_{21} & B_{22} \\ \hline C_{11} & C_{12} & D_{11} & D_{12} \\ C_{21} & C_{22} & 0 & D_{22} \end{array}\right] = \begin{bmatrix} A & B \\ C & D \end{bmatrix}. \tag{288}$$

Sylvester [5] shows the following:

$$\det \begin{bmatrix} A & B \\ C & D \end{bmatrix} = \det(AD - BC) \tag{289}$$

where A, B, C, and D are all square matrices, and A and B commute.

As the problem is presently presented, this is not the case for the matrix Δ_B. However, performing two row-reductions can make blocks A and D diagonal, which would make them commute. The submatrices in the second and fourth quadrant can be reduced to diagonal matrices. Assuming neither A_{22} nor D_{22} are equal to zero, then

$$\begin{bmatrix} 1 & -\frac{A_{12}}{A_{22}} & & \\ & 1 & & \\ & & 1 & -\frac{D_{12}}{D_{22}} \\ & & & 1 \end{bmatrix} \left[\begin{array}{cc|cc} A_{11} & A_{12} & B_{11} & B_{12} \\ 0 & A_{22} & B_{21} & B_{22} \\ \hline C_{11} & C_{12} & D_{11} & D_{12} \\ C_{21} & C_{22} & 0 & D_{22} \end{array}\right] = \left[\begin{array}{cc|cc} A_{11} & 0 & \tilde{B}_{11} & \tilde{B}_{12} \\ 0 & A_{22} & B_{21} & B_{22} \\ \hline \tilde{C}_{11} & \tilde{C}_{12} & D_{11} & 0 \\ C_{21} & C_{22} & 0 & D_{22} \end{array}\right] \tag{290}$$

therefore

$$\Delta = \begin{bmatrix} 1 & \frac{A_{12}}{A_{22}} & & \\ & 1 & & \\ & & 1 & \frac{D_{12}}{D_{22}} \\ & & & 1 \end{bmatrix} \left[\begin{array}{cc|cc} A_{11} & 0 & \tilde{B}_{11} & \tilde{B}_{12} \\ 0 & A_{22} & B_{21} & B_{22} \\ \hline \tilde{C}_{11} & \tilde{C}_{12} & D_{11} & 0 \\ C_{21} & C_{22} & 0 & D_{22} \end{array}\right] \tag{291}$$

where

$$\begin{bmatrix} \tilde{B}_{11} \\ \tilde{B}_{12} \end{bmatrix} = \begin{bmatrix} B_{11} \\ B_{12} \end{bmatrix} - \frac{A_{12}}{A_{22}} \begin{bmatrix} B_{21} \\ B_{22} \end{bmatrix} \tag{292}$$

$$\begin{bmatrix} \tilde{C}_{11} \\ \tilde{C}_{12} \end{bmatrix} = \begin{bmatrix} C_{11} \\ C_{12} \end{bmatrix} - \frac{D_{12}}{D_{22}} \begin{bmatrix} C_{21} \\ C_{22} \end{bmatrix}. \tag{293}$$

The determinant of Δ_B is now the product of the determinants of the two matrices of Equation (291). The determinant of the first is 1, which simplifies the problem slightly.

Now, the submatrices of Equation (291) have been simplified and rewritten such that A and B commute. Therefore,

$$\begin{aligned} \det \Delta &= \det \left(AD - BC\right) \\ &= \det \left(\begin{bmatrix} A_{11} & \\ & A_{22} \end{bmatrix} \begin{bmatrix} D_{11} & \\ & D_{22} \end{bmatrix} - \begin{bmatrix} \tilde{B}_{11} & \tilde{B}_{12} \\ B_{21} & B_{22} \end{bmatrix} \begin{bmatrix} \tilde{C}_{11} & \tilde{C}_{12} \\ C_{21} & C_{22} \end{bmatrix} \right) \\ &= -\det \left(\left[\begin{array}{c|c} \tilde{B}_{11}\tilde{C}_{11} + \tilde{B}_{12}C_{21} - A_{11}D_{11} & \tilde{B}_{11}\tilde{C}_{12} + B_{21}C_{22} \\ \hline B_{21}\tilde{C}_{11} + B_{22}C_{21} & B_{21}\tilde{C}_{12} + B_{22}C_{22} - A_{22}D_{22} \end{array} \right] \right). \end{aligned} \tag{294}$$

From this, the determinant can be trivially found. The un-tilded elements can be found by corresponding Equations (287) and (288), while the tilded elements can be found using Equations (292) and (293).

Note the complexity of Equation (294). None of the terms can be assumed to be zero without knowing more about the problem at hand. The tilded-terms themselves are fairly complex without including them in Equation (294). For example, the ratio A_{12}/A_{22} is equal to

$$\frac{A_{12}}{A_{22}} = \frac{\epsilon_{zy}}{\epsilon_{zz}}\frac{\mu_{zz}}{\mu_{xz}} - \frac{\mu_{yz}}{\mu_{zz}}, \tag{295}$$

which makes $\tilde{B}_{11}$

$$\tilde{B}_{11} = \mu_{yx} - \frac{\mu_{yz}\mu_{zx}}{\mu_{zz}} - \left[\frac{\epsilon_{zy}}{\epsilon_{zz}}\frac{\mu_{zz}}{\mu_{xz}} - \frac{\mu_{yz}}{\mu_{zz}}\right]\left[\frac{\mu_{xz}\mu_{zx}}{\mu_{zz}} - \mu_{xx}\right] \tag{296}$$

which offers little in the way of physical insight into the problem.

D.2 Eigenvalues

The eigenvalues of Δ_B can be found by solving the problem $\det(\Delta - \lambda I) = 0$ for λ. Knowing the determinant, or at least how to easily find the determinant, aids in finding an equation for these values. Now, starting with

$$\Delta - \lambda I = \left[\begin{array}{cc|cc} A_{11}-\lambda & A_{12} & B_{11} & B_{12} \\ 0 & A_{22}-\lambda & B_{21} & B_{22} \\ \hline C_{11} & C_{12} & D_{11}-\lambda & D_{12} \\ C_{21} & C_{22} & 0 & D_{22}-\lambda \end{array}\right], \tag{297}$$

the same partial diagonalization above can be performed again, with slightly different values.

$$\Delta - \lambda_k I = \begin{bmatrix} 1 & \frac{A_{12}}{A_{22}-\lambda_k} & & \\ & 1 & & \\ & & 1 & \frac{D_{12}}{D_{22}-\lambda_k} \\ & & & 1 \end{bmatrix} \left[\begin{array}{cc|cc} A_{11}-\lambda_k & 0 & \breve{B}_{11}(\lambda_k) & \breve{B}_{12}(\lambda_k) \\ 0 & A_{22}-\lambda_k & B_{21} & B_{22} \\ \hline \breve{C}_{11}(\lambda_k) & \breve{C}_{12}(\lambda_k) & D_{11}-\lambda_k & 0 \\ C_{21} & C_{22} & 0 & D_{22}-\lambda_k \end{array}\right] \tag{298}$$

where

$$\begin{bmatrix} \breve{B}_{11}(\lambda) \\ \breve{B}_{12}(\lambda) \end{bmatrix} = \begin{bmatrix} B_{11} \\ B_{12} \end{bmatrix} - \frac{A_{12}}{A_{22}-\lambda} \begin{bmatrix} B_{21} \\ B_{22} \end{bmatrix} \tag{299}$$

$$\begin{bmatrix} \breve{C}_{11}(\lambda) \\ \breve{C}_{12}(\lambda) \end{bmatrix} = \begin{bmatrix} C_{11} \\ C_{12} \end{bmatrix} - \frac{D_{12}}{D_{22}-\lambda} \begin{bmatrix} C_{21} \\ C_{22} \end{bmatrix}. \tag{300}$$

Now, the determinant is

$$\det(\Delta - \lambda I) = \det\left(\begin{bmatrix} A_{11}-\lambda & \\ & A_{22}-\lambda \end{bmatrix} \begin{bmatrix} D_{11}-\lambda & \\ & D_{22}-\lambda \end{bmatrix} - \begin{bmatrix} \breve{B}_{11}(\lambda) & \breve{B}_{12}(\lambda) \\ B_{21} & B_{22} \end{bmatrix} \begin{bmatrix} \breve{C}_{11}(\lambda) & \breve{C}_{12}(\lambda) \\ C_{21} & C_{22} \end{bmatrix} \right) \tag{301}$$

To find the eigenvalues, simply set the above equation equal to zero and solve for the (presumably) four values of λ.

This is clearly a very difficult task. Each of the terms is made of up sums and products, and one or two divisions, of different tensor elements. Each of the breve terms include λ_k in a denominator, as well as twice as many tensor elements as the non-breve values. While the eigenvalues can be determined in this manner, it is clearly not only exceedingly difficult, but not the least bit advantageous. The complexity of the solution guarantees that there is little to no physical insight to be gained from determining them in this form.

Bibliography

1. "JA Woollam Co", 2006.
2. "Interstitial Oxygen: SunEdison", November 2013. URL `http://sunedisonsilicon.com/index.php?view=Interstitial-Oxygen`.
3. "Dictionary.com Unabridged". Apr 2015. URL `http://dictionary.reference.com/browse/anisotropy`.
4. Abdulhalim, I. "Analytic propagation matrix method for linear optics of arbitrary biaxial layered media". *Journal of Optics A: Pure and Applied Optics*, 1(5):646, 1999.
5. Akritas, Alkividias G, Evgania K Akritas, and Genadii I Malaschonok. "Various proofs of Sylvester's (determinant) identity". *Mathematics and Computers in Simulation*, 42(4):585–593, 1996.
6. Arevalo, S, C Atwood, P Bell, TD Blacker, S Dey, D Fisher, DA Fisher, P Genalis, J Gorski, A Harris, et al. "A new DoD initiative: the Computational Research and Engineering Acquisition Tools and Environments (CREATE) program". *Journal of Physics: Conference Series*, volume 125, 012090. IOP Publishing, 2008.
7. Aspnes, DE. "Approximate solution of ellipsometric equations for optically biaxial crystals". *JOSA*, 70(10):1275–1277, 1980.
8. Aspnes, DE and AA Studna. "High precision scanning ellipsometer". *Applied Optics*, 14(1):220–228, 1975.
9. Aspnes, DE, JB Theeten, and F Hottier. "Investigation of effective-medium models of microscopic surface roughness by spectroscopic ellipsometry". *Physical Review B*, 20(8):3292, 1979.
10. Azzam, Rasheed MA and Nicholas Mitchell Bashara. *Ellipsometry and polarized light*. North-Holland. sole distributors for the USA and Canada, Elsevier Science Publishing Co., Inc., 1987.
11. Balanis, Constantine A. *Advanced engineering electromagnetics*, volume 20. Wiley New York, 1989.
12. Beavers, Kelsey R, Nicole E Marotta, and Lawrence A Bottomley. "Thermal Stability of Silver Nanorod Arrays". *Chemistry of Materials*, 22(7):2184–2189, 2010.
13. Benson, Michael, Alex Knisley, Michael Marciniak, Michael Seal, and Augustine Urbas. "Permittivity and Permeabilitiy Tensor Extraction Technique for Arbitrary Anisotropic Materials". *[Accepted] IEEE Photonics Journal*, 2015.

14. Benson, Michael, Piyush Shah, Michael Marciniak, Andrew Sarangan, and Augustine Urbas. "Optical Characterization of Silver Nanorod Thin Films Grown Using Oblique Angle Deposition". *Journal of Nanomaterials*, 2014, 2014.

15. Berreman, Dwight W. "Optics in stratified and anisotropic media: 4× 4-matrix formulation". *JOSA*, 62(4):502–510, 1972.

16. Beydaghyan, Gisia, Cristina Buzea, Yan Cui, Chelsea Elliott, and Kevin Robbie. "Ex situ ellipsometric investigation of nanocolumns inclination angle of obliquely evaporated silicon thin films". *Applied Physics Letters*, 87(15):153103–153103, 2005.

17. Bilotti, Filiberto, Alessandro Toscano, and Lucio Vegni. "Design of spiral and multiple split-ring resonators for the realization of miniaturized metamaterial samples". *Antennas and Propagation, IEEE Transactions on*, 55(8):2258–2267, 2007.

18. Bonache, Jordi, Ignacio Gil, Joan Garcia-Garcia, and Ferran Martin. "Novel microstrip bandpass filters based on complementary split-ring resonators". *Microwave Theory and Techniques, IEEE Transactions on*, 54(1):265–271, 2006.

19. Born, Max and Emil Wolf. *Principles of optics: electromagnetic theory of propagation, interference and diffraction of light*. Cambridge University Press, 1999.

20. Bruggeman, DAG. "Effective medium model for the optical properties of composite materials". *Ann. Phys. Leipzig*, 24:636, 1935.

21. Cardoso, João R. "An explicit formula for the matrix logarithm". *arXiv preprint math/0410556*, 2004.

22. Cardoso, Joao R, Charles S Kenney, and F Silva Leite. "Computing the square root and logarithm of a real P-orthogonal matrix". *Applied numerical mathematics*, 46(2):173–196, 2003.

23. Cheng, Sheung Hun, Nicholas J Higham, Charles S Kenney, and Alan J Laub. "Approximating the logarithm of a matrix to specified accuracy". *SIAM Journal on Matrix Analysis and Applications*, 22(4):1112–1125, 2001.

24. De Feijter, JA, J Benjamins, and FA Veer. "Ellipsometry as a tool to study the adsorption behavior of synthetic and biopolymers at the air–water interface". *Biopolymers*, 17(7):1759–1772, 1978.

25. Doyle, William T. "The Clausius-Mossotti problem for cubic arrays of spheres". *Journal of Applied Physics*, 49(2):795–797, 1978.

26. Drude, Paul. "Ueber die Gesetze der Reflexion und Brechung des Lichtes an der Grenze absorbirender Krystalle". *Annalen der Physik*, 268(12):584–625, 1887.

27. Ellipsometry, Spectroscopic. “Optical characterization of epitaxial semiconductor layers”. 1996.

28. Elman, JF, J Greener, CM Herzinger, and B Johs. “Characterization of biaxially-stretched plastic films by generalized ellipsometry”. *Thin Solid Films*, 313:814–818, 1998.

29. Erman, M, JB Theeten, P Chambon, SM Kelso, and DE Aspnes. “Optical properties and damage analysis of GaAs single crystals partly amorphized by ion implantation”. *Journal of applied physics*, 56(10):2664–2671, 1984.

30. Fujiwara, Hiroyuki. *Spectroscopic ellipsometry: principles and applications*. John Wiley & Sons, 2007.

31. Gay-Balmaz, Philippe and Olivier JF Martin. “Electromagnetic resonances in individual and coupled split-ring resonators”. *Journal of applied physics*, 92(5):2929–2936, 2002.

32. Goldstein, Dennis H. *Polarized Light, revised and expanded*, volume 83. CRC Press, 2003.

33. Goodman, Joseph W. “Statistical optics”. *New York, Wiley-Interscience, 1985, 567 p.*, 1, 1985.

34. Hardy, WN and LA Whitehead. “Split-ring resonator for use in magnetic resonance from 200–2000 MHz”. *Review of Scientific Instruments*, 52(2):213–216, 1981.

35. Hasar, UC. “Elimination of the multiple-solutions ambiguity in permittivity extraction from transmission-only measurements of lossy materials”. *Microwave and Optical Technology Letters*, 51(2):337–341, 2009.

36. Havrilla, Michael. “The Effects of Symmetry on Material Property Tensors”, May 2014. Material Measurment Working Group Information Meeting.

37. Hecht, E. *Optics*. Pearson education. Addison-Wesley, 2002. ISBN 9780321188786. URL `http://books.google.com/books?id=T3ofAQAAMAAJ`.

38. Hsu, Shih-Hsin, En-Shao Liu, Yia-Chung Chang, James N Hilfiker, Young Dong Kim, Tae Jung Kim, Chun-Jung Lin, and Gong-Ru Lin. “Characterization of Si nanorods by spectroscopic ellipsometry with efficient theoretical modeling”. *physica status solidi (a)*, 205(4):876–879, 2008.

39. Huard, Serge. “Polarization of light”. *Polarization of Light, by Serge Huard, pp. 348. ISBN 0-471-96536-7. Wiley-VCH, January 1997.*, 1, 1997.

40. Huynh, Wendy U, Janke J Dittmer, and A Paul Alivisatos. “Hybrid nanorod-polymer solar cells”. *Science*, 295(5564):2425–2427, 2002.

41. Jackson, John David. *Classical electrodynamics.* Wiley New York, 1962.

42. Jarem, John M and Partha P Banerjee. *Computational methods for electromagnetic and optical systems.* CRC Press, 2011.

43. Jellison, GE. "The calculation of thin film parameters from spectroscopic ellipsometry data". *Thin Solid Films*, 290:40–45, 1996.

44. Jellison, Gerald E. "Data analysis for spectroscopic ellipsometry". *Thin Solid Films*, 234(1):416–422, 1993.

45. Jellison Jr, GE. "Spectroscopic ellipsometry data analysis: measured versus calculated quantities". *Thin solid films*, 313:33–39, 1998.

46. Jellison Jr, Gerald E. "Use of the biased estimator in the interpretation of spectroscopic ellipsometry data". *Applied optics*, 30(23):3354–3360, 1991.

47. Jen, Yi-Jun, Akhlesh Lakhtakia, Ching-Wei Yu, and Chin-Te Lin. "Vapor-deposited thin films with negative refractive index in the visible regime". *arXiv preprint arXiv:0903.1177*, 2009.

48. Johs, Blaine D, John A Woollam, Craig M Herzinger, James N Hilfiker, Ron A Synowicki, and Corey L Bungay. "Overview of variable-angle spectroscopic ellipsometry (VASE): II. Advanced applications". *Society of Photo-Optical Instrumentation Engineers (SPIE) Conference Series*, volume 1, 29–58. 1999.

49. Kabashin, AV, P Evans, S Pastkovsky, W Hendren, GA Wurtz, R Atkinson, R Pollard, VA Podolskiy, and AV Zayats. "Plasmonic nanorod metamaterials for biosensing". *Nature materials*, 8(11):867–871, 2009.

50. Katsarakis, N, G Konstantinidis, A Kostopoulos, RS Penciu, TF Gundogdu, M Kafesaki, EN Economou, Th Koschny, and CM Soukoulis. "Magnetic response of split-ring resonators in the far-infrared frequency regime". *Optics Letters*, 30(11):1348–1350, 2005.

51. Krantz, Steven George and Harold R Parks. *The implicit function theorem: history, theory, and applications.* Springer Science & Business Media, 2002.

52. Krowne, Clifford M, Maurice Daniel, Steven W Kirchoefer, and Jeffrey M Pond. "Anisotropic permittivity and attenuation extraction from propagation constant measurements using an anisotropic full-wave Green's function solver for coplanar ferroelectric thin-film devices". *Microwave Theory and Techniques, IEEE Transactions on*, 50(2):537–548, 2002.

53. Larson, Ron and Bruce Edwards. *Calculus.* Cengage Learning, 2009.

54. Liang, D, D Schmidt, H Wang, E Schubert, and M Schubert. "Generalized ellipsometry effective medium approximation analysis approach for porous slanted columnar thin films infiltrated with polymer". *Applied Physics Letters*, 103(11):111906–111906, 2013.

55. Losurdo, Maria and Kurt Hingerl. *Ellipsometry at the Nanoscale.* Springer, 2013.

56. Mackay, Tom G. *Electromagnetic Anisotropy and Bianisotropy: A Field Guide.* World Scientific, 2009.

57. Mackay, Tom G and Akhlesh Lakhtakia. *Journal of Nanophotonics*, 6(1):069501–069501, 2012.

58. Marques, R, J Martel, F Mesa, and F Medina. "Left-handed-media simulation and transmission of EM waves in subwavelength split-ring-resonator-loaded metallic waveguides". *Physical Review Letters*, 89:183901, 2002.

59. Martin, PJ, RP Netterfield, and WG Sainty. "Modification of the optical and structural properties of dielectric ZrO2 films by ion-assisted deposition". *Journal of Applied Physics*, 55(1):235–241, 1984.

60. McCrackin, Frank L, Elio Passaglia, Robert R Stromberg, and Harold L Steinberg. "Measurement of the thickness and refractive index of very thin films and the optical properties of surfaces by ellipsometry". *J. Res. Nat. Bur. Sect. A*, 67, 1963.

61. Moler, Cleve and Charles Van Loan. "Nineteen dubious ways to compute the exponential of a matrix". *SIAM review*, 20(4):801–836, 1978.

62. Moler, Cleve and Charles Van Loan. "Nineteen dubious ways to compute the exponential of a matrix, twenty-five years later". *SIAM review*, 45(1):3–49, 2003.

63. Muller, Rolf H and Joseph C Farmer. "Fast, self-compensating spectral-scanning ellipsometer". *Review of scientific instruments*, 55(3):371–374, 1984.

64. Nicolson, A.M. and G. F. Ross. "Measurement of the Intrinsic Properties of Materials by Time-Domain Techniques". *IEEE Transactions on Instrumentation and Measurement*, 19(4):377–382, 1970. ISSN 0018-9456.

65. Niklasson, Goran A, CG Granqvist, and O Hunderi. "Effective medium models for the optical properties of inhomogeneous materials". *Applied Optics*, 20(1):26–30, 1981.

66. Olmsted, John Meigs Hubbell. *Advanced calculus.* Prentice Hall, 1961.

67. Papadakis, Georgia T, Pochi Yeh, and Harry A Atwater. "Retrieval of material parameters for uniaxial metamaterials". *arXiv preprint arXiv:1411.6312*, 2014.

68. Pekar, Solomon Isaakovič. *Crystal optics and additional light waves*, volume 57. Benjamin-Cummings Publishing Company, 1983.

69. Rakic, Aleksandar D, Aleksandra B Djurišic, Jovan M Elazar, and Marian L Majewski. "Optical properties of metallic films for vertical-cavity optoelectronic devices". *Applied optics*, 37(22):5271–5283, 1998.

70. Rakić, Aleksandar D., Aleksandra B. Djurišić, Jovan M. Elazar, and Marian L. Majewski. "Optical properties of metallic films for vertical-cavity optoelectronic devices". *Appl. Opt.*, 37(22):5271–5283, Aug 1998. URL `http://ao.osa.org/abstract.cfm?URI=ao-37-22-5271`.

71. Rodenhausen, Keith B, Daniel Schmidt, Tadas Kasputis, Angela K Pannier, Eva Schubert, and Mathias Schubert. "Generalized ellipsometry in-situ quantification of organic adsorbate attachment within slanted columnar thin films". *Optics express*, 20(5):5419–5428, 2012.

72. Röseler, Arnulf. *Infrared Spectroscopy Ellipsometry.* VCH, 1990.

73. Roussel, Ph J, J Vanhellemont, and HE Maes. "Numerical aspects of the implementation of effective-medium approximation models in spectroscopic ellipsometry regression software." *Thin solid films*, 234(1):423–427, 1993.

74. Schmidt, D, B Booso, T Hofmann, E Schubert, A Sarangan, and M Schubert. "Generalized ellipsometry for monoclinic absorbing materials: determination of optical constants of Cr columnar thin films". *Optics letters*, 34(7):992–994, 2009.

75. Schmidt, D, AC Kjerstad, Tino Hofmann, Ralph Skomski, Eva Schubert, and Mathias Schubert. "Optical, structural, and magnetic properties of cobalt nanostructure thin films". *Journal of Applied Physics*, 105(11):113508–113508, 2009.

76. Schmidt, Daniel. "Characterization of highly anisotropic three-dimensionally nanostructured surfaces". *arXiv preprint arXiv:1308.2942*, 2013.

77. Schmidt, Daniel, Benjamin Booso, Tino Hofmann, Eva Schubert, Andrew Sarangan, and Mathias Schubert. "Monoclinic optical constants, birefringence, and dichroism of slanted titanium nanocolumns determined by generalized ellipsometry". *Applied Physics Letters*, 94(1):011914–011914, 2009.

78. Schmidt, Daniel and Mathias Schubert. "Anisotropic Bruggeman effective medium approaches for slanted columnar thin films". *Journal of Applied Physics*, 114(8):083510–083510, 2013.

79. Schubert, M. "Generalized ellipsometry and complex optical systems". *Thin Solid Films*, 313:323–332, 1998.

80. Schubert, Mathias. "Another century of ellipsometry". *Annalen der Physik*, 15(7-8):480–497, 2006.

81. Schubert, Mathias and Wayne Dollase. "Generalized ellipsometry for biaxial absorbing materials: determination of crystal orientation and optical constants of Sb_2S_3". *Optics letters*, 27(23):2073–2075, 2002.

82. Schubert, Mathias, Bernd Rheinländer, John A Woollam, Blaine Johs, and Craig M Herzinger. "Extension of rotating-analyzer ellipsometry to generalized ellipsometry: determination of the dielectric function tensor from uniaxial TiO¡ sub¿ 2¡/sub¿". *JOSA A*, 13(4):875–883, 1996.

83. Schultz, J.W. *Focused Beam Methods: Measuring Microwave Materials in Free Space.* Createspace Independent Pub, 2012. ISBN 9781480092853.

84. Shadrivov, Ilya V, Steven K Morrison, and Yuri S Kivshar. "Tunable split-ring resonators for nonlinear negative-index metamaterials". *Optics Express*, 14(20):9344–9349, 2006.

85. Shah, Piyush J., Xiaoxu Niub, and Andrew M. Sarangan. "High aspect ratio silver nanorod thin films grown at cryogenic substrate temperature". *J. of Nanosci. Lett.*, 3(19), 2013.

86. Simovski, Constantin R. "On electromagnetic characterization and homogenization of nanostructured metamaterials". *Journal of Optics*, 13(1):013001, 2011.

87. Smith, David R, Willie J Padilla, DC Vier, Sc C Nemat-Nasser, and Seldon Schultz. "Composite medium with simultaneously negative permeability and permittivity". *Physical review letters*, 84(18):4184, 2000.

88. Smith, DR, S Schultz, P Markoš, and CM Soukoulis. "Determination of effective permittivity and permeability of metamaterials from reflection and transmission coefficients". *Physical Review B*, 65(19):195104, 2002.

89. Strang, Gilbert. *Linear Algebra and Its Applications.* Engage Learning; 4th edition, 2006.

90. Stroud, D and FP Pan. "Self-consistent approach to electromagnetic wave propagation in composite media: Application to model granular metals". *Physical review B*, 17(4):1602, 1978.

91. Takeda, Mitsuo, Hideki Ina, and Seiji Kobayashi. "Fourier-transform method of fringe-pattern analysis for computer-based topography and interferometry". *JosA*, 72(1):156–160, 1982.

92. Tokpanov, Yu, V Lebedev, and W Pellico. *Measurements of Magnetic Permeability of Soft Steel at High Frequencies.* Technical report, Fermi National Accelerator Laboratory (FNAL), Batavia, IL, 2012.

93. Tompkins, Harland and Eugene A Irene. *Handbook of ellipsometry.* Access Online via Elsevier, 2005.

94. Tompkins, Harland G and William A McGahan. *Spectroscopic ellipsometry and reflectometry: a user's guide*. Wiley, 1999.

95. Valentine, Jason, Shuang Zhang, Thomas Zentgraf, Erick Ulin-Avila, Dentcho A Genov, Guy Bartal, and Xiang Zhang. "Three-dimensional optical metamaterial with a negative refractive index". *nature*, 455(7211):376–379, 2008.

96. Vedam, K. "Spectroscopic ellipsometry: a historical overview". *Thin solid films*, 313:1–9, 1998.

97. Viète, François, Frans van Schooten, and Joseph Ehrenfried Hofmann. *Opera mathematica*. Georg Olms Verlag, 1970.

98. Warnick, Karl F. *Numerical Methods for Engineering: An Introduction Using MATLAB and Computational Electromagnetics Examples*. SciTech Pub., 2011.

99. Weir, William B. "Automatic measurement of complex dielectric constant and permeability at microwave frequencies". *Proceedings of the IEEE*, 62(1):33–36, 1974. ISSN 0018-9219.

100. Weisstein, Eric W. ""Complex Argument" From MathWorld - A Wolfram Web Resource". URL `http://mathworld.wolfram.com/ComplexArgument`.

101. Woollam, John A. "Ellipsometry, variable angle spectroscopic". *Wiley Encyclopedia of Electrical and Electronics Engineering*, 2000.

102. Woollam, John A, Blaine D Johs, Craig M Herzinger, James N Hilfiker, Ron A Synowicki, and Corey L Bungay. "Overview of variable-angle spectroscopic ellipsometry (VASE): I. Basic theory and typical applications". *Society of Photo-Optical Instrumentation Engineers (SPIE) Conference Series*, volume 1, 3–28. 1999.

103. Woollam, John A and Paul G Snyder. "Fundamentals and applications of variable angle spectroscopic ellipsometry". *Materials Science and Engineering: B*, 5(2):279–283, 1990.

104. Woollam, John A, Paul G Snyder, and Martin C Rost. "Variable angle spectroscopic ellipsometry: A non-destructive characterization technique for ultra thin and multilayer materials". *Thin Solid Films*, 166:317–323, 1988.

105. Zhang, BP, NT Binh, Y Segawa, K Wakatsuki, and N Usami. "Optical properties of ZnO rods formed by metalorganic chemical vapor deposition". *Applied Physics Letters*, 83(8):1635–1637, 2003.

REPORT DOCUMENTATION PAGE

Form Approved
OMB No. 0704–0188

1. REPORT DATE *(DD–MM–YYYY)* 06–01–2015	**2. REPORT TYPE** PhD Dissertation	**3. DATES COVERED** *(From — To)* Apr 2014 — Jun 2015

4. TITLE AND SUBTITLE

Identifying the experimental and theoretical effective characteristics of nonaligned anisotropic metamaterials

5a. CONTRACT NUMBER

5b. GRANT NUMBER

5c. PROGRAM ELEMENT NUMBER

6. AUTHOR(S)

Benson, Michael R, Civ

5d. PROJECT NUMBER

5e. TASK NUMBER

5f. WORK UNIT NUMBER

7. PERFORMING ORGANIZATION NAME(S) AND ADDRESS(ES)

Air Force Institute of Technology
Graduate School of Engineering and Management (AFIT/EN)
2950 Hobson Way
WPAFB OH 45433-7765

8. PERFORMING ORGANIZATION REPORT NUMBER

AFIT-ENP-DS-15-J-008

9. SPONSORING / MONITORING AGENCY NAME(S) AND ADDRESS(ES)

Department of Engineering Physics
2950 Hobson Way
WPAFB OH 45433-7765
DSN 271-0690, COMM 937-255-3636
Email: michael.benson@afit.edu

10. SPONSOR/MONITOR'S ACRONYM(S)

AFRL

11. SPONSOR/MONITOR'S REPORT NUMBER(S)

12. DISTRIBUTION / AVAILABILITY STATEMENT

DISTRIBUTION STATEMENT A:
APPROVED FOR PUBLIC RELEASE; DISTRIBUTION UNLIMITED.

13. SUPPLEMENTARY NOTES

This material is declared a work of the U. S. Government and is not subject to copyright protection in the United States.

14. ABSTRACT

Previous research into anisotropic materials has assumed certain properties in order to make the underlying mathematics tractable. One of the assumptions is the alignment of the optical axes with the laboratory frame of reference, such as split-ring resonators lying flat on the material plane. This assumption does not hold true for many metamaterials, such as tilted nanorods. Techniques such as ellipsometry are needed to analyze the effective characteristics of these highly anisotropic structures. In this research, tilted nanorods are analyzed using generalized ellipsometry to extract the indices of the optical axes. The underlying physics of ellipsometry is then used to create a new effective characterization technique called Permittivity and Permeability Tensor Extraction (PPTE), which makes fewer assumptions about the underlying structure of the material and allows for the analysis of a much larger class of structures. PPTE is used to find the effective characteristics of several structures, such as a structure with anisotropy-inducing inclusions and the tilted nanorods. Finally, PPTE is used to begin to examine some of the underlying presumptions about how metamaterials operate, demonstrating that some of the classically used models for calculating permittivity tensors are approximations. The utility of these models in determining the permittivity tensor is studied for several different materials with different properties.

15. SUBJECT TERMS

Ellipsometry, Effective Material Parameters, Metamaterials, Nanorods, Parameter Extraction, Permittivity Tensor, Permeability Tensor

16. SECURITY CLASSIFICATION OF:			**17. LIMITATION OF ABSTRACT**	**18. NUMBER OF PAGES**	**19a. NAME OF RESPONSIBLE PERSON**
a. REPORT	**b. ABSTRACT**	**c. THIS PAGE**			Dr. Marciniak, AFIT/ENP
U	U	U	U	217	**19b. TELEPHONE NUMBER** *(include area code)* (937) 255-3636, x4529